



Title	Characterization of Ni-Based Coated Layer on Carbon Steel by Electron Microscopy and Neutron Radiography
Author(s)	Eni, Sugiarti
Citation	北海道大学. 博士(工学) 乙第6956号
Issue Date	2015-03-25
DOI	10.14943/doctoral.r6956
Doc URL	<a href="http://hdl.handle.net/2115/60907">http://hdl.handle.net/2115/60907</a>
Type	theses (doctoral)
File Information	Eni_Sugiarti.pdf



[Instructions for use](#)

# **Characterization of Ni-Based Coated Layer on Carbon Steel by Electron Microscopy and Neutron Radiography**

**By**

**Eni Sugiarti**



**THESIS FOR THE DEGREE OF DOCTOR OF PHILOSOPHY**

**Laboratory of Advanced Materials (LOAM)  
Materials Science Division, Graduate School of Engineering  
Hokkaido University  
February, 2015**

# **Characterization of Ni-Based Coated Layer on Carbon Steel by Electron Microscopy and Neutron Radiography**

**By**

**Eni Sugiarti**

**A thesis submitted in partial fulfillment of the requirements for the degree of Doctor of Philosophy**

**Examination Committee: Prof. Somei Ohnuki  
Prof. Naoyuki Hashimoto  
Prof. Shigenari Hayashi  
Prof. Ukai  
Prof. Miura**

**Doctor`s Thesis  
Division of Materials Science  
Graduate School of Engineering, Hokkaido University  
February, 2015**

**Characterization of Ni-Based Coated Layer on Carbon Steel by Electron  
Microscopy and Neutron Radiography**

Receipt of Doctor Thesis

	Date	Seal
Prof. Somei OHNUKI		
Prof. Naoyuki HASHIMOTO		
Prof. Shigenari HAYASHI		
Prof. UKAI		
Prof. MIURA		

Eni Sugiarti  
Laboratory of Advanced Materials (LOAM)  
Division of Materials Science and Engineering  
Graduate school of Engineering  
Hokkaido University  
February, 2015

## Acknowledgements

I would like to sincerely express my appreciation to my supervisor - Professor Somei Ohnuki for giving me the change to continue my PhD study. I am very grateful for his patient guidance and warm encouragement all the time not only when I am in Japan but also in Indonesia. Thanks for spending your time for discussion and all the effort on giving helpful comment on my paper and thesis.

I would like to thank my co-supervisor, Professor Naoyuki Hashimoto for supporting and inspiring me during the research work and spending time on my papers and thesis work.

I am grateful to Professor Shigenari Hayashi for helpful advices, sharing your knowledge in the oxidation field, spending your time on meetings, giving suggestions for the experiment, discussing and resolving the problem when writing my paper.

Special thanks to Dr. Yongming Wang for his continuous help during my study. I have particularly enjoyed our numerous exciting discussions, which directly fruit several important aspects of this work. I am benefited from all your help and would like to express my deep appreciation to you.

Thanks also go to Dr. Shigehito Isobe for being open minded to me and patiently answering my questions. I appreciated to the help I got from Ms. Kaori Kobayashi. Because of you, I am really enjoyed in Japan.

I am indebted to Dr. Kemas A. Zaini, Indonesian Institute of Sciences (LIPI), for admitting me into his research group and to the coating project. His encouragement and inspiration are truly appreciated.

I wish to express my thanks to all of my team work in Indonesia, Fredina, Desti, Anton, Bambang, Tia, Leni, Risma for supporting this work. I am grateful to Yuliati H, Julio and Isnaeni for her comments and support.

I wish to thank all of staffs in `Nanotechnology Platform`, in particular Mr. Endo for training me on FIB, Mr. Miyazaki for training me FE-EPMA and X-ray facilities. This work benefits a lot from your valuable support on microstructure study. Thanks also to Mr. Kenji Ookubo for providing his assistance and expertise during the use of the high voltage electron microscopy.

I acknowledge financial support from JSPS PhD Ronpaku Program, Japan for providing me the opportunity to continue my Doctor Course at Hokkaido University and LIPI Competitive Program, Indonesia enabling me to do related researches in Indonesia.

I would like to thank all the former and present students in the Laboratory of Advanced Materials (LOAM). I am very happy for the enjoyable working environment you all have created. A lot of thanks to you all surrounding me and the moments you shared with me. You never know how much I appreciate to work with you here, in Japan.

Finally but not the least, to my husband, Afri, my children, Alya, Radhitya and Daffa, thanks for all your love and for believing much more in me than I do myself. Special thanks also to my parents and my mother in law for caring and praying all the time for me. Without all of your supports, I could not manage to finish my work and I could not be a stronger mother and researcher.

## Abstract

Development of electrical power generation system is assessed by special attention to plant efficiency. Coal-fired power generation systems are major contributor to carbon dioxide (CO<sub>2</sub>) emission. In 2012, 48 % of Indonesian energy consumption was based on coal. Higher operating temperatures and pressures for steam and gas turbines in coal-fired power generation have been developed for many years and result in higher system efficiencies. However, the rate of change needs to be increased to reduce CO<sub>2</sub> emission. According to greenhouse gas (GHG) commitment, Indonesia government plans to increase the use of geothermal energy, which is a viable solution to rapidly expanding global crisis. However, steam-side oxidation usually occurs in the super-heater and re-heater section of coal-fired power systems, where the materials are exposed to the highest operating steam temperatures. On the other hand, the geothermal fluid, water and steam, and their mixtures contain many kinds of the corrosive chemicals, which cause scaling and corrosion in wells and surface installations. The oxidation of steam turbine and corrosion of geothermal pipeline are the most important subjects to be evaluated.

Steel products are widely used in material for coal-fired and geothermal power plant industries due to economical reason and operating temperature limit. However, poor corrosion and oxidation performances restrict the effectiveness of steel products. To improve the surface properties, a number of surface modifications are performed with different techniques where coatings are deposited on the steel surface. Recently, Ni-based coatings have come into wide used because of their good wear resistance and durability at high temperatures. Additions of the cobalt (Co), chromium (Cr), and aluminum (Al) to the coating material promote the hardness, formation of intermetallic phases, and increase the oxidation/corrosion properties.

Details of experimental methods have been showed in chapter 3. In the present study, NiCoCrAl is diffusion-coated onto low carbon steel by electrodeposition to create a NiCo coating layer followed by pack cementation of Cr and Al. As-coated and treated samples have been investigated by using HVEM, TEM, XRD, SEM, EPMA, and EDS. The cross sectional TEM specimens have been prepared by the combination of ion slicer (IS) and focused ion beam (FIB). Nano to macro scale characterizations presented in this study are powerful techniques to understand the material properties related to the structure of crystallized material.

In chapter 4, the effect of the Co concentration and temperature on hardness and oxidation properties as well as phase constituent in the coated layer was investigated. An

analysis of the correlations between the structure, hardness properties, oxidation behaviors, and phase formation was also discussed. The results showed that 5% Co coated sample has good hardness properties, oxidation resistance and forms a series of high melting phases such as  $\gamma$ -(Ni, Fe),  $\text{Al}_3\text{Ni}$ ,  $\zeta$ -(Al,Cr)Ni and oxidation resistant of  $\beta$ -(Ni,Al).

In chapter 5, the oxidation behavior of the coated samples developed by different temperature of pack cementation in isothermal oxidation at 800 °C for 100 h was studied. The sample developed at 800 °C showed better oxidation resistance than that at 900 °C and 1000 °C, because the oxide mainly consists of  $\alpha$ - $\text{Al}_2\text{O}_3$  with continuous, thin and less porous structures. Thus, it possesses the capability as a diffusion barrier for oxygen to protect the carbon steel substrate when subject to severe oxidation.

In chapter 6, the formation of meta-stable  $\text{Al}_2\text{O}_3$  on NiCoCrAl coated layers during initial stage for up to 100 h exposure time under isothermal oxidation at 800 °C in air was comprehensively presented. The oxide scale formed on the initial stage of 1 h and 15 h of exposure consists of several polymorphs crystalline of alumina structure such as meta-stable  $\delta$ ,  $\theta$ , and stable  $\alpha$ - $\text{Al}_2\text{O}_3$  phases. However, the oxide scale of 100 h sample was identified to be mostly composed of  $\alpha$ - $\text{Al}_2\text{O}_3$  and a small amount of  $\delta$ - $\text{Al}_2\text{O}_3$ . The results were plotted on the isothermal oxidation map at lower temperature of 800 °C. It is worth noted that the result in present study is the first result which will be contributed to the oxide ternary map of Ni–Cr–Al at 800 °C.

In chapter 7, the implementation of the coating process on pipeline system and an experimental simulation was carried out by developing closed loop piping system constructed by low carbon steel, ST37, and 304 SS materials. Three shapes of pipes were selected, i.e, straight, elbow and tee. The performance of uncoated and coated carbon steel ST37 was compared with 304 SS pipes after acid vapor corrosion test using 37% HCl for 48 hours. Neutron radiography and tomography (NRT) as a new method for non-destructive testing in this field has been adopted for pipe inspection and corrosion monitoring. 2D neutron radiography (NR) and 3D neutron tomography (NT) showed the existence of corrosion product in the form of rust and blister inside the pipe wall.

Finally the general conclusion has been discussed in chapter 8. The conclusions on the performance of Ni-based coated carbon steel after oxidation and corrosion are used to make some recommendations for future research and development in power plant industries.

# Contents

<b>Chapter 1</b>	<b>Introduction.....</b>	<b>1</b>
1.1	Historical background .....	1
1.2	Objectives .....	6
1.3	The structure of the thesis .....	7
<b>Chapter 2</b>	<b>Material Issues for Power Plant System .....</b>	<b>8</b>
2.1	Material used in power plant.....	8
2.2	Operational challenges in steam engine and piping component.....	9
2.3	Protective coating .....	12
2.3.1	The concept of overlay coating .....	14
2.3.2	Metallurgy and application of MCrAlY coatings .....	14
2.3.3	Role of alloying element .....	15
2.3.4	Multi layer method of NiCoCrAl Coatings .....	16
2.4	General aspects of high temperature oxidation .....	21
2.4.1	Oxidation process .....	22
2.4.2	Oxidation kinetics.....	22
2.4.3	Oxidation of alloys .....	26
2.5	Research and development of NiCoCrAl Coating .....	28
<b>Chapter 3</b>	<b>Methodology .....</b>	<b>33</b>
3.1	Experimental procedure.....	33
3.1.1	Material .....	33
3.1.2	Coating process .....	34
3.1.3	Mechanical test (Hardness) .....	37
3.1.4	Thermal test.....	37
3.1.4.1	Isothermal oxidation .....	37
3.1.4.2	Acid vapor corrosion .....	38
3.1.5	Sample preparation for cross-sectional microstructure .....	40
3.1.5.1	SEM and FE-EPMA samples .....	40
3.1.5.2	HVEM and TEM samples .....	41
3.1	Experimental techniques and instrumentation.....	44
3.2.1	Multi Beam High Voltage Electron Microscopy (HVEM).....	44
3.2.2	Transmission Electron Microscopy (TEM).....	45
3.2.2.1	Energy Dispersive X-ry Spectroscopy (EDS) .....	46

3.2.2.2 Selected Area Electron Diffraction (SAED).....	46
3.2.3 Ion beam milling techniques .....	46
3.2.3.1 Argon Ion Slicer (IS) .....	47
3.2.3.2 Focused Ion Beam (FIB) .....	48
3.2.4 X-Ray Diffraction (XRD).....	49
3.2.5 Scanning Electron Microscopy (SEM).....	50
3.2.6 Field Emission - Electron Probe Micro Analyzer (FE-EPMA) .....	50
3.2.7 Non destructive techniques for material characterization .....	51
3.2.7.1 Neutron Radiography (NR) Facility at BATAN, Indonesia.....	57
3.2.7.2 Computed Tomography (CT) .....	59
<b>Chapter 4 Characterization of Ni-Based Coated Layer .....</b>	<b>61</b>
4.1 Effect of Co content on the hardness and structural properties.....	61
4.2 Effect of Co content on the microstructure .....	63
4.3 High temperature oxidation results.....	66
4.4 Nanostructure of the as-coated sample .....	68
4.5 Phase constitution of the NiCoCrAl coating layer.....	71
4.6 Conclusions.....	74
<b>Chapter 5 Oxidation Behavior of Ni-Based Coated Layer.....</b>	<b>76</b>
5.1 Oxidation kinetics .....	76
5.2 Surface morphologies and phases.....	78
5.3 Cross-sectional microstructure and elemental diffusion .....	79
5.4 Oxide formation.....	81
5.5 Conclusion .....	83
<b>Chapter 6 Formation of Meta-Stable Al<sub>2</sub>O<sub>3</sub> Scale during Oxidation .....</b>	<b>84</b>
6.1 Phase constitution in as-coated and oxidized samples.....	84
6.2 Cross-sectional structures in micro scale .....	86
6.3 Cross-sectional structures in nano scale .....	88
6.4 Properties of polymorph alumina.....	90
6.4.1 Corundum $\alpha$ -Al <sub>2</sub> O <sub>3</sub> .....	90
6.4.2 Tetragonal $\delta$ -Al <sub>2</sub> O <sub>3</sub> .....	91
6.4.3 Monoclinic $\theta$ -Al <sub>2</sub> O <sub>3</sub> .....	91
6.5 Polymorphic crystal structures of alumina.....	92
6.6 Composition of oxide grown on Ni-Cr-Al system at 800 °C.....	98
6.7 Conclusion .....	101

<b>Chapter 7</b>	<b>Non – Destructive Characterization of Corroded Carbon Steel .....</b>	<b>103</b>
7.1	Scattering interactions .....	104
7.2	Outer corrosion.....	105
7.3	Internal corrosion (rust and blister in 2D and 3D NRT images) .....	107
7.4	Conclusion .....	110
<b>Chapter 8</b>	<b>General Discussion and Conclusion .....</b>	<b>112</b>
8.1	Modelling structure and phase characterization .....	112
8.2	Performance of Ni-based coated carbon steel on oxidation and corrosion .....	113
8.3	The influence of the coating system on the oxidation and corrosion .....	115
8.2	Recommendations for future research and development.....	117
<b>References</b>	.....	<b>118</b>
<b>Appendices</b>	.....	<b>127</b>

## List of Caption Figures

- 1.1 Indonesia electricity generation capacity by source, 2012.
- 1.2 World's top coal exporters, 2012.
- 1.3 CO<sub>2</sub> emissions of several power sources per electric generating capacity (including Methane).
- 1.4 Gas and steam condition for power plant generation system.
- 1.5 Top five generator of geothermal electricity, 2011.
- 1.6 Indonesia geothermal potential resources and prospect status map. (a-g) the location of existing geothermal power plant.
- 1.7 Existing geothermal power plant in Indonesia located in Sumatera, Sulawesi and Java Island.
- 2.1 Uses of A-USC boiler materials.
- 2.2 Distribution of piping used in geothermal system.
- 2.3 Maximum service temperature for pipe material.
- 2.4 Relative oxidation and corrosion resistance of high-temperature coating systems.
- 2.5 Schematic representation of NiCoCrAl multi - layer coatings on carbon steel substrate.
- 2.6 The main chemical reactions involved in the pack cementation process.
- 2.7 Ellingham diagram of free energy of formation of oxides as a function of temperature.
- 2.8 Different types of behavior for high temperature oxidation and corresponding mass gain curves. (a) Parabolic oxidation, (b) Sub-parabolic oxidation, (c) Breakaway oxidation, (d) Oxide scale spallation, and (e) Evaporation of volatile species.
- 2.9 Binary alloy oxidation, component A is more noble and B is more active.
- 2.10 Binary alloy oxidation, component A and B form stable oxides but BO is more stable than AO.
- 2.11 Research road map on the development of Ni-based coated layer on carbon steel substrate in geothermal power plant application.
- 2.12 Recent advancement of nano - micro - macro scale applied in materials characterization. Case study: NiCoCrAl coated sample on carbon steel substrate.
- 2.13 A variety of techniques can be used to probe complex structure.
- 3.1 Flow diagram of the coating process and the characterization method.
- 3.2 (a) Schematic illustration, (b) Ni-*strike* solution, and (c) experimental set-up of NiCo *watt* electroplating.

- 3.3 (a) Schematic illustration, (b) sample and pack mixture in the crucible, and (c) experimental set-up for Cr and/or Al pack cementation.
- 3.4 Principle of hardness test. (a) position of indenter and (b) measuring the diameter of indentation.
- 3.5 Schematic illustration of oxidation pattern.
- 3.6 Schematic drawing the placement of Ni plate as anode was placed inside the piping components for electroplating process.
- 3.7 (a) Schematic illustration, photograph image (b) before, and (c) after acid vapor corrosion test by 37% HCl for 48 h.
- 3.8 Schematic illustration of the IS specimen size.
- 3.9 Typical thin (less than 1  $\mu\text{m}$ ) “lagoon shaped” area produced by IS technique. The coated layer is indicated by the yellow arrow and an observable area is indicated by the yellow circle.
- 3.10 Different steps of an ex-situ lift out process. (Top) plain view and (bottom) cross cut view.
- 3.11 Schematic illustration of argon ion beam irradiation to a specimen. (Left) Argon ion source and the specimen holder rock  $\pm 6.0^\circ$ . (Right) A side view of the specimen blocks.
- 3.12 Schematic diagrams of (a) a basic FIB system and (b) liquid metal ion source.
- 3.13 Schematic illustration for capturing an image by neutron radiography.
- 3.14 NR arrangements for the collimation ratio, the neutron flux and the transmitted intensity of the radiation measurements.
- 3.15 Detection techniques for neutrons.
- 3.16 The logarithmic scale of attenuation coefficient of elements for neutrons (separate dots), for 1 MeV gamma-ray (dotted line), for 150 keV X-ray (solid line) and for 60 keV X-ray (dashed line).
- 3.17 The NR facility at BATAN–Serpong. (a) The photograph of neutron radiography facility, (b) A Schematic drawing of neutron radiography facility.
- 3.18 Schematic illustration showing equipment part for capturing the 2D and 3D NRT.
- 4.1 Micro-hardness measurements of uncoated and coated samples.
- 4.2 Surface morphologies of NiCoCrAl coating on carbon steel substrate with different Co contents: (a) 1 wt% and (b) 5 wt%.
- 4.3 Cross-sectional microstructure and composition gradients of Ni(1%)Co plating, followed by Cr-Al pack diffusion coating at 800 °C.

- 4.4 Cross-sectional microstructure and composition gradients of Ni(5%)Co plating, followed by Cr-Al pack diffusion coating at 800 °C.
- 4.5 Cross-sectional microstructure and composition gradients of Ni(5%)Co plating, followed by Cr-Al pack diffusion coating at 1000 °C.
- 4.6 Mass gain per unit area versus time during oxidation of coatings at 800 °C for 100 hours.
- 4.7 Cross-sectional micrographs (left) and elemental distribution (right) of the oxidized samples developed at various condition: Sample #1: Ni(1%)CoCrAl, coated at 800 °C; Sample #2: Ni(5%)CoCrAl, coated at 800 °C and Sample #3: Ni(5%)CoCrAl, coated at 1000 °C.
- 4.8 Nanostructure of sample #1: (a) bright field XTEM images, (b) SAED patterns and (c) HRTEM images obtained from the circled area.
- 4.9 Nanostructure of sample #2: (a) bright field XTEM images, (b) SAED patterns and (c) HRTEM images obtained from the circled area.
- 4.10 Nanostructure of sample #3: (a) bright field XTEM images, (b) SAED patterns and (c) HRTEM images obtained from the circled area.
- 5.1 The oxidation mass gain at 800 °C in air for three types of the coated samples, and (b) rate constant,  $k_p$ .
- 5.2 (left) SEM images showing the surface morphologies and (right) corresponding XRD patterns of three types of the coated sample after oxidation at 800 °C for 100 h : (a-b) 800 °C, (c-d) 900 °C, and (e-f) 1000 °C.
- 5.3 Cross-sectional micrographs (left) and corresponding elemental distribution (right) of three types of the samples developed at various temperatures: (a) 800 °C, (b) 900 °C, and (c) 1000 °C.
- 5.4 Cross-sectional micrographs (left) and corresponding elemental distribution (right) after oxidation at 800 °C for 100 h in air for the samples developed at various temperatures: (a) 800 °C, (b) 900 °C, and (c) 1000 °C.
- 6.1 XRD patterns of as coated and after isothermal oxidation at 800 °C in air for various times.
- 6.2 SEM images showing cross-sectional microstructure of the samples: (A) as-coated, (B) 1 h, (C) 15 h, (D) 46 h, and (E) 100 h oxidized. Small letter (a-f) indicates enlarge SEM images obtained from the rectangular marked areas.
- 6.3 Bright field XTEM images of oxidized sample with different exposure time: (a) 1 h and

- (b) 100 h. A high magnification image obtained from the rectangular area (top image). P1) and (P2) → fine grain of  $\alpha$ -Al<sub>2</sub>O<sub>3</sub>, (P3) → area where  $\delta$ -Al<sub>2</sub>O<sub>3</sub> is present and (P4) → large grain containing dislocations of spinel NiAl<sub>2</sub>O<sub>4</sub>.
- 6.4 Hexagonal unit cell of  $\alpha$ -Al<sub>2</sub>O<sub>3</sub> with (a) side view and (b) (0001) projection.
  - 6.5 The  $\theta$ -Al<sub>2</sub>O<sub>3</sub> monoclinic unit cell. Large sphere represent O atom and small Al. Example of tetra- and octahedral Al position are indicated.
  - 6.6 Schematic illustration for indexing the electron diffraction pattern.
  - 6.7 SAED patterns showing several polymorphic crystal structures of alumina: (a).  $\delta$ -Al<sub>2</sub>O<sub>3</sub>, (b).  $\theta$ -Al<sub>2</sub>O<sub>3</sub>, (c).  $\alpha$ -Al<sub>2</sub>O<sub>3</sub>, (d). spinel NiAl<sub>2</sub>O<sub>4</sub>, and (e). cubic (Al,Cr)<sub>2</sub>O<sub>3</sub>. Symbol B in the SAED pattern represents the incident electron beam direction of the diffraction pattern.
  - 6.8 Measured lattice parameter of spinel NiAl<sub>2</sub>O<sub>4</sub> (red line) and cubic (Al,Cr)<sub>2</sub>O<sub>3</sub> (blue line) phases obtained from the coated sample oxidized at 800 °C for up to 100 h.
  - 6.9 Approximation of oxide morphology map for ternary Ni-Cr-Al based on the established phases in the NiCo-Cr-Al coatings after oxidation at 800 °C for 100 h. Boundaries of alumina formers are plotted as characterized by Nicholls et al.
  - 6.10 Oxide composition grown on Ni–Cr–Al coatings after oxidation at 900 °C for 500 h presented by M. Seraffon et al. [88]. Boundaries of alumina formers are compared to those obtained at 900 °C and 950 °C [86] and by Nicholls et al. [85].
  - 7.1 Different mechanism of scattering interaction of X-ray and neutron beams.
  - 7.2 Different contrast of observing element under X-ray and neutron beams according to their thermal conductivity.
  - 7.3 Photographs showing the piping components after acid vapor corrosion test using 37% HCl for 48 h. Left top image showing the piping construction. (1-5) designating the location of the pipe components. (A-D) index designating the pipe materials described in Table 3.
  - 7.4 Photograph of pipe components at position 1 and corresponding neutron 2D radiography image. Magnified images obtained from the mid plane of all pipes area.
  - 7.5 Photograph of pipe components at position 2 and corresponding neutron 2D radiography image. Magnified images obtained from the mid plane of all pipes area.
  - 7.6 Neutron 3D tomography images of pipe components at position 2.

- 8.1. Schematic illustration showing the cross-sectional structure of the NiCoCrAl coated layer on carbon steel substrate with different coating temperature.
- 8.2. The oxidation mass gain at 800 °C for 100 h of carbon steel without and with NiCoCrAl coatings. Inset figure shows the magnified oxidation mass gain of NiCoCrAl coatings.
- 8.3. The corrosion mass change under immersion using 37% HCl for 24 hours of several coating systems.

## List of Caption Tables

- 2.1. Forms and causes for metal in geothermal system and ways to prevent attack.
- 2.2. Percentage of material failures.
- 2.3. Desirable features of an oxidation / corrosion resistance coating.
- 3.1 Chemical composition of low carbon steel substrate (wt%).
- 3.2 Formulation of Ni electroplating.
- 3.3 Formulation of the pack mixture.
- 3.4 Chemical composition of ST37 and 304 SS.
- 3.5 Equipment used for metallographic sample preparation.
- 3.6 Instrumental parameters of neutron radiography facility at BATAN, Indonesia.
- 4.1 Chemical composition, phase identification, and lattice parameters in the coated layers identified by SAED patterns.
- 5.1 Measured parabolic rate constant at two stage of oxide growth for three types of the coated samples.
- 6.1 Structure and properties of alumina polymorphs.
- 6.2 Lattice parameter determined from the coated layers.
- 6.3 Compositions obtained in the coated layer corresponding to oxide species.

# Chapter 1

## Introduction

### 1.1 Historical background

Increasing the efficiency of energy production is one method to reduce the carbon dioxide emissions generated, and thus contain the global climate change. Increase level of CO<sub>2</sub> in atmosphere derives mostly from combustion of fossil fuels. Since fossil fuels will most probably remain as an important source of energy in the coming decades, increasing the efficiency of energy production will have direct and crucial impact to the greenhouse gas (GHG) emission generated. In line with the world's commitment on climate change, Indonesia government announced non-binding emission reduction target of 26% lower intensity than the baseline of 2020 using domestic budget. With international support, the reduction could be further increased to 41% [Ministry of Energy and Mineral Resources - Indonesia, 2010]. To meet this target, Indonesia government is preparing National Action Plan on GHG Reduction (2010-2020). There are also several policy measures relevant to climate change, primarily in energy sector.

The primary energy supply in Indonesia is mainly based on fossil fuels like oil, gas and carbon. Unlike many other countries, Indonesia government encourages increased use of coal in the power sector, because of the relatively abundant domestic supply. In 2012, 48 % of Indonesian energy consumption was based on coal, 22 % on natural gas and, 12 % on oil. Renewable energy, particularly hydro and geothermal have a share of 11 % and 2%, respectively as shown in Fig.1.1.

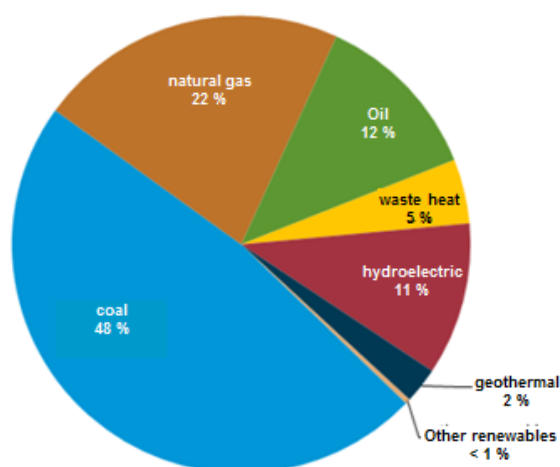


Figure. 1.1. Indonesia electricity generation capacity by source, 2012 [1].

Indonesia plays an important role in world coal markets, particularly as a regional supplier to Asian markets. Fig.1.2 shows that Indonesia has been the largest exporter of thermal coal, typically used in power plants, for several years. In 2012, Indonesia exported about 383 million short tons of coal, making it the world's largest exporter of coal by weight.

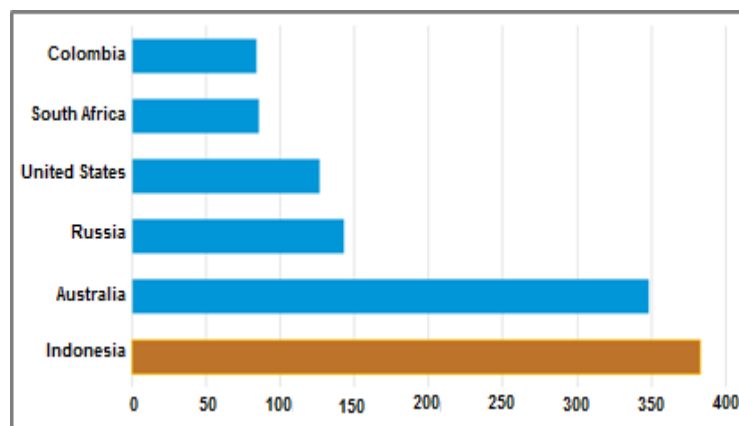


Figure 1.2. World's top coal exporters, 2012 [1].

Unfortunately, coal-fired power generation is also accompanied by considerable greenhouse gas (GHG) emissions. Coal emits more CO<sub>2</sub> (carbon dioxide) than any other form of power generation as illustrated in Fig.1.3. When considering that coal will remain to be the largest source of global power generation, reducing the amount of CO<sub>2</sub> emitted by coal-fired power plants will be very effective in reducing global warming.

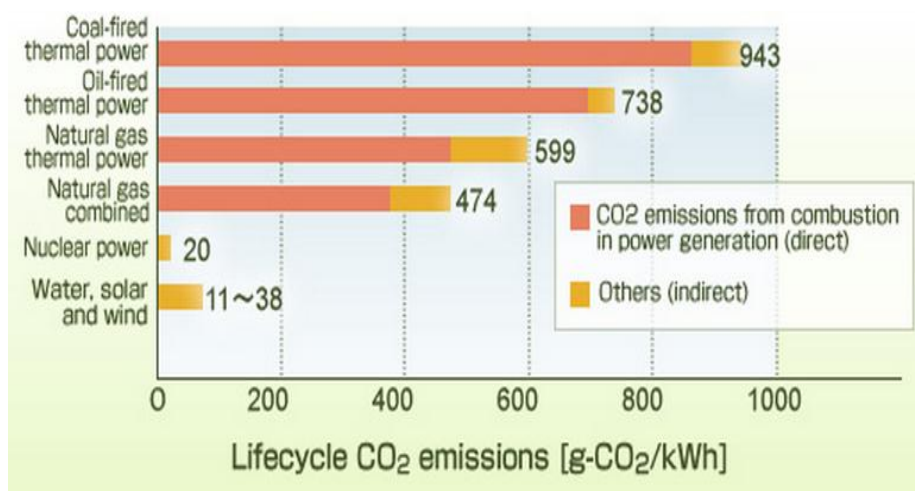


Figure 1.3. CO<sub>2</sub> emissions of several power sources per electric generating capacity (including Methane) [2].

High expectations are being placed on the development of technologies that improve the efficiency of coal-fired power generation in environmentally conscious ways. Fig. 1.4 shows that higher operating temperatures and pressures for steam and gas turbines have been under development for many years and result in higher system efficiencies. However, the rate of change needs to be increased to meet the CO<sub>2</sub> emission reduction targets being set.

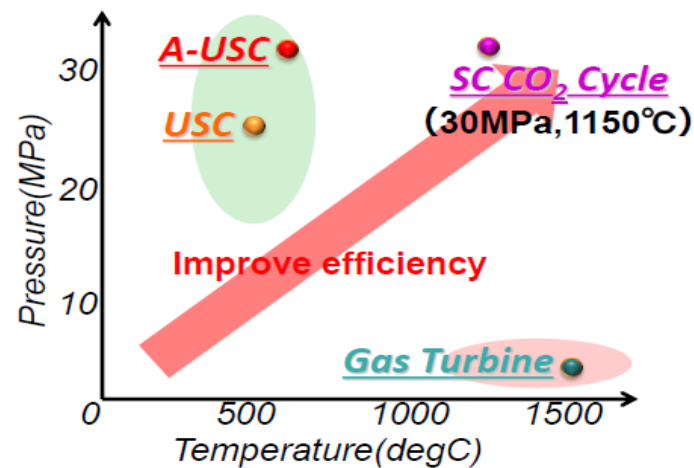


Figure 1.4. Gas and steam condition for power plant generation system [2].

According to GHG commitment, Indonesia government also plan to increase the use of renewable energy to 15% of the electricity portfolio by 2025 depend on developing the country's geothermal resources. There are reasons why geothermal energy is a viable solution to a rapidly expanding global crisis.

- ✓ It is renewable energy: geothermal energy is considered to be limitless. Its heat comes from the core of the Earth, a 24-hour-a-day, 365-day-a-year energy source.
- ✓ It is convenient: geothermal heat can literally be found everywhere. There is a constant supply. Geothermal energy is not dependent upon factors like sun or wind to generate power. It is also local, geothermal energy never has to be imported.
- ✓ A cleaner power plant: generate electricity without spewing tons of toxins into the atmosphere.

Country reviews presented at the World Geothermal Congress in 2010 confirmed that geothermal energy resources have been identified in over 90 countries and 78 of them utilize geothermal resources. Installed geothermal electric power was about 10 GW in 2011,

producing 67 TWh/y of electricity [3]. Fig.1.5 shows the top five countries producing geothermal electricity in the world in 2011.

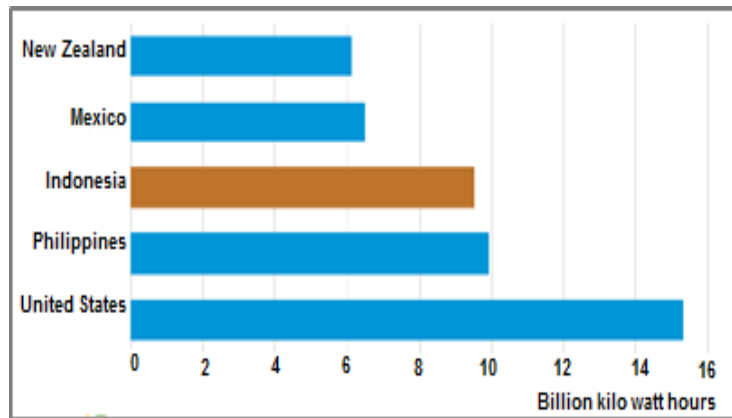


Figure 1.5. Top five generator of geothermal electricity, 2011 [1-2].

Indonesia is the third-largest geothermal energy generator in the world, behind the United States and the Philippines. Indonesia is developing country which is endowed with good geothermal resources due to it located on the Ring of Fire gives big potential of geothermal energy. 276 locations with geothermal energy potential had been identified that is estimated to have resources sufficient to generate 29 GW of electricity, which equates to 40% of the world's geothermal reserves, but only 10% of which is currently being used. (Fig.1.6).



Source: Geological Agency, 2010

Figure 1.6. Indonesia geothermal potential resources and prospect status map. (a-g) the location of existing geothermal power plant.

Seven fields that generate 1.197 MW of geothermal electricity have been developed. Three fields are under construction and another two fields have been explored which mainly located in Sumatera and Java. Those existing geothermal power plants are shown in Fig. 1.7.

Geothermal energy production is quickly becoming a power house on the alternative energy scene. The country added 130 megawatts (MW) of geothermal capacity in 2012. Recently the Indonesian government has completed a *Blue Print* on the development of geothermal energy of more than 6000 MW up to the year 2020 and it to be operated primarily by Indonesian electricity company (PERTAMINA) [4]. It means that Indonesia is likely to be a ‘*geothermal super power*’ in the future.



Figure 1.7. Existing geothermal power plant in Indonesia located in Sumatera, Sulawesi and Java Island.

Optimum utilization of geothermal energy will significantly reduce dependence on fossil fuel, reduce greenhouse gas (GHG) emission and improve national energy security. However, the utilization of geothermal has not been without technical and environmental problems. On the technical side, the most common problems have been related to the chemistry of the geothermal fluids which sometimes contain quite considerable concentrations of minerals and gases. Many of these technical problems can be solved, or minimized at least, by

improved well design and well operation, proper material selection and chemical treatment of the geothermal fluids, including use of chemical inhibitors.

It is estimated that nearly 3% of the global domestic gross product, corresponding to 2.8 trillion US dollars, is wasted every year with problems related to corrosion [5]. About 90% of the corrosion costs are associated with iron-based materials. Since carbon steels, which account for about 85% of the annual worldwide steel production, represent the largest class of iron alloys in use, the corrosion of such materials is of paramount importance. Notwithstanding many years of intensive research and development, there is not available an ideal protection method. A convenient method to protect metals is by the use of physical barriers against species such as water, oxygen, hydrogen and chloride.

On the other hand, since the plant is an independent power producer (IPP) project, low capital cost and reliable operation with high efficiency are essential from an economical point of view. The plant has several distinctive characteristics including large-capacity turbine, two-phase flow pipelines with central separators, and integrated pressure control designated to meet such requirements. It is well known that larger capacity means higher efficiency for a power plant steam turbine. Therefore, the performance of the steam turbine components is strongly dependent on their resistance to oxidation, since the formation of oxide scale causes a reduction of the thickness of the walls.

Major issues in the area of materials development are increased lifetime, reliability and safety of engineering components of electric power plants as well as environmental impacts like improved degree of efficiency and consequently reduced fuel consumption. To meet the need, design or select an appropriate of material commonly used for steam turbine and pipeline component should be considered.

## **1.2 Objectives**

The main purpose of the present study is to obtain detailed and advanced material characterization results to improve carbon steel performance under corrosive atmosphere. In general, the objective of this work is to study:

- ✓ Optimum coating condition on carbon steel substrate.
- ✓ Oxidation behavior of the coated samples.
- ✓ Evaluation meta-stable alumina formed during oxidation
- ✓ Corrosion behavior of the coated piping components.

### **1.3 The structure of the thesis**

The present thesis is divided into eight chapters. The first one describes the background of the study to reduce CO<sub>2</sub> emission by improving the efficiency of coal-fired power generation and related to the development scenario of geothermal power plant in Indonesia as a prospective renewable energy in the future. The second chapter introduces the required material, operational challenges, and process of development a protective coating in power plants and gives details on the general aspect of oxidation or corrosion mechanism. The electroplating and pack cementation coating techniques are also detailed, as well as the temperature constraints for this process. The third chapter is dedicated to the presentation of the materials investigated and the experimental methods involved for the development of coatings, the oxidation, corrosion and the hardness tests, as well as the techniques required for characterizing the coatings and the oxide products. Chapter 4 gives details of the experimental results on effect of cobalt content on hardness properties, micro-structural change and oxidation performance. Emphasis was placed on the coating development at different temperature in chapter 5. Comparison of the oxidation resistance of coated and uncoated carbon steels is reported. The study about the formation of meta-stable alumina on the coated layer after isothermal oxidation is described in chapter 6. The implementation of the coating process to the piping component and the characterization by non-destructive technique is presented in the chapter 7. The performance of the coated carbon steels and general summary drawn from the present work are discussed in chapter 8, which gives further details about the applicability of the presently developed coatings in power plants system.

## Chapter 2

### Material Issues for Power Plant System

#### 2.1. Material used in power plant

Use of steel products with high quality and reliability are critical to improve the energy efficiency and assure the safety of equipment and facilities in energy industry. Steel products are widely used in plants for production and use of energy resources, represented by fossil fuel. Steel materials are used in various forms and must provide high levels of performance and quality.

Fig. 2.1 shows where in an A-USC (advanced ultra-supercritical) boiler the various materials under development are used. Ferrite, austenite, Ni or Fe-Ni based alloy materials are used in the tertiary heater, final heater, secondary re-heater, main steam pipes, high-temperature reheat steam pipes, and other high-temperature components.

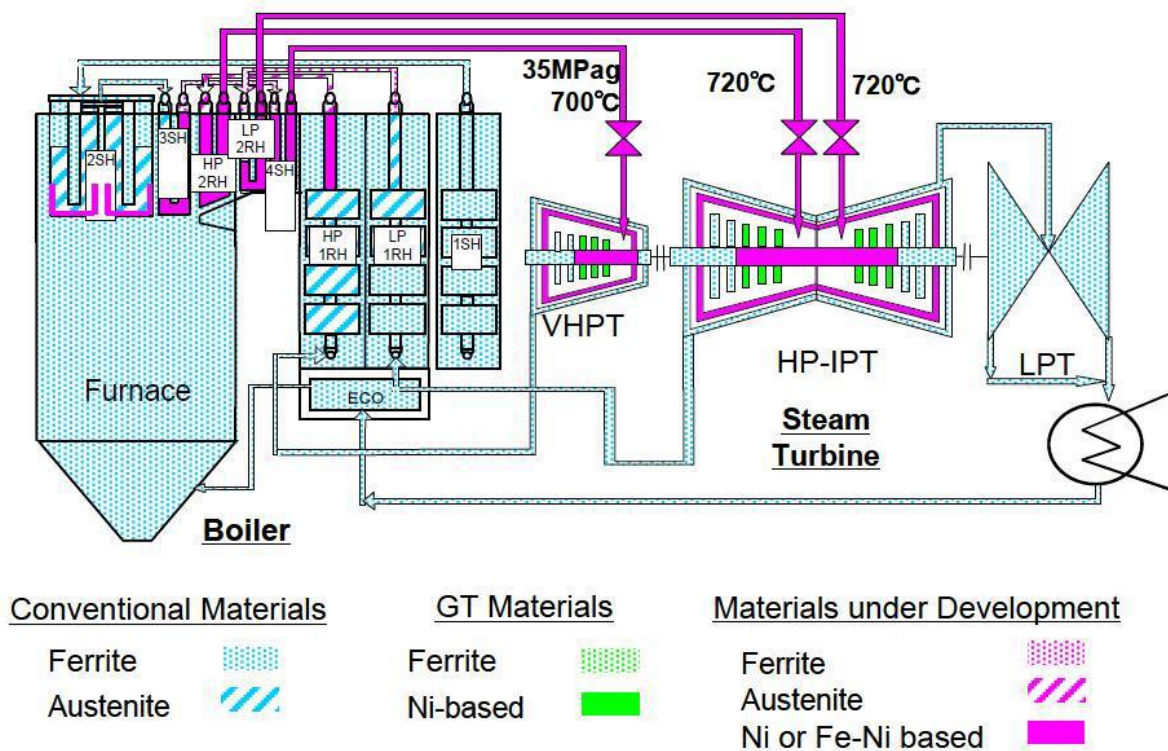


Figure 2.1. Uses of A-USC boiler materials [6].

On the other hand, the selection of materials for the construction of geothermal wells and fluids (liquid, steam or both) installation is one of the factors of importance in the original

design of geothermal utilization schemes which are expected for long service life. Steel is now the most widely used material for geothermal transmission lines and distribution networks; especially if the fluid temperature is over 100 °C. Other common types of piping material are fiberglass reinforced plastic (FRP) and asbestos cement (AC) as shown in Fig. 2.2.

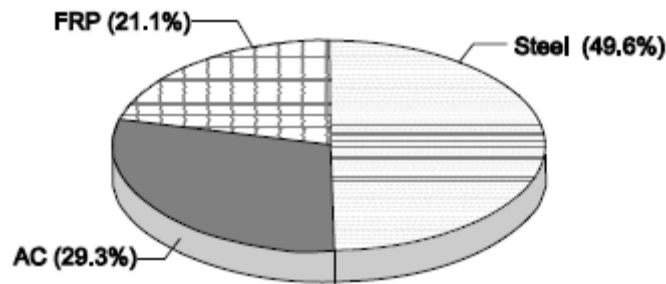


Figure 2.2 Distribution of piping used in geothermal system [7].

One of the factor that steel is widely used for this application is due to the temperature operation limit is higher than the other materials as described in Fig. 2.3. The properties of steel make them attractive construction materials for geothermal power plant. However, the reliability of these steel depends upon their application in the power plant.

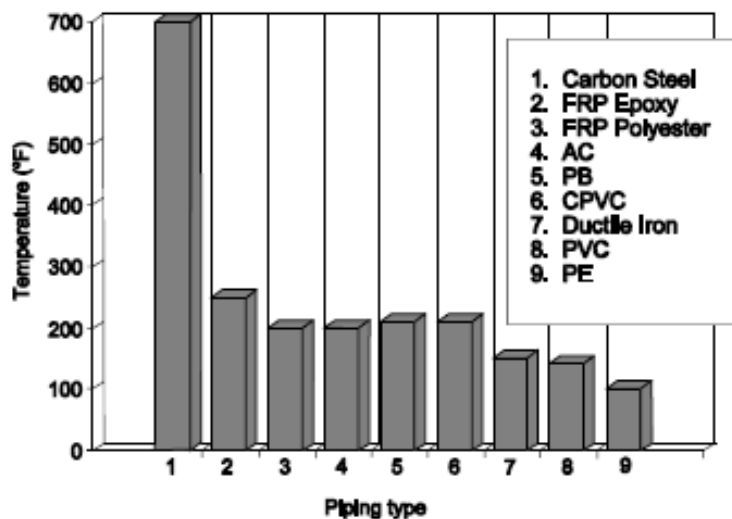


Figure 2.3. Maximum service temperature for pipe material [7].

## 2.2. Operational challenges in steam engine and piping component

The steam side oxidation of super-heater and re-heater materials coal-fired power system is one of the one major limiting factor in materials selection for supercritical boilers.

Steam-side oxidation occurs usually in the super-heater and re-heater section, where the materials are exposed to highest steam temperatures. The oxide scale formed on the steam-side may lead to major failures and thereby reduced plant availability. There are three different failure types which may be recognized due to steam-side oxidation. First, the wall loss of the tubes caused by oxidation may increase the hoop stresses and cause premature creep failures in the heat exchanging tubes. Second, the insulating oxide scale may lower the thermal conductivity, resulting in increased metal temperature and thereby accelerated creep and corrosion processes. The third concern is that if the oxide scale on the steam-side become increasingly thick, it will spall more easily. The spalled oxide scale particles may lodge in the steam circulation and cause tube blockages, or if they enter the steam the steam turbine, cause erosion in turbine blades and nozzles.

Corrosion is a major concern with steel piping, particularly in geothermal applications. Y. Kurata et al. reported on several corrosive species in a geothermal environment, geothermal fluids contain H<sub>2</sub>S, CO, other gases and ions, then materials of geothermal facilities are often damaged in various by these corrosive substances. In addition, the materials are damaged due to collisions with solid particles formed by precipitation of the dissolved substances the fluids, and are also damaged by high temperatures as well as high pressures of the fluid. By taking appropriate precautions, the primary corrosion modes for each of several classes of metal are discussed and summarized in Table 2.1. Furthermore, Table 2.2 shows the outline of the material failures at the respective facilities. It occupies 28% of the total number of damages in wells and pipelines. The erosion-corrosion (25.4%) happens at the pipes for two - phase flow which in high velocity, and also at the elbows and well head silencers where the flow direction and velocity turn abruptly with change of the cross-sectional area in its path. There comes stress-corrosion cracking (10.2%) which happens to a coupling section of casing pipes when used under and H<sub>2</sub>S, CO, existing environment.

Table 2.1. Forms and causes for metal in geothermal system and ways to prevent attack [8].

<b>Material</b>	<b>Major form of corrosion</b>	<b>Main environmental factor</b>	<b>Limits and precautions</b>	<b>Other comments</b>
<i>Mild and low alloy steel</i>	uniform	pH	Rapid rate increase below pH 6	Air in leakage is a major hazard; local flashing in pipes can cause very high flow rates and erosion/corrosion;
		Chloride	Rapid rate increase above 2% Cl <sup>-</sup>	
		Flow velocity	Limit flow 5 to 7 fps	

				avoid direct impingement on steel
	Pitting, crevice	temperature	Susceptibility increases with increasing temperature and chloride concentration	avoid mechanical crevices
		Chloride		
		Scale	Remove scale; avoid deposits	
	Sulfide stress	H <sub>2</sub> S	Can occur at very low H <sub>2</sub> S level	Complex interaction
	Cracking	Yield strength (hardness)	Use low strength material	
		Temperature	Hazard greater at lower temperature	
	Hydrogen blistering	H <sub>2</sub> S	Used void free material	Possible at very low H <sub>2</sub> S concentration
	Galvanic coupling	Electrical contact with more noble metal	Avoid coupling close to large area of cathode metal	More severe when material has porous coating or scale
<b><i>Stainless steels</i></b> <b><i>Ferritic alloys</i></b>	Pitting, crevice	chloride	In general susceptibility increase with increasing concentration and temperature	Lower alloys may also have high uniform rates in severe environment; O <sub>2</sub> is a hazard; Higher alloys are much more resistant
		scale	Avoid scale deposits	Cr and Mo most effective alloying agents
		Stagnant or low flow	Avoid stagnant or low flow condition	
		oxygen	O <sub>2</sub> greatly increase susceptibility	
	intergranular	Chloride, temperature	Avoid by proper welding and heat treating procedures	
<b><i>Stainless steels</i></b> <b><i>Austenitic alloy</i></b>	Stress corrosion cracking	Chloride	Complex interaction; depending on other factors; cracking can occur for Cl <sup>-</sup> > 5 ppm; O <sub>2</sub> – 100 ppb; T > 60 °C.	Hazard increase with increase in Cl <sup>-</sup> , O <sub>2</sub> ; T; some alloys more resistant; protect exterior surfaces.
		Oxygen		
		Temperature		
	Pitting, crevice	Chloride	*same as ferritic	Resistance increase with

				Mo content; avoid mechanical crevices
		Temperature		
	intergranular	scale	Avoid scale deposits	
		Stagnant or low flow	Avoid stagnant or low flow condition	
		oxygen	O <sub>2</sub> greatly increase susceptibility	
		Chloride, temperature	Avoid by proper welding and heat treating procedures	

Table 2.2. Percentage of material failures [9].

Type	General corrosion	Erosion- corrosion	Crack	Pitting	Scaling	Others	Unkown
a	28	25.4	10.2	3.4	23.7	6.8	2.5
b	12.4	19.1	20.3	3.4	1.1	24.6	19.1
c	24.2	11.6	6.4	5.2	-	52.6	-

(a) Well and pipeline, (b) drilling, and (c) well logging facilities.

### 2.3. Protective coatings

Due to the extreme conditions experienced by the components in coal-fired and geothermal power plant, protection against adverse effects is required in order to maintain component integrity and overall engine performance. As a result, an extensive use of surface engineering is required in order to combine the optimum bulk properties with the required surface protection. Surface engineering plays an important role in the operation of all high temperature components in a steam engine. In its simplest form it improves the environmental resistance of the components; as the improvement in mechanical properties of the structural alloys was made at the expense of the environmental resistance. Such coatings are normally applied to higher strength structural alloy substrates.

The selection of a suitable treatment or coating for a given application depends on complex interplay of surface, coating and substrate related properties that are defined by the specific application. Table 2.3 illustrates a summary of the desirable features and forms the frame work around which the design requirements of a coating for a good oxidation/corrosion resistance can be discussed.

Table 2.3. Desirable features of an oxidation / corrosion resistance coating [10].

Coating Property	Requirement	Coating Location		Coating / substrate interface
		Surface	Bulk	
Oxidation / corrosion resistance	Low rates of scale formation	√		
	Uniform surface attack	√		
	A thermodynamically stable surface oxide	√		
	Ductile surface scales	√		
	Adherent surface scales	√		
	High concentration of scale forming elements within the coating to act as reserve for scale repair	√	√	
	Microstructures must be tailored to eliminate any fast diffusion paths.	√	√	
Thickness	Coatings must be sufficiently thick to successfully protect structural materials from undesirable environmental interactions occurring over proposed mission lifetimes.		√	
Interface stability	Low rate of diffusion across interface at operating temperatures.			√
	Limited compositional changes across interface.			√
	Absence of embrittling phase formation during service.			√
Good adhesion	Matched coating and substrate properties to minimize coating mismatch and stress generation at coating/substrate interface.		√	√
	Optimum surface condition before coating.			√
	Growth stresses during coating formation should be minimized.		√	√
Mechanical strength	Coating must withstand all stress (creep, fatigue and impact loading) that is generated at component surface during service.		√	
	Well matched surface expansion coefficients between coating and substrate to minimize thermal stressing and thermal fatigue.		√	√
Environmental	Any coating material must have a suitably low vapor pressure to minimize sublimation and contamination of the working gas.		√	
	Application of coatings should not expose substrate materials to adverse environmental contaminants.		√	

	Coating materials must be thermodynamically stable with respect to the working gas and other materials in contact with the gas.		√	
--	---	--	---	--

The primary aim of coating or surface treatment for high temperature operating components is the ability to form thermodynamically stable, slow growing surface oxide capable of separating the coating alloy and the environment. This is why most coatings contain the three key elements of aluminum, chromium and silicon [10]. However, not only oxidation and corrosion resistance are important but also mechanical properties, adhesion and metallurgical stability must be kept in mind when designing a coating.

### 2.3.1. The concept of overlay coating

Overlay coatings are deposited onto the component surface. Overlay coatings used in steam engine are a family of corrosion/oxidation resistant alloys specifically designed for high temperature surface protection and are often referred to as M-Cr-Al-Y, where M is the alloy base metal, usually nickel, cobalt or an iron based alloy [10].

As stated by Nicholls [10], Talboom [11] published the first paper on the electron beam physical vapour deposition (EB-PVD) of a number of cobalt based MCrAlYs (CoCrAlY) in 1970. Electron-beam physical vapour deposition (EB-PVD) was the first method used to deposit MCrAlY coatings [12]. However, due to cost considerations, coating manufacturers soon developed techniques such as air, vacuum and low pressure plasma spraying (APS, VPS and LPPS) and high velocity oxy fuel (HVOF) deposition techniques.

MCrAlY overlay coatings are also frequently used as bond coats where they are applied to increase adherence of the outer ceramic layer of thermal barrier coatings (TBC). The primary function is to increase the high temperature oxidation and corrosion resistance of the underlying structural alloy.

### 2.3.2. Metallurgy and application of MCrAlY coatings

MCrAlYs (where M= Ni, Co) were initially developed in the 1960s based on a FeCrAlY system [11-13]. The overlay coatings (MCrAlYs) provide increased flexibility of design with compositions tailored specifically for different applications. MCrAlYs can be divided into several groups depending on the metal used. Some of the more important groups are: NiCrAlY, CoCrAlY, CoNiCrAlY, NiCoCrAlY. In each group the metal which is presented first, e.g.

cobalt in CoCrAlY, is the base metal and has the highest percentage in the composition. However NiCrAlY coatings are generally the most oxidation resistant, while CoCrAlY systems provide better hot corrosion resistance [14]. Generally, under high temperature oxidizing conditions NiCrAlYs and NiCoCrAlYs outperform the cobalt base systems. This is illustrated schematically in Figure 2.4.

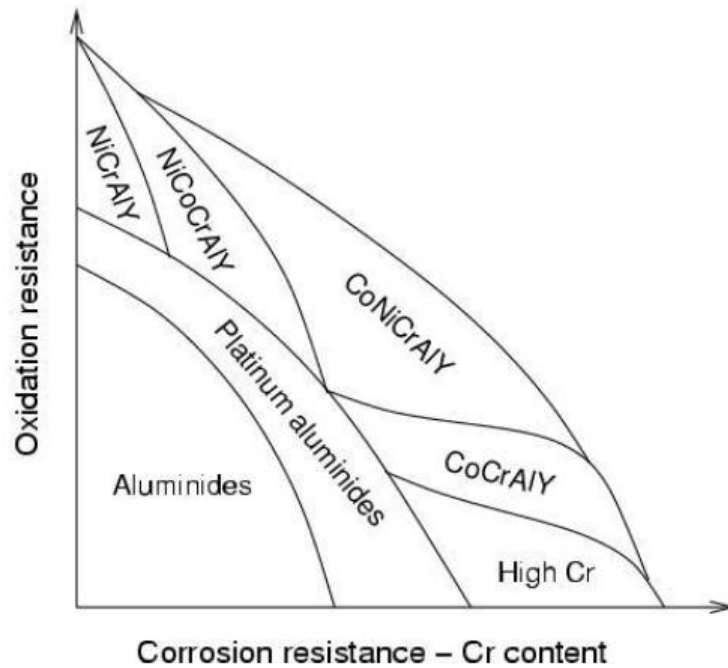


Figure 2.4. Relative oxidation and corrosion resistance of high-temperature coating systems [14].

To have a better understanding of the differences in performance of MCrAlYs, it is essential to understand the role of each element plays in these coatings. With the help of diagrams in Fig. 2.4 and better understanding of the behavior and role of each element in the coating, better designs and composition of MCrAlYs are possible (composition of the MCrAlY system is selected to give a good balance between oxidation and corrosion resistance, and coating ductility).

### 2.3.3. Role of alloying element

MCrAlY overlay coatings typically contain four elements or more. The role of these alloying elements is described as follows:

#### *Aluminum (Al)*

Aluminum has the greatest effect on the oxidation resistance. It forms the stable  $\alpha$ - $\text{Al}_2\text{O}_3$  which is a slow growing protective oxide. This effect of Al generally increases with its concentration. However, too much increase in its content can result in significant reduction of ductility of the MCrAlY, nevertheless it should be sufficiently high enough to develop and maintain an alumina layer and prevent subsequent breakaway oxidation [15]. Aluminum contents of 10-12 wt.% are typical. Aluminum, alloys with Co or Ni to form  $\beta$ -(Co,Ni)Al which readily forms the protective  $\alpha$ -alumina scale and provides a reservoir from which the alumina scale can be replenished.

### ***Chromium (Cr)***

Chromium not only improve hot corrosion resistance, but also increases the activity and diffusivity of aluminum meaning less aluminum is required for forming and maintaining the protective alumina oxide scale. This will result in an increase in ductility. Chromium also effectively reduces oxygen diffusion into the alloy by lowering the oxygen activity at the oxide scale-alloy interface [15] and is also found to stabilize  $\alpha$ - $\text{Al}_2\text{O}_3$  in preference to  $\gamma$ - $\text{Al}_2\text{O}_3$  [16]. It should be noted that  $\text{Cr}_2\text{O}_3$  decomposes into volatile  $\text{CrO}_3$  at temperatures above 900 °C [17].

### ***Cobalt (Co)***

Generally the oxidation resistance increases as the cobalt concentration decreases [16]. It alloys with aluminum producing the  $\beta$ -CoAl and provides improved sulphidation resistance. It can be readily substituted for nickel.

### ***Nickel (Ni)***

Nickel forms a series of high melting point phases such as  $\gamma$ -Ni,  $\gamma'$ - $\text{Ni}_3\text{Al}$  and oxidation resistant  $\beta$ -NiAl. It has also been reported that adding nickel to a ternary alloy of Co-Cr-Al can possibly reduce the process of interaction between the coating and the superalloy [18].

## **2.3.4. Multi-layer method of NiCoCrAl coatings**

As previously mentioned in section 2.3.1 that the methods for depositing MCrAlY overlay coatings include thermal spraying, CVD (chemical vapor deposition) and PVD (physical vapor deposition) methods [19-20]. In the present study NiCoCrAl is diffusion-coated by electrodeposition to create a NiCo coat followed by pack cementation with Cr and Al as illustrated in Fig. 2.5. These two methods are metallic coating to protect the carbon steel

substrate and they are selected because a simple process, can deposit material on complex shaped substrate, cost-effectiveness and have potential to scale up [21].

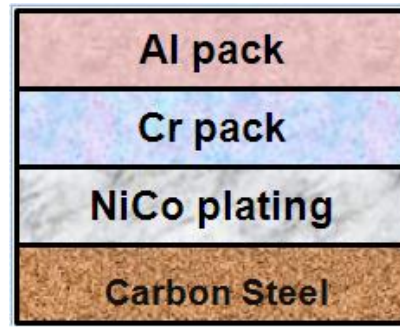


Figure 2.5. Schematic representation of NiCoCrAl multi - layer coatings on carbon steel substrate.

### ***Electroplating***

Nickel electroplating is utilized in large number of applications due to its advantages such as strength, toughness and resistance to corrosion/wear. Its mechanical properties can be varied by altering the electrolyte composition and operating parameters. It can also be varied by incorporating other metallic elements and ceramic particles/fibers within the electrodeposited nickel matrix. The applications of such deposits fall basically into three main categories: decorative, functional and electroforming [22]. Hard and low stressed nickel coatings have been obtained with the use of sulphur containing organic additives like saccharin, naphthalene trisulphonic acid and dibenzene sulphonic acid [23]. These organo-sulphur compounds were found to induce sulphur embrittlement when these coatings were subjected to high temperature applications. On the other hand, co-deposition of cobalt with nickel hardens the nickel in a sulphur free form by forming a solid solution. This solid solution does not embrittle on heat treatment. Moreover, the hard Ni–Co deposits are more ductile than those hardened by sulphur containing additives [23-24]. Ni–Co alloys have been studied extensively for magnetic applications especially in micro-system technology for the manufacture of sensors, actuators, micro relays and inductors [25-26]. These alloys have been deposited from a variety of simple and complex baths [27–29]. Highly tensile stressed deposits are prone to get cracked when these electroplated articles are subjected to mechanical strains; hence it is desirable to obtain a low stressed deposit [23]. Electrodeposition from sulphamate bath is preferred to obtain low stressed deposits.

Investigations on electrodeposited Ni–Co alloys have indicated that their properties strongly depend on the cobalt content. The amount of cobalt in the Ni–Co deposit can be

controlled by experimental parameters, such as electrolyte composition, pH, current density, temperature and stirring speed [29-30]. The effect of these parameters on the mechanical properties such as hardness, strength, residual stress and magnetic properties has been dealt in detail in the literature [23-29].

### ***Pack Cementation***

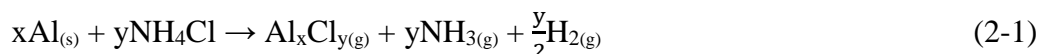
Pack cementation is an extended CVD method in which the substrate to be coated is introduced in a retort and surrounded by a powder mixture, which is composed of the source alloy(s), an activator and an inert filler. The retort is then heated to the desired coating temperature usually under inert or reducing environment. In these conditions, the source element reacts with the activator forming a gaseous transporting species. This diffuses through the pack to the substrate surface where it decomposes, allowing the metallic element to be deposited to penetrate into the substrate by solid state diffusion. As for all diffusion coatings, the microstructure is highly dependent on the substrate, which is coated. For this reason, process conditions have to be optimized for each material.

Typically the powder pack mixture consists of 3 components:

1. A metallic source M: a fine powder of the element(s) to be deposited on the surface of the substrate (Al, Cr, Si, Ti or combinations of these elements)
2. A halide salt activator as for example: NaCl, NH<sub>4</sub>Cl, AlCl<sub>3</sub>, NaF, NH<sub>4</sub>F.
3. An inert filler powder (e.g. Al<sub>2</sub>O<sub>3</sub>) preventing the powder mixture from sintering at high temperature.

Fig. 2.6 illustrates the major chemical reactions involved in the general pack cementation process. In order to allow a better understanding of the following paragraph, the reactions are written for the particular example of aluminizing iron activated by NH<sub>4</sub>Cl. The whole process relies on the formation of gaseous halides according to the general reaction:

#### Formation of gaseous halides



AlCl<sub>3(g)</sub>, AlCl<sub>2(g)</sub>, AlCl<sub>(g)</sub>, Al<sub>2</sub>Cl<sub>6(g)</sub> or Al<sub>2</sub>Cl<sub>4(g)</sub> are the chlorides involved in a chloride activated aluminizing process.

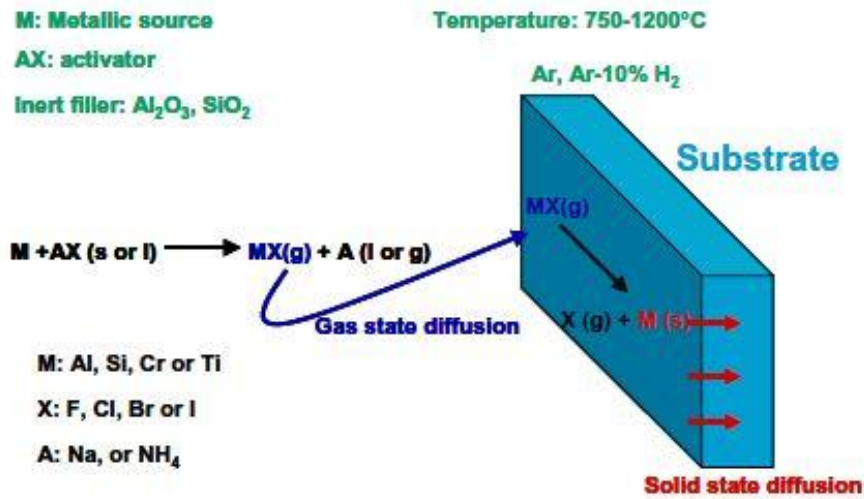


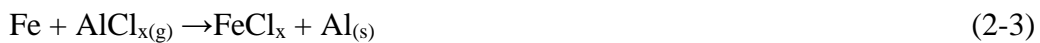
Figure 2.6. The main chemical reactions involved in the pack cementation process [31].

The partial pressures of each of the gaseous halides formed are established by their thermodynamic stability, which varies with the process conditions: composition of the pack, type of activator, temperature, pressure, and type of inert or reducing environment. In the case of aluminum deposition, AlCl<sub>3(g)</sub> is the major halide formed at low temperature, whereas at higher temperature the activity of AlCl<sub>(g)</sub> becomes higher. Once they are formed the halide molecules diffuse through the gas phase to the substrate (e.g. iron) surface, where they adsorb and decompose owing to the general reactions:

Disproportionate of lower halides into higher halides



Exchange reactions



Reduction of the halides



Reaction of dissociation



By using alkaline or earth alkaline halide activators as for instance, NaCl, KCl or CaCl<sub>2</sub>,

the precipitation of the activator salt has to be considered also [31]:

#### Precipitation of NaCl activator



The aluminum formed at the surface of the substrate by reactions Eq. 2-2 to 2-6 can then diffuse into the solid substrate, forming the desired coating. The predominance of the reactions Eq. 2-2 to 2-6 depends first of all on the stability of the gaseous halides involved. The deposition particularly occurs by disproportionate reaction (Eq. 2-2) when, first, the vapor pressure of the substrate halide is low and when, secondly, the coating element has higher and lower halides of comparable vapor pressures in order to set atomic aluminum free. When the vapor pressure of the substrate halide becomes comparable to the gaseous species of the coating element, the contribution of the exchange reaction (Eq. 2-3) becomes important. The latter reaction even gets undesirable if the vapor pressure of the substrate halide becomes higher than the source supplier halide, as it would lead to a significant metal loss and to porous coatings. In a NaCl activated pack, this phenomenon can occur during chromizing or siliconizing of iron, whereas reaction Eq. 2-3 stays minimal during aluminizing [32].

The reader may at this point easily catch the compromise which has to be found. Because halide molecules must diffuse through the gas phase from the pack to the substrate, the coating composition depends on the gaseous halide activity and their stability or their ability to decompose at the substrate surface. Hence, the formation and the decomposition of the gaseous halide have to be optimized at the same time in the pack and at the substrate surface, respectively. Furthermore, it is a prerequisite that the thermodynamic activity of the incorporated element is always lower at the surface than in the pack [33]. This activity gradient drives the gas phase diffusion of the halide molecules from the pack to the substrate surface. As a consequence, a desired coating composition cannot be obtained by simply using a master alloy of the same composition [34]. Moreover, the concept of “major depositing species” has been defined. This corresponds to the gaseous species that is responsible for the major part of the deposition. In the case of a Cr-Al codeposition process by a chloride activated pack, Rapp et al. [34] and Da Costa et al. [35] showed that although the vapor pressure of  $\text{AlCl}_{3(g)}$  is several orders of magnitude higher than that of Cr halides and other Al halides, the codeposition is possible by optimizing the process conditions so as to get comparable vapor pressures of  $\text{AlCl}_{(g)}$  and  $\text{CrCl}_{2(g)}$ . Indeed,  $\text{AlCl}_{3(g)}$  is too stable and does not decompose enough at the substrate

surface. The Al transport occurs via  $\text{AlCl}_{(g)}$ . This is thus considered as the major transporting species for Al, whereas  $\text{CrCl}_{2(g)}$  is the major transporting species for the deposition of Cr [34].

#### 2.4. General aspects of high temperature oxidation

Oxidation is an environmental phenomenon in which metals or alloys exposed to oxygen or oxygen containing gases at elevated temperatures convert some or all of the metallic elements into their oxides [36]. The oxide formed can act as a protective scale if it remains adherent and so reduce further oxidation. However, if the oxide scale formed continually spalls off, it will expose fresh metal and thus results in progressive metal loss.

When the total chemical equation for the chemical reaction between a metal and oxygen gas to form the metal oxide is considered, oxidation of metals may seem to be among the simplest chemical reactions. However, the reaction path and the oxidation behavior of a metal can depend on a variety of factors, and reaction mechanisms may as a result prove complex.



Oxidation is generally studied by controlled exposure of metals to oxidizing atmospheres such as  $\text{O}_2$ ,  $\text{CO}_2$ ,  $\text{H}_2\text{O}$ ,  $\text{NO}_2$  or air at high temperatures for a various lengths of time. The purpose of oxidation experiments is generally to assess the reaction kinetics and the mechanism of oxidation of a metal or alloy under a set of exposure variables such as temperature, pressure, or gas composition.

When representing oxidation kinetics any of the above variables can be used and can be measured as a function of time, since they all result in an assessment of the extent of reaction.

The rate of formation of an oxide on a metal according to the reaction in equation (2-7) can be investigated by several methods [15]:

- *The amount of metal consumed:* in practice this may be assessed by observing either the mass loss of the sample or the residual metal thickness.
- *The amount of oxygen consumed:* This may be assessed by observing either the mass gain or the amount of oxygen used.
- *The amount of oxide produced:* This may be assessed by observing the mass of oxide formed or by measuring the oxide thickness.

### 2.4.1. Oxidation process

A metal will oxidize if the free energy ( $\Delta G^\circ$ ) associated with its reaction is negative. However, the free energy for a reaction is affected by a number of parameters which are as follow:

- Temperature
- Partial pressure
- Composition

The effect of temperature and oxygen partial pressure on the free energy of different material can be seen in the Ellingham diagram of Fig. 2.7. Composition also has a big effect on the free energy associated with an oxidation reaction, as it is usually assumed that the thermodynamic activity of metal(s) in a reaction is one ( $a_{Me}=1$ ). However, in the case of alloys, this is not true as the thermodynamic activity of different elements varies within an alloy. It can be seen in this plot, that the most stable oxide is alumina followed by titania, silica, manganese oxide and chromia.

### 2.4.2. Oxidation kinetics

The higher of oxidation rate means the higher of the oxidation damage. As a consequence, one way to quantify the oxidation damage is to measure the rate of the corrosive/oxidative reaction. This most often consists in measuring the mass gain due to the reaction between the metal and the corrosive gas.

Although it is essential to know the thermodynamic consideration of free energy change to determine the occurrence of an oxidation reaction, the kinetics of the reactions is also important. It has been found experimentally that several rate laws can be identified. The principal laws are as follow [36]:

- *The linear law*

The rate of reaction is independent of time, is found to refer predominantly to reaction whose rate is controlled by a surface reaction step or by diffusion through the gas phase.

$$\frac{\Delta m}{A} = k_p t \quad (2 - 8)$$

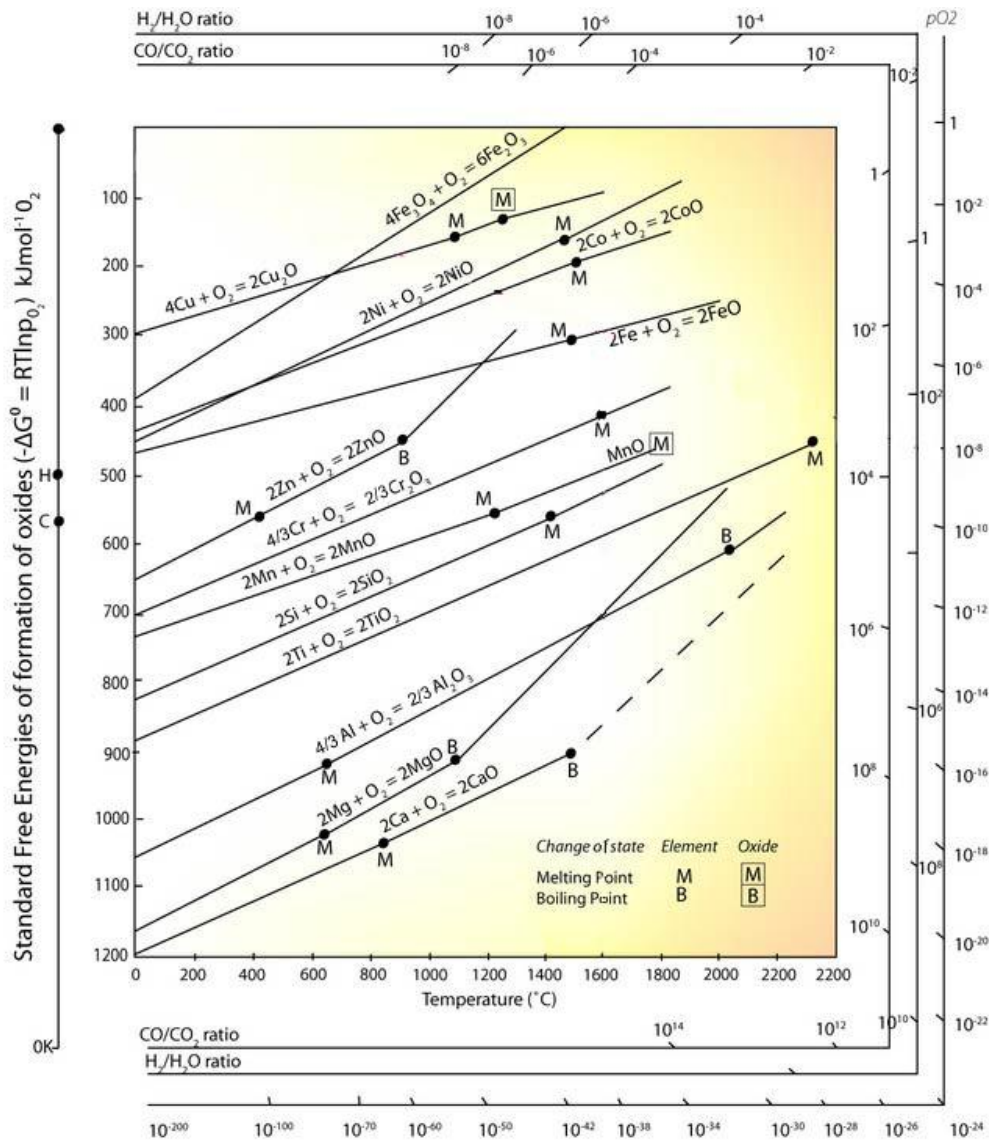


Figure 2.7. Ellingham diagram of free energy of formation of oxides as a function of temperature [24].

➤ *The parabolic law:*

The rate is inversely proportional to the square root of time, is found to be obeyed when diffusion through the scale is the rate determining process.

$$\left(\frac{\Delta m}{A}\right)^2 = k_p t \quad (2 - 9)$$

➤ *The logarithmic law:*

The formation of very thin films of oxides which are between 20 to 40 angstroms thick at

low temperatures.

where  $\Delta M$ ,  $A$  and  $t$  correspond to the mass gain of the sample, the sample area and the exposure time, respectively. Fig. 2.8 shows the different archetypes of mass gain curves. The curve *a* is a parabola. This type of kinetics is often observed, especially for pure metals when the rate of the oxide scale growth is dictated by ionic diffusion through the oxide scale.

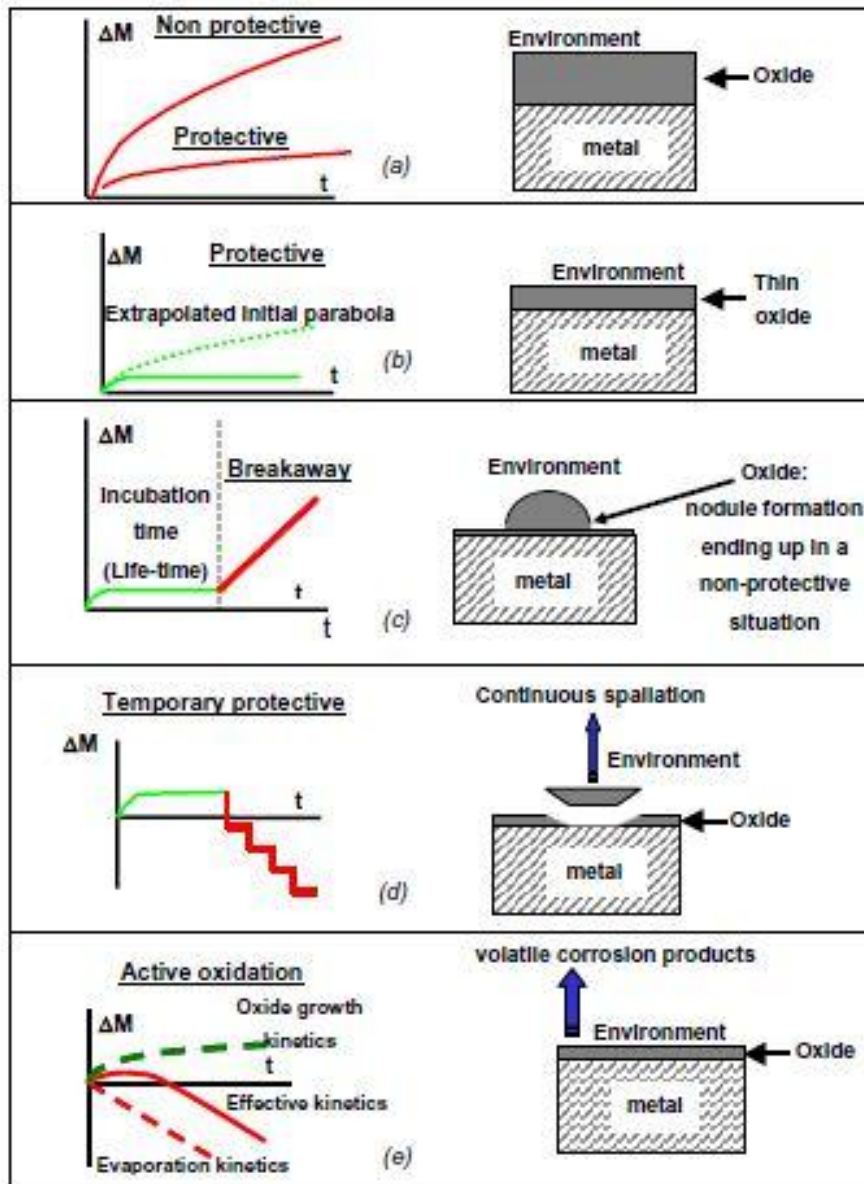


Figure 2.8. Different types of behavior for high temperature oxidation and corresponding mass gain curves. (a) Parabolic oxidation, (b) Sub-parabolic oxidation, (c) Breakaway oxidation, (d) Oxide scale spallation, and (e) Evaporation of volatile species.

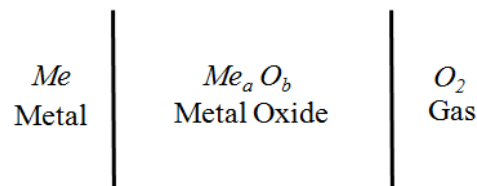
The comparison of  $k_p$  values allows the quantification of the corrosion rate. A small  $k_p$

represents a slow parabolic scale growth and thus a protective behavior (Figure 2.8a), whereas a high  $k_p$  corresponds to a higher reaction rate and a non-protective situation. Nevertheless, it has to be kept in mind that in particular on technical alloys, these parabolic kinetics in many cases, only occur after some transition time due to the simultaneous growth of different oxide nuclei, competing at the start of exposure. At the end of the transition regime, the oxidation kinetics is controlled by the slowest growing oxide, which leads to a drop of the oxidation rate. Consequently, the mass gain curve remains below the extrapolation of the initial parabola (Figure 2.8b). Following exposure will thus lead to sub-parabolic oxidation, which is protective. Curve *c* shows the situation called breakaway oxidation. At the beginning of exposure, the oxidation is protective. After some time the mass gain increases significantly, showing a transition from protective to non-protective oxidation. The prerequisite for breakaway oxidation is that underneath the oxide scale, the alloy depletes in elements that are forming the protective oxide. The concentrations in those elements can decrease even below the minimum concentration required for the formation of the protective oxide. Then two critical phenomena can occur, leading to breakaway. First, the oxide scale may only be protective until a critical incubation time, above which it starts cracking due to stresses arising from its growth [37]. At that moment, the corrosive gases penetrate into the crack through the oxide scale and come directly in contact with the depleted alloy. The latter further oxidizes but the resulting oxide is no longer protective. Consequently, a higher corrosion rate is observed. This first phenomenon is the so called mechanical-chemical breakaway. The second explanation is the exclusive chemical breakaway. In this case, the oxide does not crack but simply, the concentration of the alloying element, which forms the protective oxide scale, further drops to a level where the oxide scale becomes chemically instable. The protective oxide will be converted into non protective oxide characteristic for strongly depleted subsurface composition and leading to fast growing oxides: the breakaway. Another type of phenomenon is shown by curve *d* and represents spalling of the oxide scale. Indeed, the mass loss observed in some cases is attributed to cracking and spalling of the oxide scale due to either growth stresses, as mentioned earlier, or stresses arising from temperature changes. In the latter case, differences in the thermal expansion coefficients between the bulk metal and the oxide scale lead to the development of mechanical stresses in the oxide, for instance during cooling. These stresses can result in scale failure and spallation. A second explanation for the mass loss is the volatilization of oxide species (curve *e*), as it has been observed for example for chromium oxide in water vapor [38-41]. With respect to thermodynamic and kinetics considerations, a protective oxide scale can

thus be defined as a dense, homogeneous, adherent and slow growing scale that enables a long term protection of the underlying metal. It also includes the ability of healing the scale cracks by further oxidation during service [42].

### 2.4.3. Oxidation of alloys

Since some part of this research work is based on oxidation; some background to the oxidation of alloys is brought forward. From the consideration of equation (2-7) it is obvious that the solid reaction product will separate the two reactants as shown below:



It is clear that for the reaction to proceed further, one or both of the reactants must penetrate the scale. Therefore, the mechanisms by which the reactants may penetrate the oxide layer are an important part of the mechanism by which high temperature oxidation occurs. Since all metal oxides are ionic in nature it is not practicable to consider the transport of neutral metal or non-metal atoms through the reaction product [43]. Several mechanisms are available to explain the transport of ions through ionic solids which have been explained in details in references [43-44].

The basic mechanisms operating in the oxidation of pure metals are also operative in the oxidation of alloys with added complexity such as formation of multiple oxides, mixed oxides, internal oxides, and diffusion interaction within the metals [36].

To better understand the effect of oxidation in alloys, a binary AB model where A is the major component and B is the minor component is considered. Two distinct possibilities exist:

1. Element A is more noble and B is more reactive.
2. Both A and B are reactive to oxygen with BO more stable than AO.

In the 1<sup>st</sup> situation where element A is considered to be more noble and B to be more reactive, at atmospheric pressures of oxygen A does not form AO, whereas B converts to BO. Depending on the concentration of B in A; (i) the alloy is dilute in B, (ii) the alloy is concentrated in B. Where the alloy is dilute in B, oxygen will diffuse internally to oxidize and form dispersed precipitates of BO in A. Because there is not enough B available a continuous BO scale does not form. In the case where the alloy is concentrated in B, there is sufficient B

available and thus a continuous BO layer forms. This is shown schematically in Fig. 2.9.

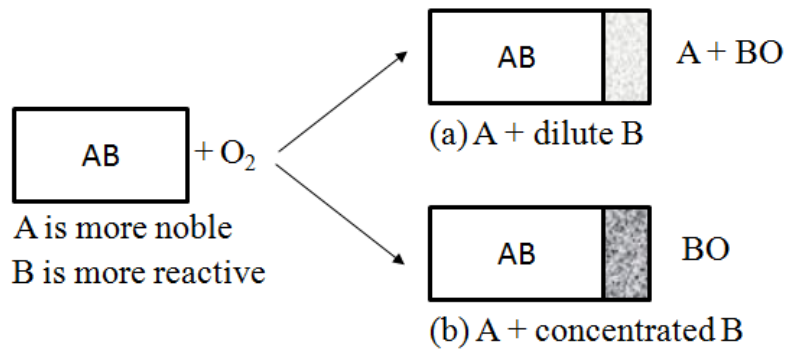


Figure 2.9. Binary alloy oxidation, component A is more noble and B is more active [36].

In the 2<sup>nd</sup> situation where A and B are both reactive to oxygen with BO being more stable than AO, the concentration of B again dictates the oxide morphologies. (i) The alloy is dilute in B; (ii) the alloy is concentrated in B. If the alloy is dilute in B a stable oxide AO forms as the outer scale. Below this scale at the AO-alloy interface, the oxygen activity is high enough to oxidize B into BO precipitates. If the alloy is concentrated in B, the concentration of B exceeds the critical level required to form a continuous BO scale. This is shown schematically in Fig. 2.10.

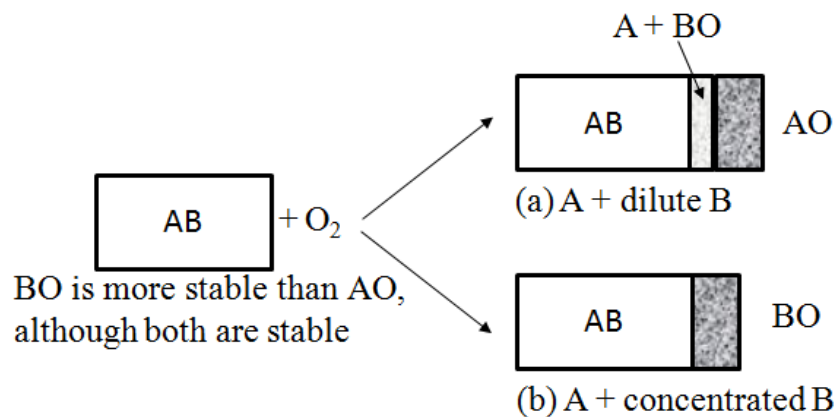


Figure 2.10. Binary alloy oxidation, component A and B form stable oxides but BO is more stable than AO [36].

The latter case is the basic model for creating oxidation resistant alloys and coatings (the process is known as selective oxidation where there is a preferential attack by oxygen on one of the components in the material). The oxide growth rate is parabolic, and the actual rate

of oxidation depends on how protective the BO scale is and on the presence of additional alloying elements [36].

Giggins and Pettit [45] have investigated the oxidation of Ni-Cr-Al alloys in the temperature range of 1000 to 1200 °C where a protective alumina layer can be formed. They analyzed a range of Ni-Cr-Al alloys with different Cr and Al contents, and found that a continuous external layer of Al<sub>2</sub>O<sub>3</sub> formed on a Ni-Cr-Al alloy at lower aluminum concentrations than would be necessary if Cr was not present in the alloy [45]. However, a sufficiently high amount of Al is required in order to form the continuous alumina layer. This has been reported to be in the range of 10 to 12 wt.% [45]. Higher Al content results in higher oxidation resistance. On the other hand, high Al contents can lower the ductility of the alloy. Hence, in order to have a high Al content for good oxidation protection and at the same time keeping the excellent mechanical properties, coatings such as MCrAlYs have been utilized. The composition of MCrAlY coatings (particularly the Al and Cr content) ensures they are chosen to be alumina formers, protecting the substrate from oxidizing environments whilst maintaining the excellent mechanical properties of the substrate.

## **2.5. Research and development of NiCoCrAl coating**

Fig. 2.11 shows the research road map of Ni-based coated layer on carbon steel substrate. The concept of MCrAlY overlay coating firstly applied on carbon steel substrate. The coating method used in the present study is combination of NiCo Electroplating and Cr followed by Al pack cementation. In the first year (FY2011), the effect of composition layer was comprehensively studied by developing four types of coated sample with different sequential process. By this investigation, the results showed that Al more appropriate on top layer than Cr after oxidation test at temperature of 800 °C [46]. This result was good agreement with the description in Fig. 2.4 which revealed that NiCoCrAlY composition had a relative oxidation and corrosion resistance. In the case of sample #1 in Fig. 2.11, NiCo layer beneath the Al layer was not pretend as oxygen barrier layer to the substrate due to the formation of NiO phase and it affected the formation of spinel structure instead of stable Al<sub>2</sub>O<sub>3</sub> protective layer. Therefore, the sequential layer of sample #4 in Fig. 2.11 with NiCo/Cr/Al showed better oxidation resistance than the other of three coated samples. NiCo as first layer forms a series of high melting point phases such as  $\gamma/\alpha$ -(Ni,Co),  $\gamma'$ -Ni<sub>3</sub>Al, Al<sub>3</sub>Ni and oxidation resistant  $\beta$ -NiAl and these formed phases can reduce the process of interaction between the coating and the substrate. Cr pack as second layer can increase the activity and diffusivity of Al, increase

in ductility and lowering the oxygen activity. Al pack as third layer acts as reservoir of oxide forming element and has the ability for self-healing of oxide layer. In other word, Al on top layer has good effect for oxidation because of  $\alpha\text{-Al}_2\text{O}_3$  with slow oxide scale formation. By understanding the arrangement of the coated layer, further experiment in the second year (FY2012) was focused on the variation of coating parameter in order to obtain the best coating performance. Different coating compositions provide different protective properties due to the nature of the different oxides growing on them. The composition of the alloy, as well as the exposure time and temperature, greatly influence the oxide layer created. On the other hand, a detailed characterization of the micro/nanostructure of the multi-layers formed on carbon steel substrate is required to improve the commercial performance of carbon steel and to obtain optimum conditions in accordance with the applications. In the third year, the implementation of the best coating condition was utilized to the carbon steel piping component and acid vapor corrosion test was carried out to simulate the actual condition in geothermal power plant application. Neutron radiography and tomography (NRT) was applied to observe the internal corrosion of the coated piping components. The method is very useful to understand the difference corrosion behavior of coated and uncoated carbon steel pipe without destructive technique.

Nano to macro scale characterization was applied to understand the material properties related to the structure of crystallized material. Fig. 2.12 shows the recent advancements made in nano to macro scale analytical technologies. These technologies enable scientists and engineers to obtain detailed information related to the crystal structure, phase, defect, morphology, elemental composition, etc [47-49] as described in Fig. 2.13. Therefore, recent development of material from laboratory design to applied science reach a great progress by combining the available technology for material characterization.

# Research Road Map

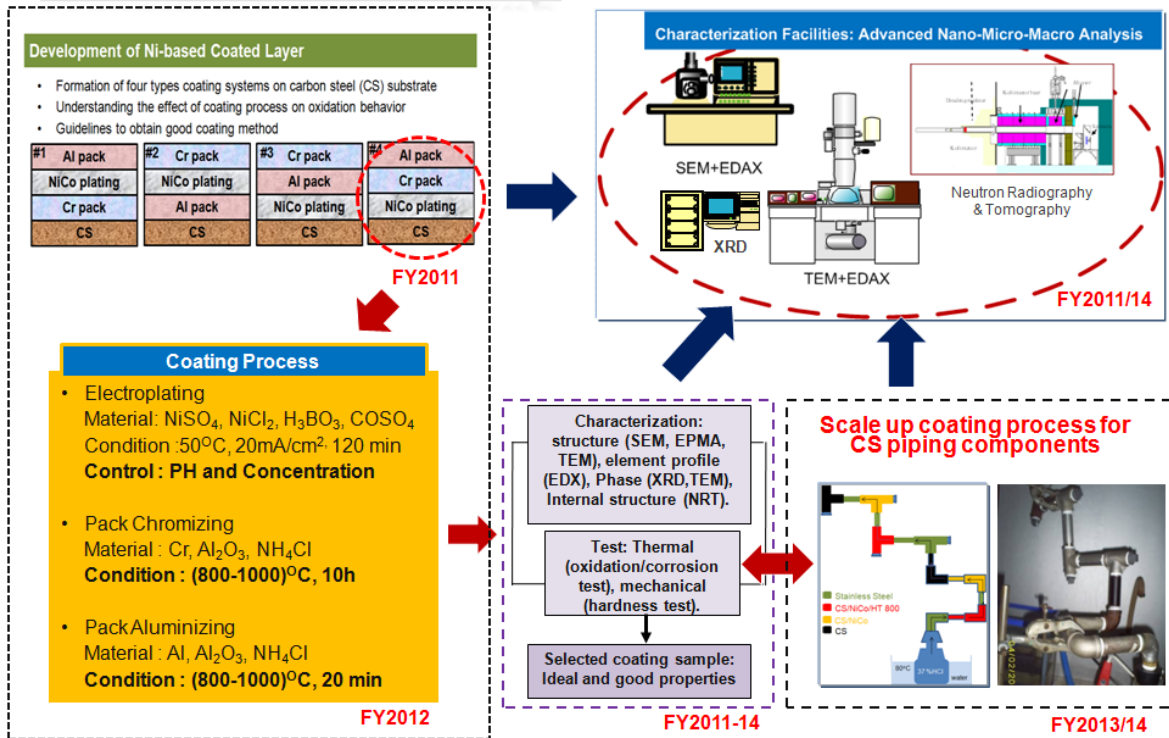


Figure 2.11. Research road map on the development of Ni-based coated layer on carbon steel substrate in geothermal power plant application.

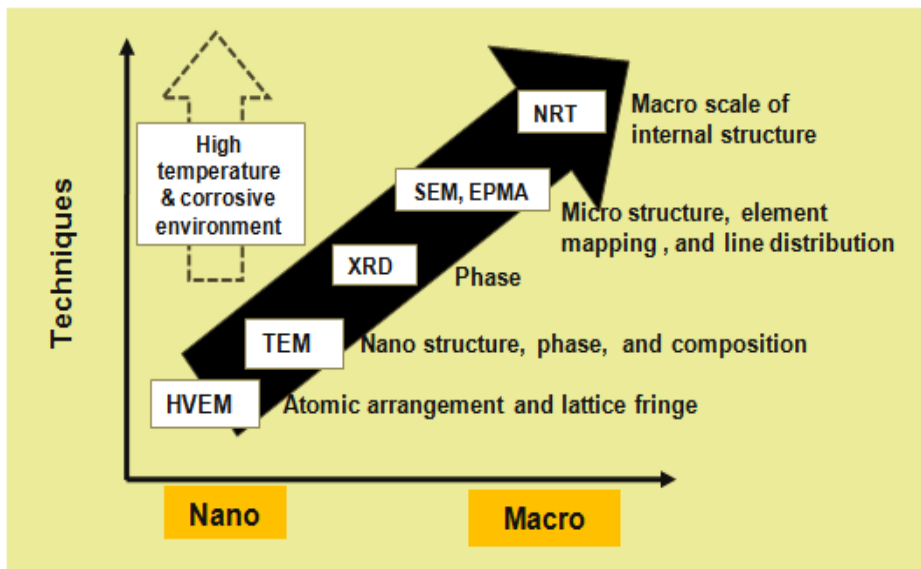


Figure 2.12. Recent advancement of nano - micro - macro scale applied in materials characterization. Case study: NiCoCrAl coated sample on carbon steel substrate.

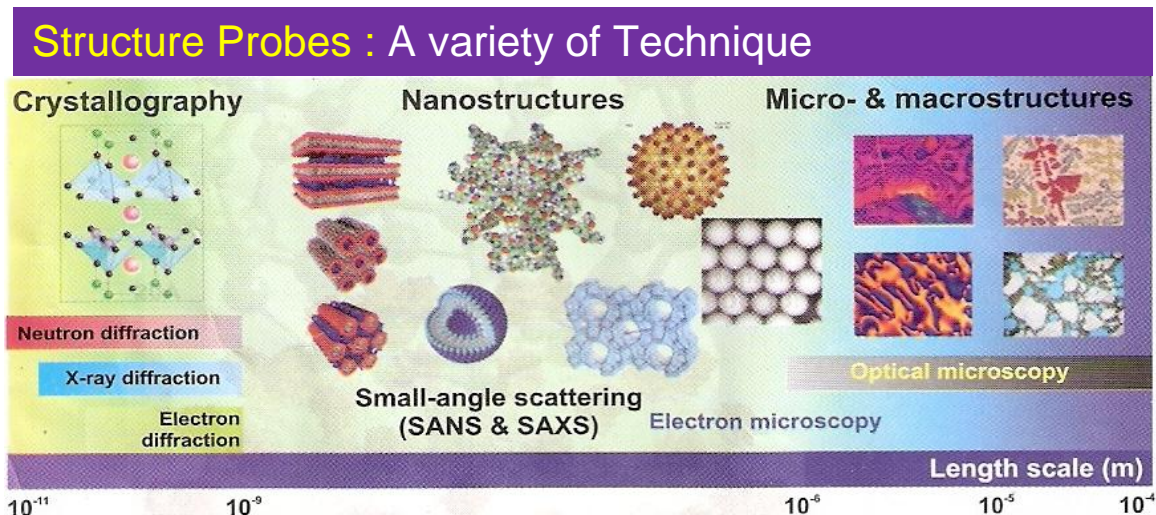


Figure 2.13. A variety of techniques can be used to probe complex structure [51].

Utilization of XRD and SEM which are commonly used in analyzing the phase formation and structure of the layer has been providing information for micro-scale [51]. However, in multi-layer coatings, it is not straightforward to determine the phase sequence from the substrate to the outermost layer due to the limitations of X-Ray analysis. The characterization of the coated layers requires the use of advanced analytical techniques, and especially cross-section transmission electron microscopy (XTEM) is always mandatory. The powerful of XTEM technique has been described comprehensively in previous work and enables resolving unknown structures in an Nb-Re-Cr ternary system [52]. Further, selected area electron diffraction (SAED) and high-resolution image (HRTEM) obtained from areas of interest in the coated layer was used to provide a detailed identification of the phase distribution in the coating. The results of these methods correlate well with crystal structure analysis of the phases within the coating. The information is crucially needed to understand the mechanism of coating formation and hence, the degradation of the layers can be prevented in the best way to extent the materials` life time [53].

New breakthroughs method in the field of material characterization will be conducted in this research using non-destructive method by neutron radiography and computed tomography which provides information about internal corrosion/oxidation that occurs in a macroscopic sample. In spite of its unique advantages, neutron scattering is only one of the techniques for probing the structures of materials. All of the techniques, such as x-ray scattering and electron microscopy, are needed if scientists are to understand the full range of structural properties of matter.

In most cases, the different methods used to probe material structure give complementary information because the nature of the interaction between the radiation and the sample are different. To a certain extent the method of choice depends on the length scale of the structure to be investigated (Fig. 2.13). When two techniques address the same scale, additional information, such as the size and chemical composition of the sample, is required to select the optimal technique.

## Chapter 3

### Methodology

This chapter covers the experimental procedure and equipment used during this study. Description of the material, coating process, mechanical and thermal tests as well as sample preparations for characterization technique are presented. A variety of characterization tools that used in the present study are also comprehensively described. The combination of all analytical methods is very useful to understand the characteristic of material in order to perform nano - micro - macro scale.

#### 3.1 Experimental procedure

The coating process was carried out by deposition of NiCo using electroplating technique on carbon steel substrate followed by Cr and Al pack cementation. The coating procedure follows the flow diagram as shown in Fig. 3.1.

##### 3.1.1 Material

The material used in the present study was a type of low carbon steel, namely ST-37 plate of dimension 15×10×1.5 mm. The chemical composition of this substrate is shown in Table 3.1.

Table 3.1. Chemical composition (wt%) of low carbon steel substrate.

Elements	Wt%	Elements	Wt%
C	0.17	Mn	1.40
S	0.045	Cr	0.1
P	0.045	Fe	96.24

### 3.1.2 Coating process

The specimens were ground using silicon carbide emery papers from grade 200 to 1200. Substrates for coating process were drilled and hung by steel wire, followed by dipping in acetone solution to remove greases, then rinsed in distilled water before being placed in an electrolyte solution. NiCo electroplating of the substrate was performed at two concentrations of cobalt, Ni(1 wt%)Co and Ni(5 wt%)Co. The compositions of the electrolyte solution baths containing nickel sulfate, cobalt sulfate, nickel chloride, and boric-acid as shown in Table 3.2. The reagents were dissolved in distilled water and the pH adjusted in the range of 3.6 - 3.8. Prior to the deposition of NiCo, the substrate was coated with a Ni-strike solution for 30 seconds containing nickel chloride and chloride acid as shown in Table 3.2.

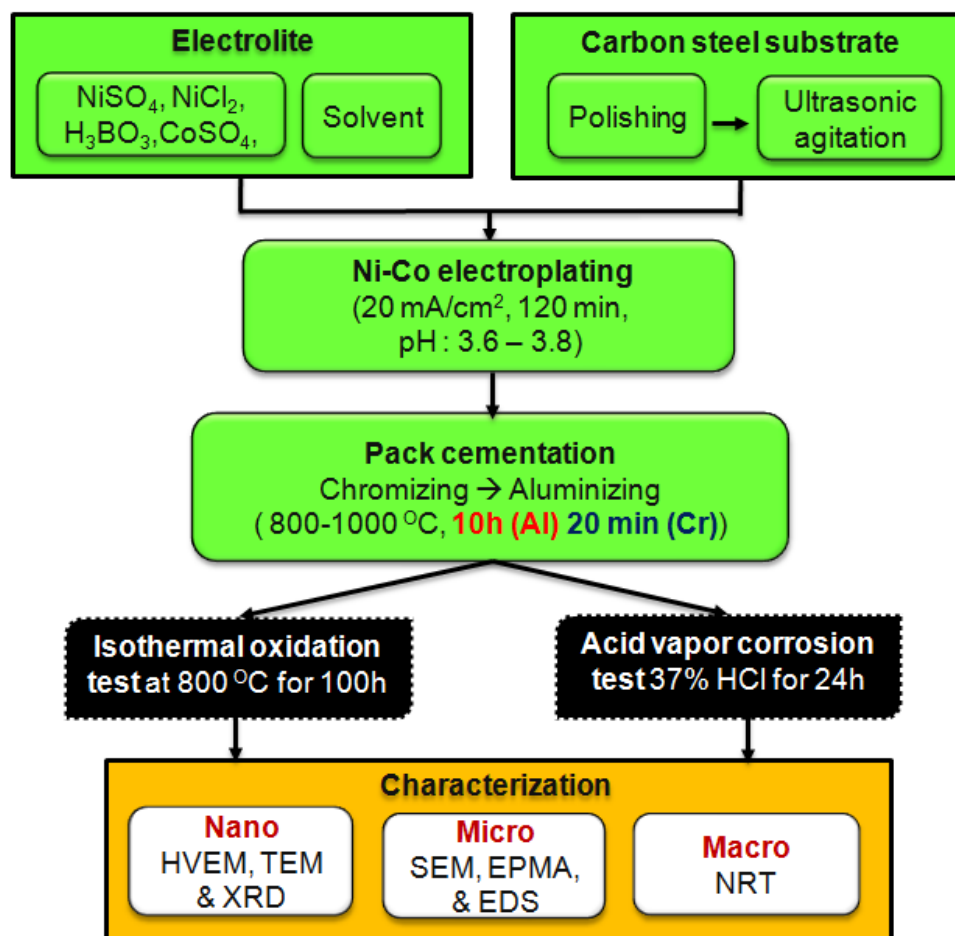


Figure 3.1. Flow diagram of the coating process and the characterization method.

Table 3.2. Formulation of Ni electroplating.

Ni-strike			NiCo-watts			
Chemical	Formula	Concentration	Chemical	Formula	Concentration (g/L)	
					1 wt% Co	5 wt% Co
Nickel Chloride	$\text{NiCl}_2 \cdot 6\text{H}_2\text{O}$	250 g/L	Nickel Sulfate	$\text{NiSO}_4 \cdot 7\text{H}_2\text{O}$	326.7	313.5
Chloride	$\text{HCl}$	125 ml	Cobalt Sulfate	$\text{CoSO}_4 \cdot 6\text{H}_2\text{O}$	3.3 L	16.5
Acid			Nickel Chloride	$\text{NiCl}_2 \cdot 6\text{H}_2\text{O}$	45	45
			Boric Acid	$\text{H}_3\text{BO}_3$	40	40

The electrolyte temperature was maintained at 50 °C with a thermostatic bath and the NiCo deposition time was 120 minutes with a constant current density of 20 mA/cm<sup>2</sup>. Fig. 3.2 shows a schematic illustration and experimental set-up of NiCo electroplating. After the electroplating process, the sample was rinsed in distilled water and dried in saw dust before final weighing.

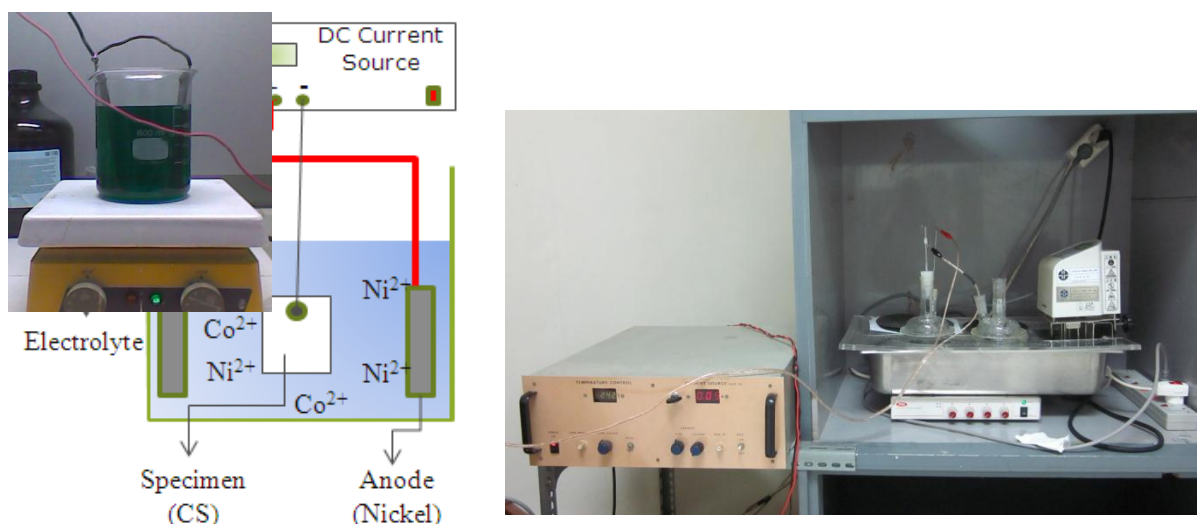


Figure 3. 2. (a) Schematic illustration, (b) Ni-strike solution, and (c) experimental set-up of NiCo watt electroplating.

After NiCo electroplating process, chromizing continued by aluminizing was carried out. For the pack mixtures, Cr and/or Al powder,  $\text{NH}_4\text{Cl}$  halide salt, and alumina powder, were used as donor, activator, and filler of the pack, respectively. The substrates were covered with the pack powder in cylindrical alumina crucibles. The formulations of the powder mixtures and the pack condition are summarized in Table 3.3. Pack cementation process was carried out under argon atmosphere in order to protect the specimens against oxidation as shown in Fig. 3.3. Finally, several types of the coated samples have been developed with two concentrations of cobalt, Ni(1 wt%)Co and Ni(5 wt%)Co, and different temperature of pack cementation process, which is 800 °C, 900 °C, and 1000 °C.

Table 3.3. Formulation of the pack mixture.

<b>Chromizing</b> Temp: 800 – 1000 °C time: 10 hours			<b>Aluminizing</b> Temp: 800 - 1000°C Time: 20 minutes		
<b>Chemical</b>	<b>Formula</b>	<b>Concentration (wt%)</b>	<b>Chemical</b>	<b>Formula</b>	<b>Concentration (wt%)</b>
Chromium	Cr	30	Aluminium	Al	25
Alumina	$\text{Al}_2\text{O}_3$	60	Alumina	$\text{Al}_2\text{O}_3$	70
Ammonium Chloride	$\text{NH}_4\text{Cl}$	10	Ammonium Chloride	$\text{NH}_4\text{Cl}$	5

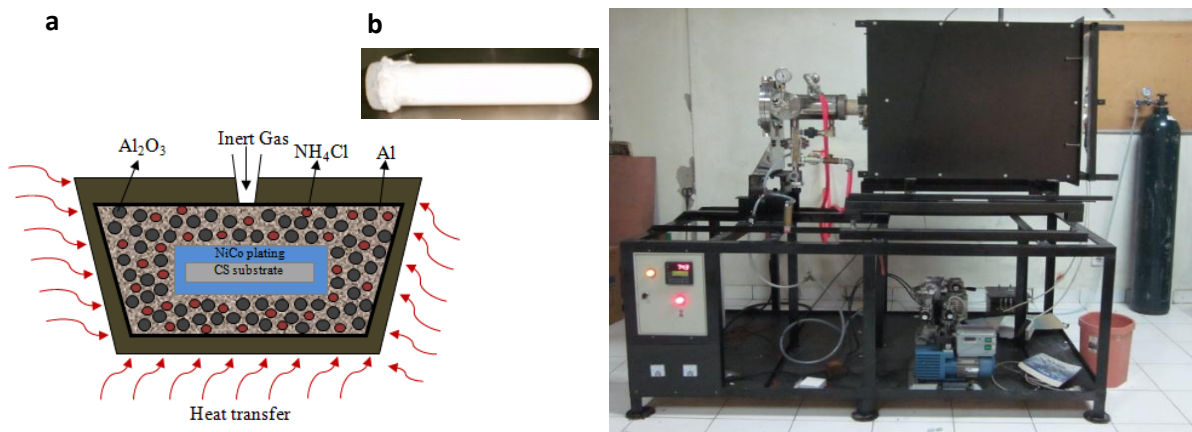


Figure 3. 3. (a) Schematic illustration, (b) sample and pack mixture in the crucible, and (c) experimental set-up for Cr and/or Al pack cementation.

### 3.1.3 Mechanical test (Hardness)

Micro hardness of the coatings was measured using a Shimatzu-HMV-2 micro hardness tester. The Vickers hardness test method consists of indenting the test material with a diamond indenter, in the form of a right pyramid with a square base and an angle of 136 degrees between opposite faces subjected to a load of 200 gf for 10 seconds. Five measurements were conducted on each sample and the results were averaged. The area of the sloping surface of the indentation is calculated (Fig. 3.4). The Vickers hardness is the quotient obtained by dividing the gf load by the square mm area of indentation with the equation:

$$HV = \frac{2F \sin \frac{136^\circ}{2}}{d^2} \propto HV = 1.854 \frac{F}{d^2} \quad (3-1)$$

Where  $F$  is load in kgf,  $d$  is arithmetic mean of the two diagonals,  $d1$  and  $d2$  in mm, HV is vicker hardness.

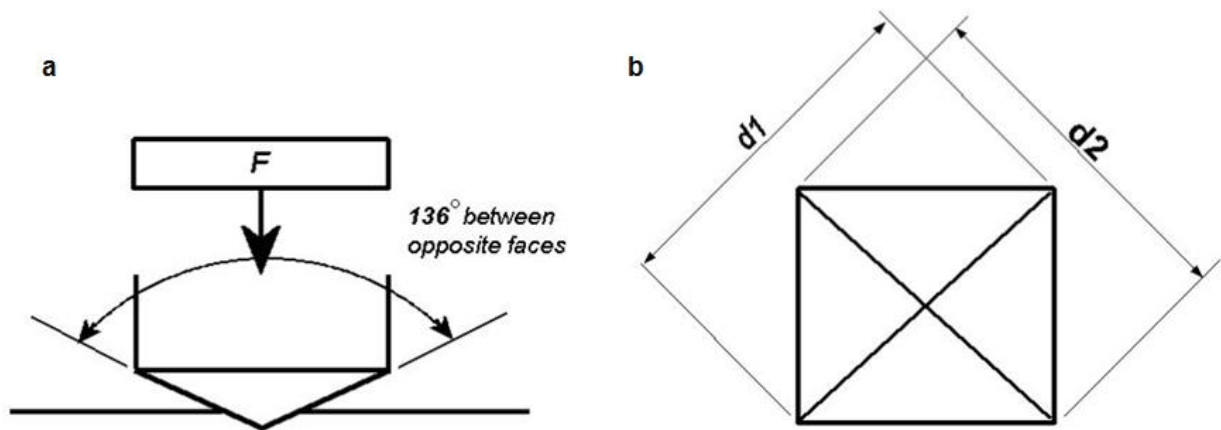


Figure 3.4. Principle of hardness test. (a) Position of indenter and (b) measuring the diameter of indentation [53].

### 3.1.4 Thermal test

#### 3.1.4.1 Isothermal oxidation

Isothermal oxidation tests of the specimens were conducted in static air in a muffle furnace for several intervals of exposure times up to 100 h as illustrated in Fig 3.5. In each interval, the specimens were kept in the furnace as temperature cooled to room temperature. An electronic balance with the sensitivity of  $10^{-5}$  g was used to measure the mass changes of the specimens.

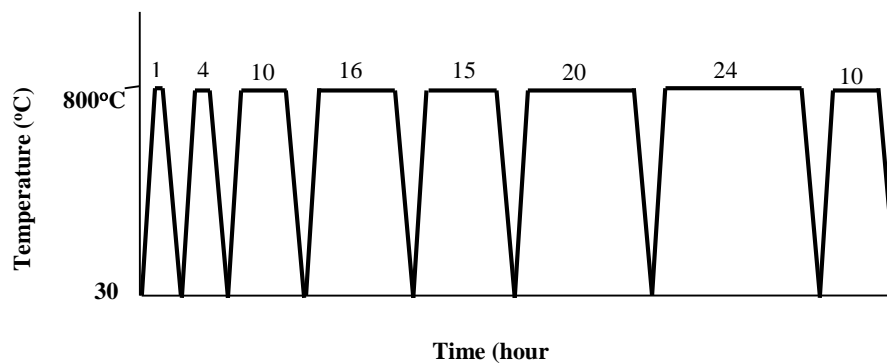


Figure 3.5. Schematic illustration of oxidation pattern.

### 3.1.4.2 Acid vapor corrosion

Acid vapor corrosion test was carried out for the piping component by using 37% HCl for 48 h. ST37 or low carbon steel and 304 type stainless steel pipes with the size of  $3\frac{1}{2}$  inch were used and the chemical composition is described in Table 3.4. The piping components consist of straight, elbow, and tee shapes. Each shape of ST37 pipe was prepared by different condition, which is uncoated, NiCo coated, NiCo coated followed by heat treatment at 800 °C for 2 h. The NiCo was electroplated by using electrolyte solution described in Table 3.2. The anode or Ni plate was adjusted inside the pipe; thus the anode was constructed as shown in Fig. 3.6. All the pipes were assembled as illustrated in Fig. 3.7(a) and then placed into the flask containing 37% HCl. The condition of acid vapor was maintained at 80 °C for 48 h by controlling the water heater. The photograph image of the arranged pipe before and after corrosion test is shown in Fig. 3.7 (b and c).

Table 3.4. Chemical composition of ST37 and 304 SS (wt%).

Mass%	C	Si	S	P	Mn	Cr	Ni	N	Fe
ST37	0.17	-	0.045	0.045	1.40	0.1	-	-	Balance
304 SS	0.08	0.75	0.003	0.045	2.0	18	8	0.1	Balance

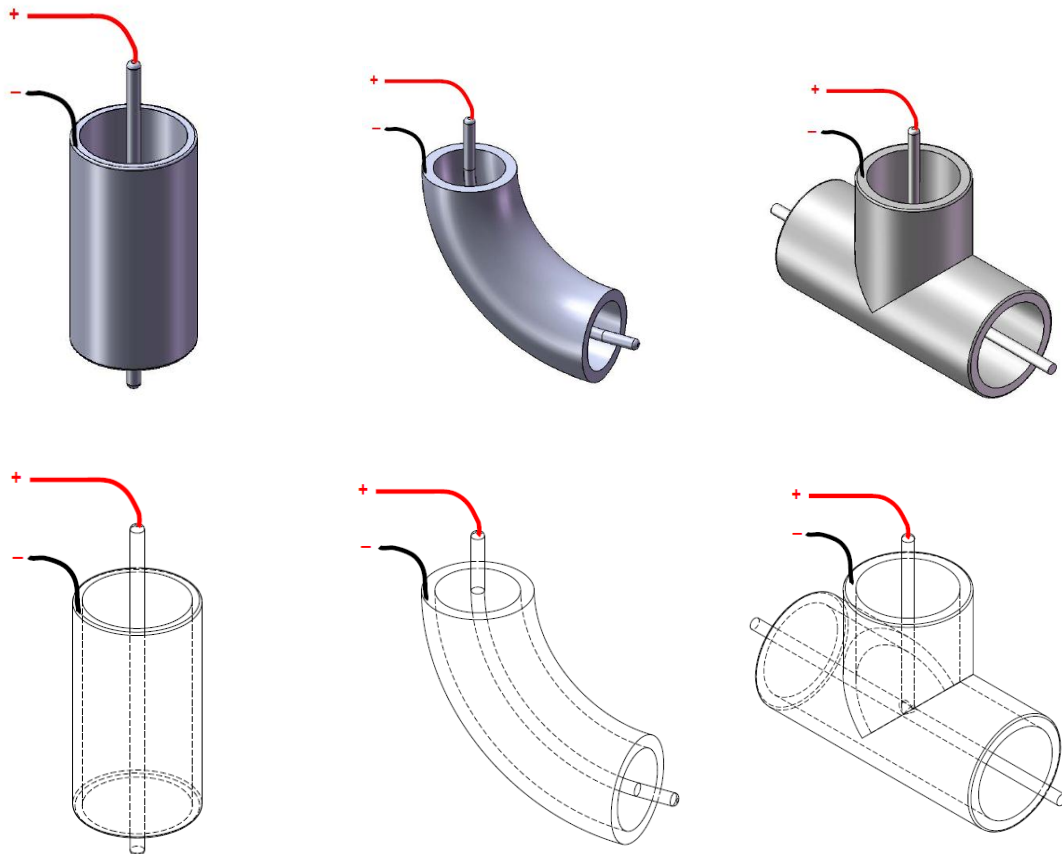


Figure 3.6. Schematic drawing the placement of Ni plate as anode was placed inside the piping components for electroplating process.

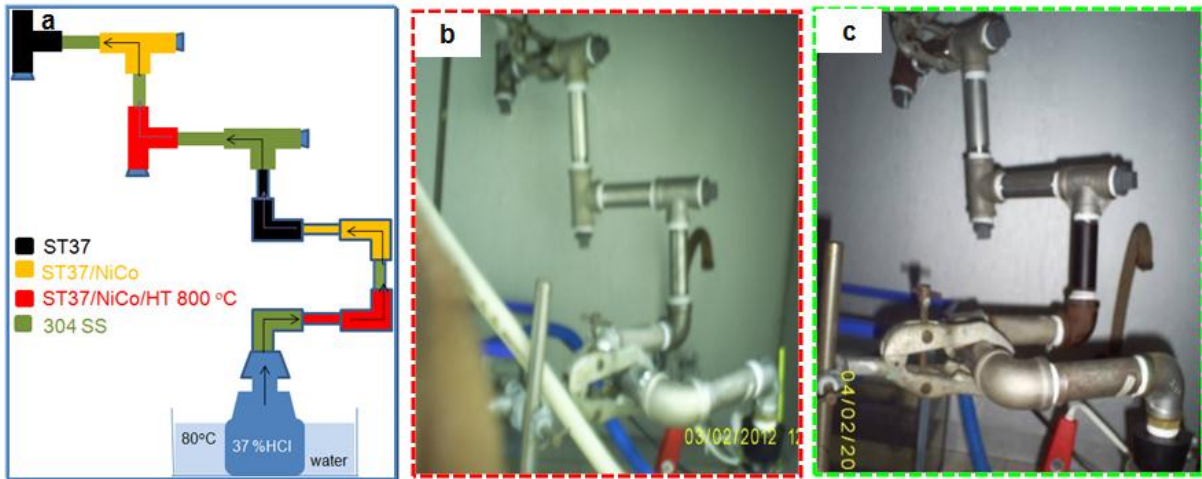


Figure 3.7. (a) Schematic illustration, photograph image (b) before, and (c) after acid vapor corrosion test by 37% HCl for 48 h.

### 3.1.5 Sample preparation for cross-sectional microstructure

#### 3.1.5.1 SEM and FE-EPMA samples

The particular choice of a sample preparation procedure depends on the alloy system and also on the focus of the examination, which could include process optimization, quality assurance, alloy design, deformation studies, failure analysis, and reverse engineering. Metallographic sample preparation comprises three or four steps: mounting (optional), sectioning, mechanical abrasion, and polishing. Listings of the equipment used on each step are detailed in Table 3.5.

Table 3.5. Equipment used for metallographic sample preparation.

mounting	sample clip, hardener and epoxy resin
sectioning	saw and cutter
polishing	emery paper (#400, 800, 1000, 1200, 1500 and 2000) alumina suspension, polishing cloth and grinder
miscellaneous	ultrasonic cleaner and dryer

### 3.1.5.2 HVEM and TEM samples

A cross-sectional TEM (XTEM) specimen, containing a multi-layer, was prepared by using two ion beam techniques depending on the characteristic of the coating specimen. An argon ion slicer (IS, JEOL EIS 9100) was first employed to obtain a large area of multi-layer coated sample. Although the IS technique has the advantageous, several difficulties still remains for preparing a XTEM of the coated layer. The sample had to be cut in an appropriate size prior to the IS, causing spallation of the oxide scale. Additionally, a focused ion beam (JEOL, JFIB 2300) technique was used to obtain XTEM specimens at the specific sites, which is not possible by the IS method. With these two techniques, it is possible to prepare XTEM specimens of as-coated and treated samples.

#### Argon Ion Slicer (IS)

As starting, a coated bulk specimen had to be cut in dimension of 2.8 x 0.1 x 0.45 mm as illustrated in Fig. 3.8. An argon flow rate of 7.3 to 7.8 (arbitrary unit) was selected to obtain a thin foil specimen with minimum damage.

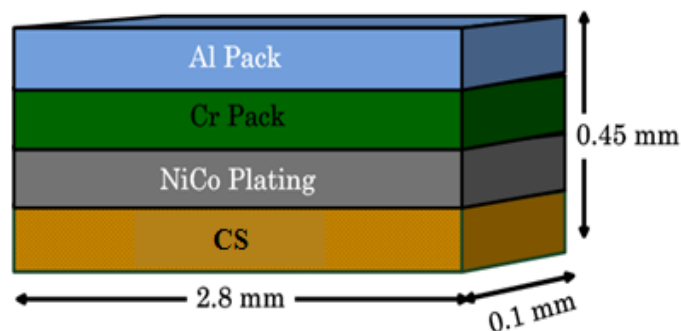


Figure 3.8. Schematic illustration of the IS specimen size.

Three times millings with angles of between 2° and 5° have been shown to be highly effective in preparing a XTEM coating specimen which comprised of materials with varying

milling rates. The process shows a good result for about 6 h milling and then a large electron transparent area with a uniform thickness was produced.

Fig. 3.9 shows the milling condition and appearances of specimen. The coating layer is mounted upward in first milling, downward in second milling and refinement in third milling. The thinned region produced in thickness about 100 nm. Like in conventionally thinned samples a small hole is generated in the thinnest region of the sample.

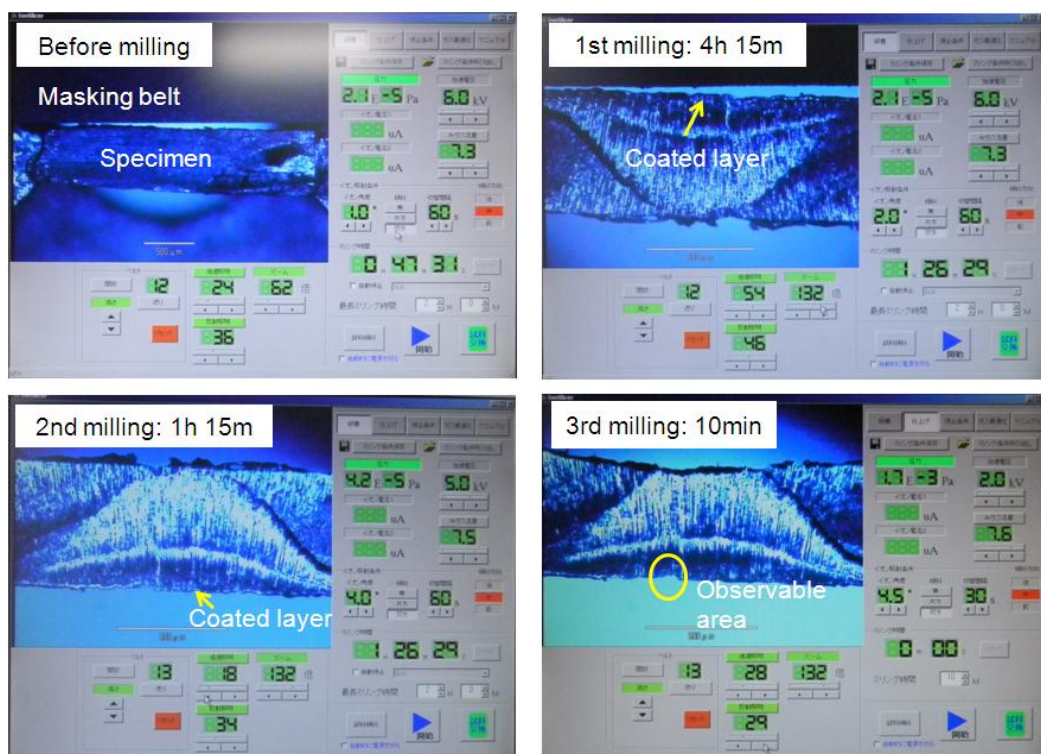


Figure 3.9. Typical thin (less than 1 $\mu$ m) “lagoon shaped” area produced by IS technique. The coated layer is indicated by the yellow arrow and an observable area is indicated by the yellow circle.

### Focused Ion Beam (FIB)

The nanometer scale resolution of the FIB allows the precise location the area of interest on the specimen; therefore the exact region for thinning can be chosen. In this research ex-situ lift out approach has been attempted.

### **Ex-situ lift out technique**

Method for ex-situ lift out technique can be simplified into following successive steps and it is shown in Fig. 3.10.

- The selected region is firstly deposited with tungsten. Then, 20 x 20  $\mu\text{m}$  excavation area was milled by high current and big aperture beam size for about 10 minutes (Fig. 3.10(a)).
- In this method, the Ga beam size is successively reduced and the sample is thinned down to below 500 nm (Fig. 3.10 (b - d)).
- Further thinning at both sides of the section is done with ion currents below 100 pA. When a thickness between 50 to 100 nm is reached the sides of the section are cut off (Fig. 3.10(e)).
- After tilting the sample to  $53^\circ$  the cut section is viewed from the side and the bottom of the section is cut (Fig. 3.10(e bottom)).
- The specimen is removed from the FIB system and placed under an optical microscope. A thin quartz needle attached to a micromanipulator is approached to the cut region. The thin section usually clings to the tip of the quartz needle due to electrostatic forces and can be removed from the specimen.
- In the next step, the quartz needle is approached to a Cu grid with an amorphous carbon film. When the quartz needle is touching the carbon film the thin sample section sticks typically easily to the carbon film.

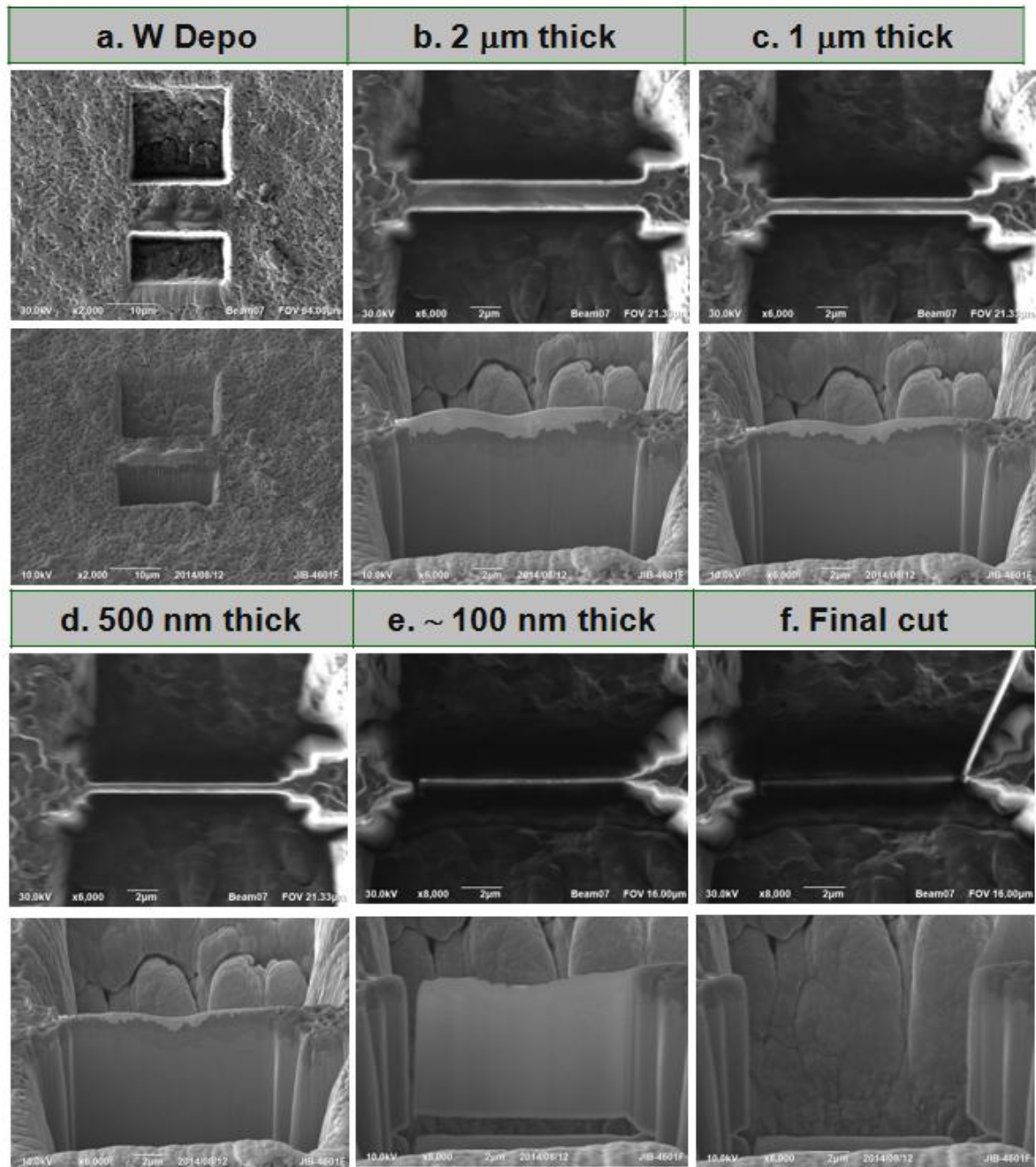


Figure 3.10. Different steps of ex-situ lift out process. (Top) plain view and (bottom) cross cut view.

## 3.2 Experimental techniques and instrumentation

### 3.2.1 Multi Beam High Voltage Electron Microscopy (HVEM)

A multi beam high voltage TEM (JEOL – JEM ARM 1300) was used to obtain the

nano-structure of the coated sample in the present study. HV-TEM is used for a wide range of application involving research and development of aerospace material, atomistic direct observation, synthesis modification for developing non equilibrium material and etc. The accelerating voltage is work in the range of 1 to 1.3 MV, the highest point resolution of 0.12 nm, atomic resolution (1.17 Å) and high tilting ( $\pm 45^\circ$ ) as well as energy filtering which makes it capable to characterize the electron crystallography of nano-sized functional materials. The various advantages of this facility are high resolution, high specimen penetration, and high depth of information as well as low beam damage.

### **3.2.2 Transmission Electron Microscopy (TEM)**

TEM is an analytical method which allows detailed examination of microstructure, crystal structures, chemical compositions and orientation of precipitates, through high-resolution imaging, diffraction pattern, and X-ray analysis.

The acceleration voltage of the latest TEM is between 100 to 200 kV which defines the velocity and wavelength, and hence the resolution of the microscope. The image can be recorded with a CCD camera linked to a computer or by developing a film.

The objective lens provides the formation of either the image or the diffraction pattern of the specimen [55]. Imaging mode uses the differences between intensities of the electrons after they have interacted with the sample. The contrast images are formed by means of an aperture. A bright field image is created by the transmitted beam and a dark field image by one of the diffracted beams which have travelled through the specimen and the microscope column. Interactions of charged electrons with the periodic crystal lattice are necessary to obtain a diffraction pattern. This provides information on the atomic positions. TEMs can produce different types of electron diffraction patterns: spot patterns, ring patterns, Kikuchi patterns, Selected Area Diffraction (SAD) Pattern, Convergent-Beam Electron Diffraction (CBED)

Pattern.

X-rays generated through the interaction of the electron beam with the specimen can be used to determine the composition and identities of phases from their EDX spectra. In this study, the JEOL 2010 transmission electron microscope was used for micro-structure analysis.

### **3.2.2.1 Energy Dispersive X-ray Spectroscopy (EDS)**

Contemporary electron microscopes are regularly equipped with an energy dispersive X-ray (EDX) detector which enables both quantitative and qualitative analysis of the specimen to be obtained.

An EDX system consists of a sensitive X-ray detector, a liquid nitrogen vessel for cooling, and software to collect and analyze energy spectra [51]. The detector is held in the sample chamber as close to the specimen as possible to collect the maximum possible energy of incoming X-rays by ionization. The X-ray entering the detector is converted into an electrical signal of proportional size; the resulting electrical pulses are amplified, registered and can be presented as energy spectra. Every element is represented by characteristic X-ray spectrum. The detector is made of semiconducting silicon or germanium crystals that operate at low voltages to improve sensitivity. EDX system software analyzes the energy spectrum in order to determine the abundance of specific elements, and can create an element composition map showing the spatial distribution of elements in the sample.

### **3.2.2.2 Selected Area Electron Diffraction (SAED)**

The diffraction pattern contains electrons from the whole area of the specimen that is illuminated. Such a pattern is not very useful because the specimen will often be buckled. Furthermore, the direct beam is often so intense that it will damage the viewing screen. Insertion of an aperture in the image plane of the microscope results in the blocking of those

electrons which fall outside the dimensions of the aperture. SAED is a useful tool to acquire electron diffraction patterns from a certain area of interest on the specimen.

### **3.2.3 Ion beam milling techniques**

Specimen preparation is an important aspect of the TEM analysis of high temperature coating materials. The recent trend in coating material is to elucidate the structural understanding of the coating formation and evolution at the microscopic scale. The research detailed herein exemplifies the effort that is being expended to enhance both specimen preparation procedures and TEM performance.

Specimen preparation techniques are very material dependent, therefore, it is important to initially select the technique that is most beneficial for the individual specimen. For most coating materials, a suitable preparation technique is argon ion slicer (IS) and focused ion beam (FIB) [56-57].

#### **3.2.3.1 Argon Ion Slicer (IS)**

Argon Ion slicing (IS) milling has recently evolved into one of the most effective techniques for preparing specimens for the TEM. An IS based on a shadowing technique and leads to high quality, homogenous, damage free and large electron transparent areas. The sample should be prepared in appropriate size to  $100(\pm 10)$   $\mu\text{m}$  thick prior to the ion milling. The sharp edge of the sample is partially shaded by the sharp edge of a copper mask belt with a thickness of 10  $\mu\text{m}$  mounted above the sample. The ion beam lies in the same plane as the sharp edges of sample.

In this respect the tilt angle determines the final size of the thinned area obtained. The beam can be tilted in various angles from  $0^\circ$  to  $6.0^\circ$ . The slicing process alternates between front and backside whereas side change intervals are variable as are accelerating voltage and

slicing time. Streaks produced during slicing on the sample surface are minimized by a “swing-mechanism” rocking the sample stage slightly in the plane of the ion beam (Fig. 3.11). In this study, an argon ion slicer (JEOL – EM09100IS) was used for XTEM specimen preparation.

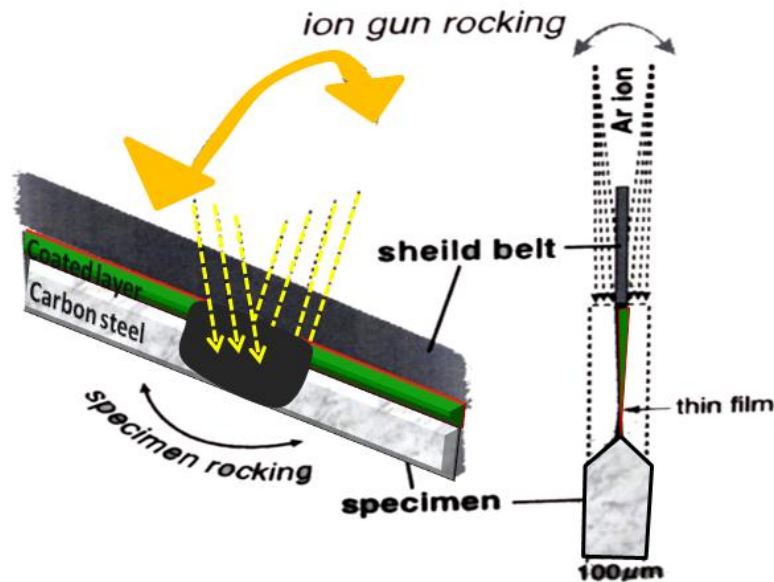


Figure 3.11. Schematic illustration of argon ion beam irradiation to a specimen. (Left) Argon ion source and the specimen holder rock  $\pm 6.0^\circ$ . (Right) A side view of the specimen blocks [56].

### 3.2.3.2. Focused Ion Beam (FIB)

The FIB technique is used particularly for site - specific analysis, deposition, and ablation of materials [58]. Nowadays, most instruments combine a SEM (electron) and FIB (ion) column, which allows imaging at higher magnifications and more accurate control during the milling process as shown in Fig. 3.12. Liquid gallium is predominantly used as a source of ions ( $Ga^+$ ), which are then accelerated to energy of 5-50 keV, and focused onto the sample. Some sputtered atoms and molecules as well as secondary electrons and ions are generated out from the specimen surface after the collision. Optimization of beam currents provides either high imaging resolution or higher amount of material being removed (down to a sub-micron

scale). In this study, a focus ion beam (JIB 4600F/HKD) was also used for XTEM specimen preparation.

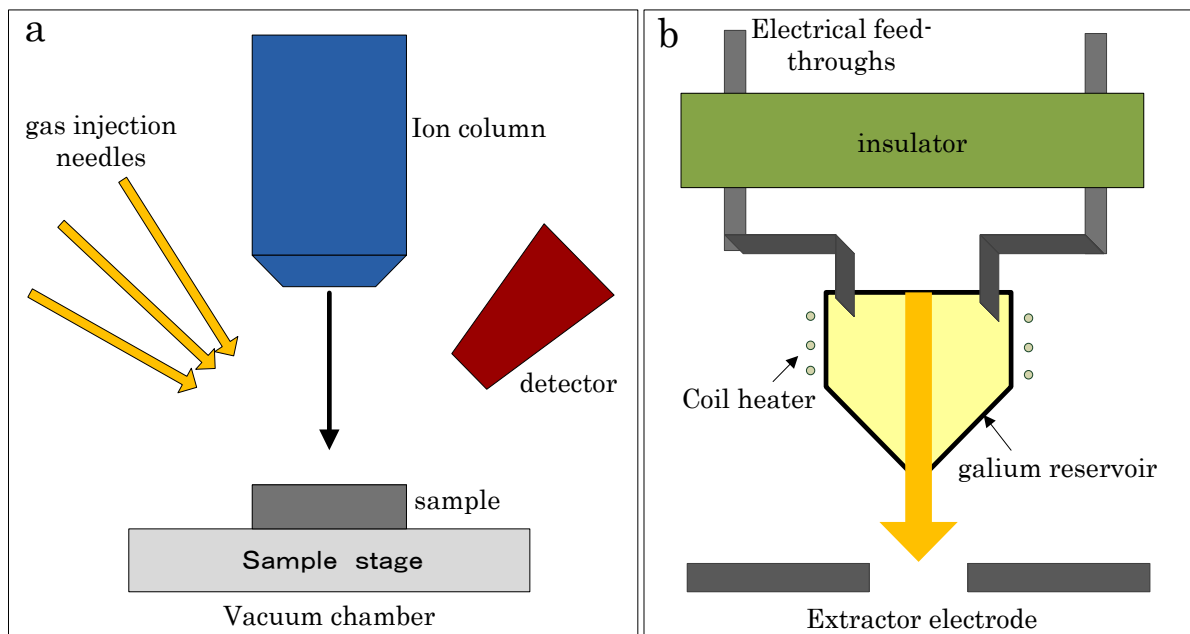


Figure 3.12. Schematic diagrams of (a) a basic FIB system and (b) liquid metal ion source [58].

### 3.2.4 X-Ray Diffraction (XRD)

A Philips X-ray diffractometer (PANalytical X-ray Instruments) combined with an X'Pert Pro software, PW3040/60 X-ray generator and fitted with an X'Celerator detector was utilized. Diffraction data is acquired by exposing the samples to Cu-K $\alpha$  X-ray radiation, which has a characteristic wavelength ( $\lambda$ ) of 1.5418 Å. X-ray was generated from a Cu anode supplied with 40 kV and a current of 40 mA.  $2\theta$  diffraction angles of 10°- 90° with step sizes of 0.01° and step times of 50 seconds were used for determining phases present in the coatings. Fixed anti-scatter and divergence slits of 5 mm were used together with a beam mask of 10 mm and all scans were carried out in 'continuous' mode.

Phase identification was carried out by means of the X'Pert accompanying software program PANalytical High Score Plus in conjunction with the ICDD Powder Diffraction File 2 Database (1999) [59]. In the case of the as-coated and oxidized samples, the XRD analysis was performed on the top surface of the samples.

### **3.2.5 Scanning Electron Microscopy (SEM)**

A 20 kV SEM (JEOL, JSM6380LA) permits the acquisition of three-dimensional-like images and the determination of many properties of the sample (composition, surface topography, etc.) [60]. The interaction of the electron beam with the sample produces different types of signals, *e.g.* secondary electrons, backscattered electrons, characteristic X-rays, and other photons of various energies. Secondary electron imaging (SEI) was mainly used for analyzing the coating morphologies. Backscattered electron imaging (BSE) was carried out for the analysis of different phases available in the coatings. Since the BSE imaging mode relies on the differences in the mean atomic number of the existing phases. This results in the phases with higher mean atomic number to appear brighter than the phases with a lower mean atomic number.

In addition, contemporary electron microscopes are equipped with an Energy Dispersive X-ray (EDX) detector which allows for both quantitative and qualitative analysis of the coated sample. Details are given in section 3.2.2.1

### **3.2.6 Field Emission - Electron Probe Micro Analyzer (FE-EPMA)**

A FE-EPMA (JEOL, JXA-8530F) is the only physical analysis device with an established quantitative correction method. It is possible to perform elemental analysis of 100 nm micro regions, which is not possible with conventional EPMA [61]. This technique is

commonly used with a probe current of 10 nA to 100 nA. The FE-EPMA can analyze almost all elements at accelerating voltages down to 6 kV, when the characteristic X-ray excitation voltage of all X-ray lines is considered. Therefore, an EPMA with FE gun, capable of achieving the finer probe at lower accelerating voltages and high probe currents needed for analysis, then can improve the micro area analysis capability over the conventional EPMA. FE-EPMA in the present study is used to obtain X-ray maps which enabling a quantitative understanding of the behavior of each element diffused toward the coated sample.

### **3.2.7 Non-destructive technique for material characterization**

Non-destructive technique (NDT) is widespread use in industrial R&D as well as in research laboratories. The most widely used NDT is ultrasonic inspection, acoustic emission, vibration diagnostics, eddy current inspection, X-ray radiography, and leak detection. Neutron radiography (NR), an advanced technique for non-destructive materials testing, utilizes transmission of radiation to obtain visual information on the structure and/or inner processes of a given object. Over the last two decades there has been considerable development of NR techniques, and these techniques have found more and more applications. Moreover, the demand for high level technology in materials research and in industry increasing interest in the intermediate future.

NR has a special role because of the need for high intensity neutron sources. These sources are generally provided by a research reactor or in special applications, portable sources ( $^{252}\text{Cf}$ -isotope or accelerator based neutron source) [62]. NR extends the ability to image the internal structure of a sample beyond what can be accomplished with photon (X-ray and Gamma) radiation. The similarities of neutron and photon radiography include the ability to produce a visual record of changes in density, thickness and composition of a specimen.

Over the last decades there has been a considerable development of NR and such

techniques are increasingly used because of the demand for high level technology in materials research and in industry. NR is employed in a wide range of investigations, including:

- Routine test measurements in quality control, e.g. nuclear fuel rods, pyrotechnical materials, turbine blades, corrosion of aircraft, inspection of honeycomb structure in rotor blades.
- Materials science and R&D of industrial products, e.g. environmentally materials (Freon-R134a), heat tubes, oil flow in gas turbine engines and components, refrigerator and compressor system.
- Hydrogen diffusion in metals, oil infiltration in petro-physical model systems, thermodynamic properties of two-phase systems
- Investigation of works of art (paintings and ancient sculptures).
- Biological and plant physiological research, e.g. root growth, distribution of water and heavy metals in plants.

The basic principle underlying in this technique is due to the penetrating nature of neutron radiation and its differential absorption by the material to obtain details of the internal structure. The absorption depends on the atomic number, thickness of the materials, homogeneity and composition. The geometric pattern of the transmitted neutron intensity is recorded using a suitable detector and visualized as described in Fig. 3.13.

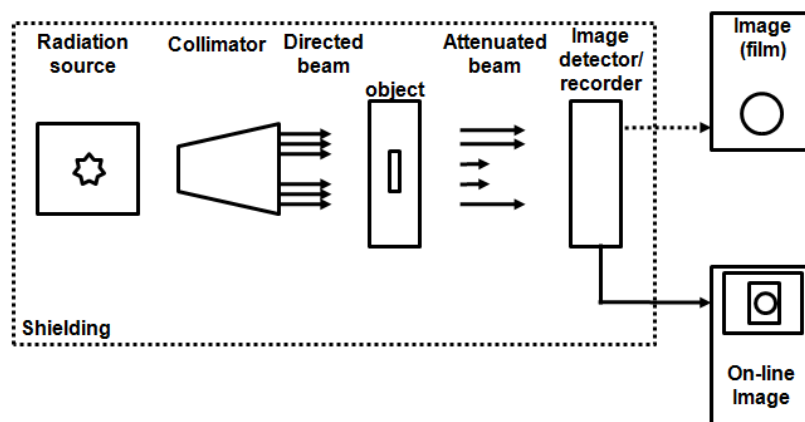


Figure 3.13. Schematic illustration for capturing an image by neutron radiography [63].

- **Collimator**

A useful beam of neutrons is required for NR. The extraction of the neutron beam from the reactor core is achieved through the insertion of probe (beam) tube or collimator. This permits only those neutrons having a direction to that of the tube axis to pass through. The divergent type collimator is widely used since a uniform beam can be projected over a large inspection area. The object under examination is placed in the path of the incident radiation and the transmitted radiation is detected by a two-dimensional imaging system as illustrated in Fig. 3.14.

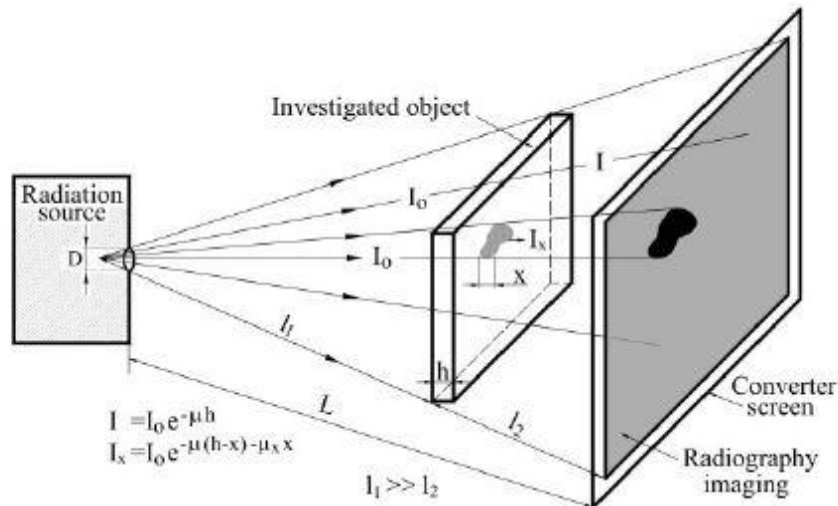


Figure 3.14. NR arrangements for the collimation ratio, the neutron flux and the transmitted intensity of the radiation measurements [64-65].

The important geometric factors for neutron collimator are the total length ( $L$ ) from inlet aperture to detector and effective dimensions of the inlet collimator ( $D$ ). This is usually expressed as collimation ratio  $L/D$ . This important parameter describes the beam collimation and will limit the obtainable spatial resolution by the inherent blurring independently from the properties of the imaging system. This un-sharpness  $U_{beam}$  can be related to the distance between the object and the detector plane  $l_2$  and to the  $L/D$  ratio [65]:

$$U_{beam} = \frac{I_s}{L/D} \quad (3-2)$$

Two opposing demands have to be taken into consideration when planning a radiography arrangement. If  $L/D$  is large then the neutron flux  $\Phi_{NR}$  at the imaging plane is relatively weak but the geometrical sharpness is high. The basic relation for  $\Phi_{NR}$  is [65]:

$$\Phi_{NR} = \frac{\Phi_s}{16 (L/D)^2} \quad (3-3)$$

where  $\Phi_s$  is the incident neutron flux.

In radiography imaging the attenuation coefficient  $\mu$  is a crucial parameter. The transmitted intensity of the radiation,  $I$ , passing through a sample with an average transmission of  $\mu$  can be written as [65]:

$$I = I_0 e^{-\mu h} \quad (3-4)$$

Where  $I_0$  is the incident intensity and  $h$  is the thickness of the sample. If there is any inclusion (in homogeneity, inner structure) in the sample of thickness  $x$  and transmission  $\mu_x$  then the transmitted intensity,  $I_x$  is given as [65]:

$$I_x = I_0 e^{-\mu(h-x) - \mu_x x} \quad (3-5)$$

If the value of  $\mu$  and  $\mu_x$  are different from each other the presence of the inclusion will provide a contrast in the radiography image.

- ***Neutron detection***

Neutron is not directly ionized radiation and hence has no effect on the conventional films used in industrial radiography. Hence, the detection system for neutron consists of a latent image recorded in close contact with a thin sheet of material (referred to as converter screen), which absorb the neutrons and converts them into a form of secondary radiation to which the image recorder responds. The converter screen is often metallic foils. The emission from the foils can be either charged particles or electromagnetic radiation, which produced the image on the film/screen. The technique used for imaging can be classified as direct and indirect.

- a. *Direct technique*

A foil of gadolinium is used before the film (Fig. 3.15). Gadolinium atoms in the foil absorb a neutron and promptly emit other radiation such as electron. Alternatively, a scintillator screen containing a mixture of lithium-6 and zinc sulphide can be utilized. On observing a neutron, a lithium atom emits an alpha particle and this then strikes the zinc sulphide screen, which in turn emits a light photon. As the above processes are continuous reactions, this type of foil and scintillator screen can be used with low neutron fluxes and long integrating exposures. Also, as the film is in contact with the converter during the neutron exposure the entire forward emitted radiations takes part in the exposure of the film. Thus, the direct technique is fast, the scintillator screen being 30 to 100 times faster than metal foils.

- b. *Indirect technique*

This is also referred to as transfer technique. This method relies on the build-up of radioactivity in the foil produced by neutron absorption. In this way an activation image is formed in the foil and this is subsequently transferred to a photographic film in contact and

allowing the decay radiations from the foil to produce the latent image on the film (Fig. 3.15). This method is useful for nuclear applications since the process of activation and film exposure are two independent processes. However, the technique is much slower compared to direct one.

The attenuation coefficient ( $\mu$ ) vs. atomic number of the elements for thermal neutron, X-ray and gamma is shown in Fig.3.16. Its value depends on both the coherent and incoherent scattering and on the absorption properties of the elements(s). For neutron,  $\mu$  does not show any regularity as a function of atomic number, and for some of the lightest elements (H, B, Li) the attenuation coefficient is by two order of magnitude greater than the corresponding parameter for most of the technically important elements, such as Al, Si, Mg, Fe, Cr.

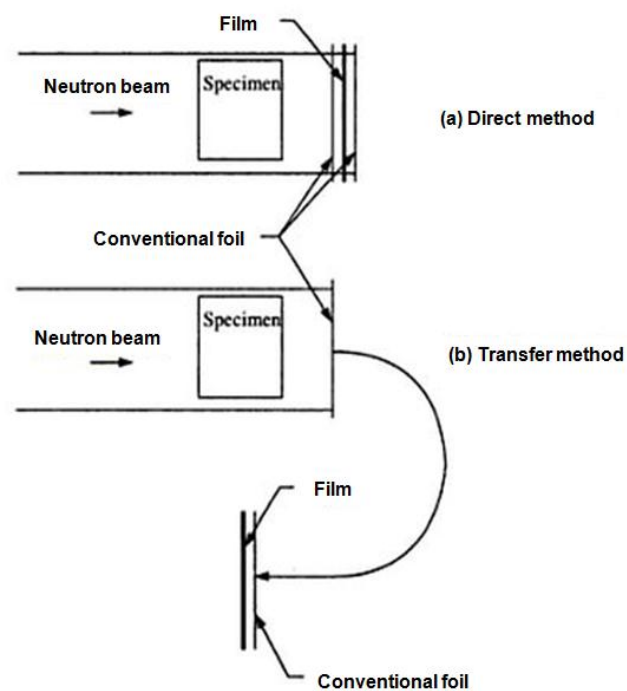


Figure 3.15. Detection techniques for neutrons [63].

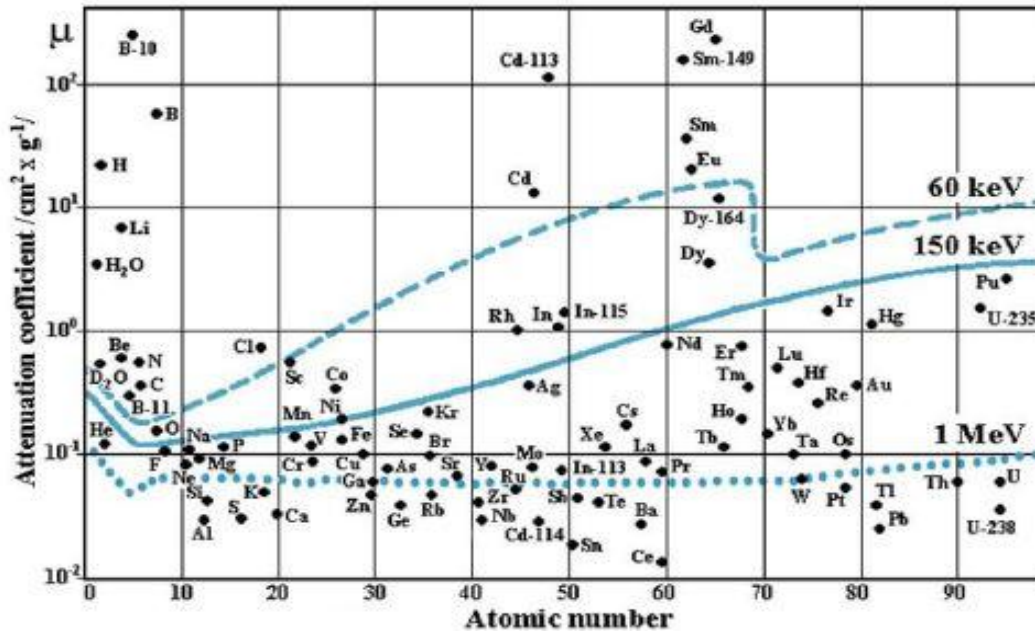


Figure 3.16. The logarithmic scale of attenuation coefficient of elements for neutrons (separate dots), for 1 MeV gamma-ray (dotted line), for 150 keV X-ray (solid line) and for 60 keV X-ray (dashed line) [63].

The differences in absorption coefficients between neutron and X-rays suggest a number of possible applications for NR, such as:

- a. Examination of dense materials like uranium, lead, etc.
- b. Detection of light materials enveloped in denser materials.
- c. Differentiating between isotope of same elements and
- d. Examination of radioactive material due to availability of image detection methods, which are not sensitive to the associated gamma rays.

### 3.2.7.1 Neutron Radiography (NR) Facility at BATAN, Indonesia

A neutron radiography facility located at National Nuclear Energy Agency of Indonesia (BATAN) start to be implemented in 1992. The NR had been installed at the S2 tangential beam port of the G. A. Siwabessy multi-purpose reactor (RSG-GAS) [66-67], as shown in Fig.

3.17. This facility consists of an inner collimator inside the RSG-GAS reactor wall, a 30 cm-diameter outer collimator, and two shutters, i.e. a main shutter driven by an electric motor, and an auxiliary shutter driven by a hydraulic pump. A movable sample table is located in front of a Li<sub>6</sub>-ZnS scintillation screen which visualizes the radiograph of the sample. In order to prevent damages by the neutron radiation to an ultra-light sensitive CCD camera, a TiO<sub>2</sub> mirror with a 95% reflectivity is used to reflect the radiograph to the camera. Since light intensity of the radiography image emitted by the scintillation screen is very low, the scintillation screen, the mirror and the CCD camera are located inside the dark box, as shown in Fig. 3.17. Then, the radiography image captured by the camera is further processed by a computer outside the radiography room.

Table 3.6 shows the instrumental parameters of the neutron radiography facility. The radiography technique using Gd and X-ray film was still used to observe the material. A standard sample from American Society for Testing and Materials (ASTM) is also still used.

Table 3.6 Instrumental parameters of neutron radiography facility at BATAN, Indonesia.

Neutron source	: GAS reactor beam port S-2
Neutron flux at sample position	: $10^6$ to $10^7$ n/cm <sup>2</sup> sec
Beam size at sample position	: 30 cm diameter
Collimator <i>L/D</i> ratio	: 83
Cadmium ratio	: 6.4
Neutron/Gamma ratio	: >105 n/cm <sup>2</sup> /mR
Radiography techniques	: Gd and X-ray film converter, Li <sub>6</sub> -ZnS scintillate screen, Intensified CCD (ICCD) based imaging system[65]

Based on the radiography image of ASTM E-545 standard sample, the collimation system provides neutrons with the following composition and characteristics: the fraction of thermal neutrons: 60.95%, scattered neutrons: 0.78%, gamma: 0.48%, pair production: 2.85%,

and the number of lines that could be seen: 4. From the measurement of the beam quality, the neutron radiography facility at BATAN Serpong was in the category of class III [66]. Although the facility is in the middle class of the category, many objects can be observed using this neutron radiography (NR) facility.

### 3.2.7.2 Computed Tomography (CT)

A computed tomography (CT) offers the unique capability of displaying cross sectional slices of the samples with high resolution and produces data which are easily adaptable for 3D representation. CT technique at BATAN was additional implemented with NR in 1998 by the development of data acquisition and control software for NRT as shown in Fig. 3.18 [66]. Recently, commercial neutron computed tomography software, Octopus 8.5, was used and reconstructed data was then displayed as 3D image using VG Studio 2.1. Each pixel of the CCD camera acts as an equivalent neutron detector, as it visualizes only a very narrow area of the scintillating screen. If one rotates the sample, the NR images are recorded in several positions and the use of suitable software enables the 3D image of the object to be reconstructed.



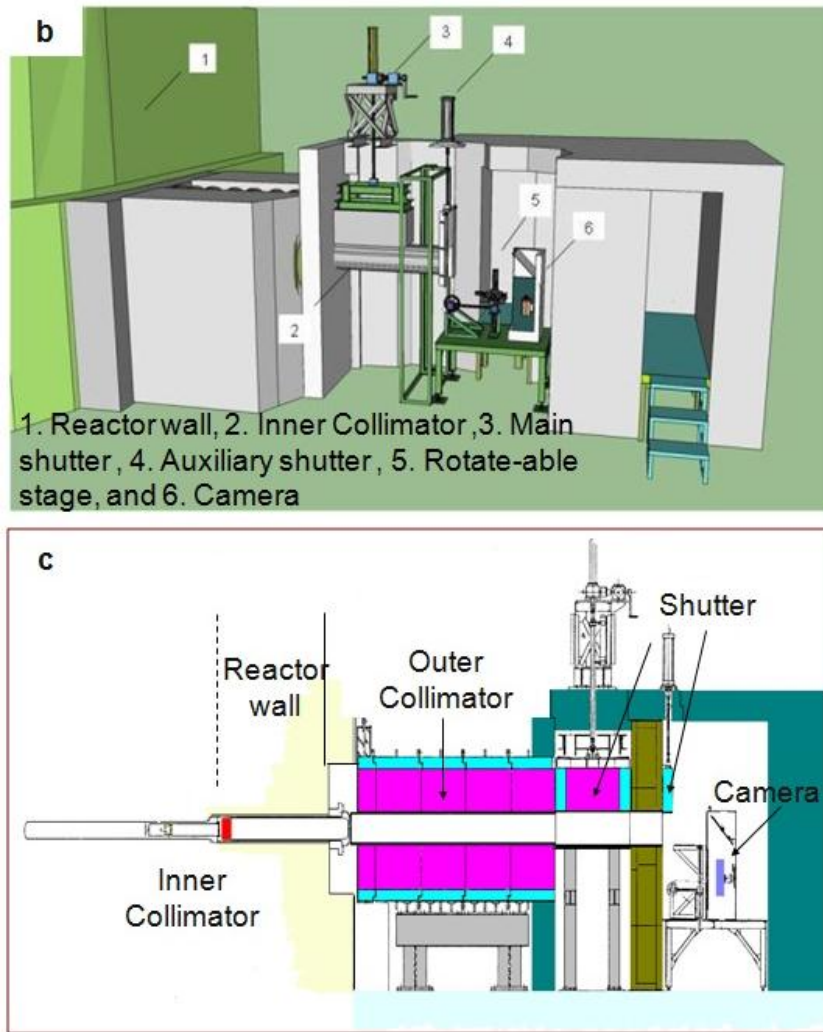


Figure 3.17. The NR facility at BATAN–Serpong. (a) the photograph of neutron radiography facility, (b) 3D, and (c) 2D of the schematic drawing of neutron radiography facility [66-67].

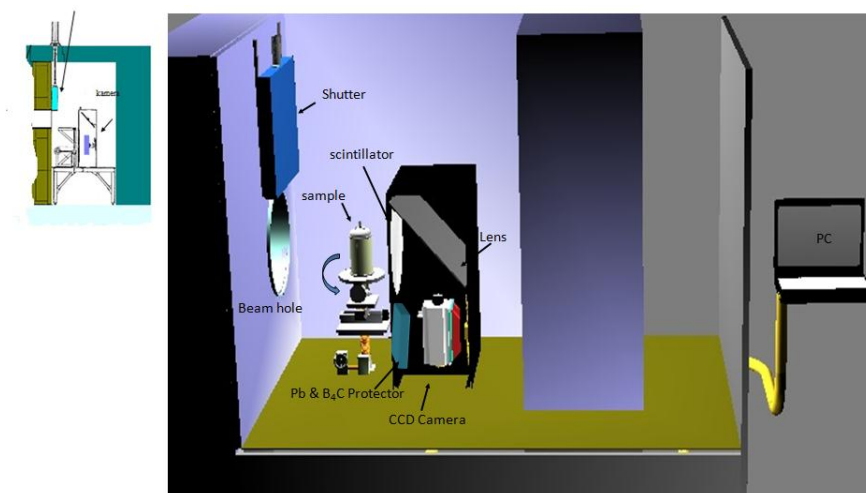


Figure 3.18. Schematic illustration showing equipment part for capturing the 2D and 3D NRT [66].

## **Chapter 4**

### **Characterization of Ni-Based Coated Layer**

This chapter focuses on a detailed characterization in micro – nano scale of coated carbon steel. At present the deposition of Ni-based coatings on carbon steel is still limited and there are no studies of NiCoCrAl coatings deposited by electroplating and pack cementation processes where the microstructure, oxidation resistance at high temperature, and hardness properties were systematically examined. The effect of the Co concentration and temperature on the oxidation and hardness properties of the carbon steel is studied. An analysis of the correlations between the structure, hardness properties, oxidation behaviors, and phase formation is also discussed. Furthermore, a comparison is made to observe the structural differences and determine the resistance of coatings in high temperature, extreme environments by subjecting all the coatings to testing in similar environments.

#### **8.3 Effect of Co content on the hardness and structural properties**

It is understood that the hardness, surface morphology, and high temperature oxidation may be influenced by the Co content in the NiCo electrodeposited on the substrate [68]. In the present study, 1 wt.%Co (sample 1) and 5 wt.% Co (sample 2) were used for the NiCo coating on the substrate. To understand the effect of the Co content on the hardness properties of the coating, hardness measurements of the carbon steel substrate without coating were also performed. Fig. 4.1 shows the micro-hardness of the substrate Fe, samples #1 and #2. The results show that the increase of the Co content from 1 wt.% to 5 wt.% in the NiCoCrAl coating increases the hardness value from 810 HVN to 1027 HVN, showing that the hardness values of the coated samples are seven and nine times higher than those of the uncoated substrate.

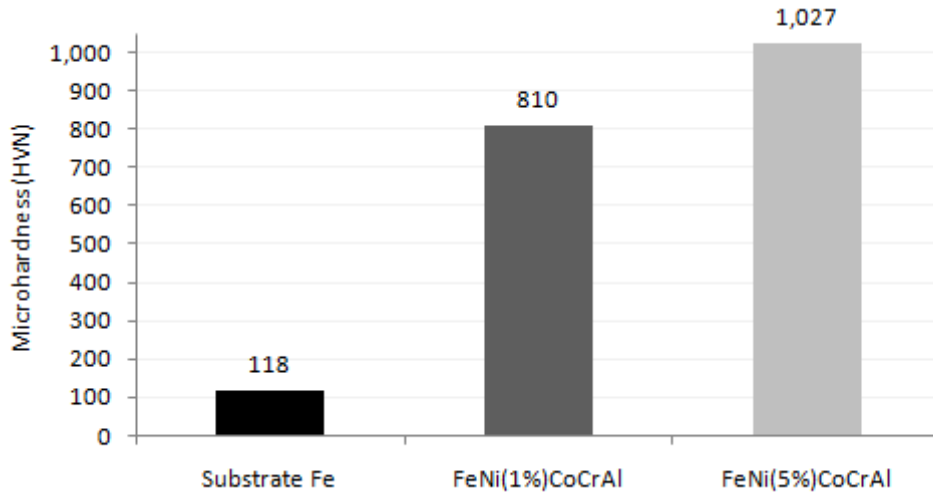


Figure 4.1. Micro-hardness measurements of uncoated and coated samples.

The surface morphologies of the as-coated NiCoCrAl coating was examined using SEM and the results are shown in Fig.4.2. It shows a regularly branched structure with average size of  $\pm 2.5 \mu\text{m}$  and  $\pm 3.5 \mu\text{m}$  for sample #1 and sample #2, respectively. The morphology is related to the structure of the hexagonal closed packed (hcp) crystals [69]. The branched structure is clustered on the surface of sample #1 and distributed throughout the coating in sample #2.

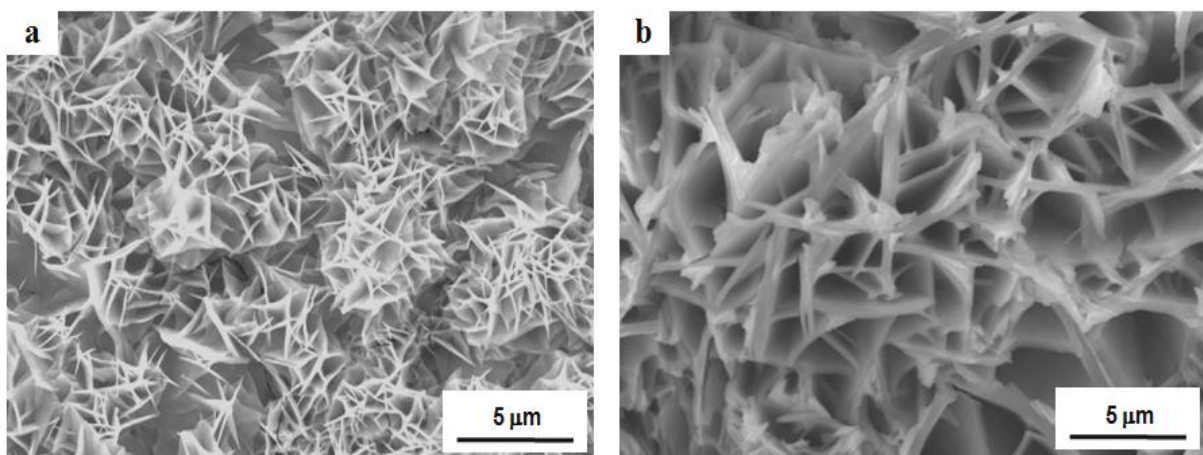


Figure 4.2. Surface morphologies of NiCoCrAl coating on carbon steel substrate with different Co contents: (a) 1 wt.% and (b) 5 wt.%.

#### 8.4 Effect of Co content on the microstructure

The cross-sectional structures of the as-coated specimens of samples #1 and #2 are shown in Fig.4.3 and Fig. 4.4, respectively. The SEM images show that the coated samples developed at 800 °C are similar with homogeneous layers and display a similar microstructure. The coatings are composed of three-layers: the first (innermost) layer of Ni(Co) symbolized by ①, the second (mid) layer of Ni(Al) symbolized by ②, and the third (top) layer of Al(Cr, Ni) symbolized by ③, with the total coating thickness about 95 μm and 160 μm for samples #1 and #2, respectively. The EDS analysis in Fig.4.3 (right) for sample #1 indicates that the Ni(Co) layer contains (96-89 at.%)Ni and (2-1.5 at.%)Co, the Ni(Al) layer contains (47-38 at.%)Ni and (57-50 at.%)Al, and the Al(Cr,Ni) layer contains (73-66 at.%)Al, (16-7 at.%)Cr, and (26-9 at.%)Ni. For sample #2, the EDS analysis in Fig.4.4 (right) indicates that the Ni(Co) layer contains (90-86 at.%)Ni and (10-8 at.%)Co, the Ni(Al) layer contains (52-42 at.%)Ni and (49-43 at.%)Al, and the Al(Cr,Ni) layer contains (66-64 at.%)Al, (20-18 at.%)Cr, and (11-13 at.%)Ni. The results show that the two coatings (sample #1 and sample #2) have different Co compositions in the inner layer ① and that there are many voids at the interface between layers ② and ③. There were also many voids at interface between layers ① and ② of the sample in Fig.4.4 (sample #2). Dark gray particles distribute in the diffusion zone between layers ② and ③ and possibly because of outward diffusion of Ni and Cr to the outermost layer and inward diffusion of Al to layer ②.

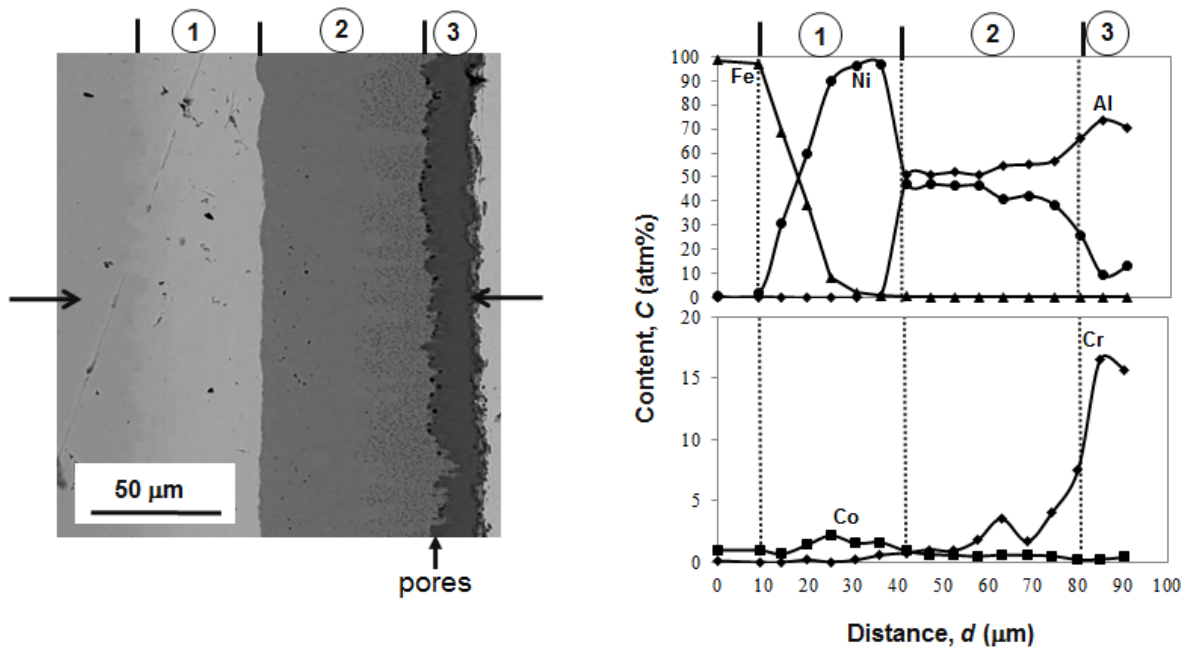


Figure 4.3. Cross-sectional microstructure and composition gradients of Ni(1%)Co plating, followed by Cr-Al pack diffusion coating at 800 °C.

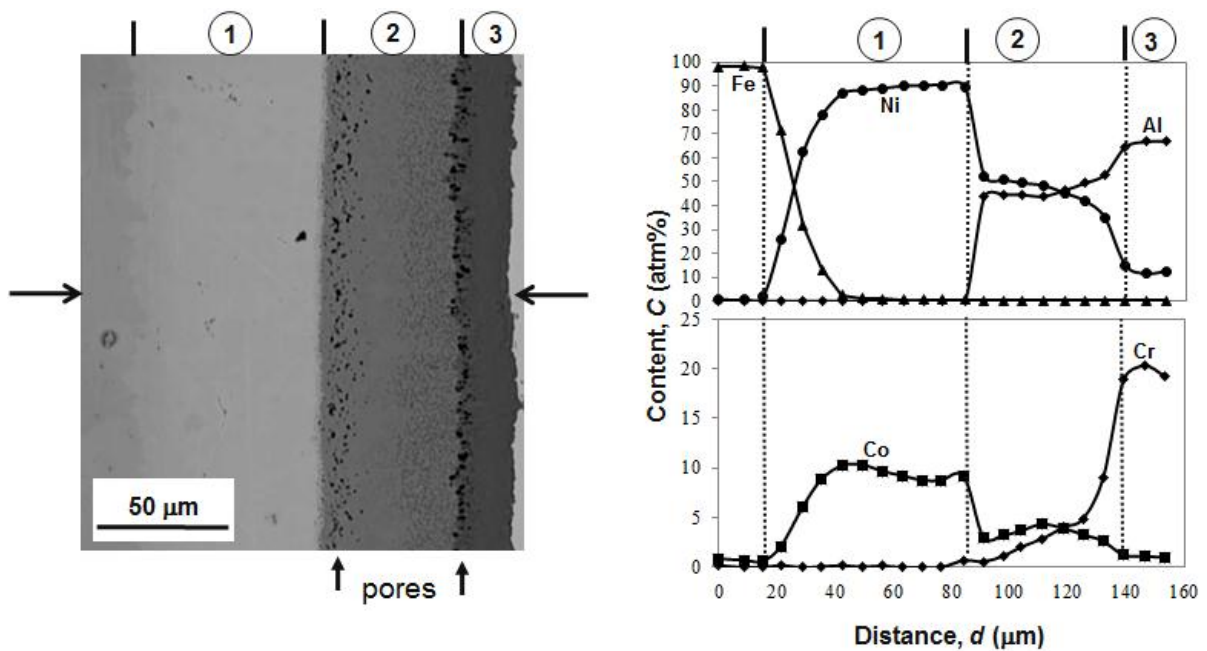


Figure 4.4. Cross-sectional microstructure and composition gradients of Ni(5%)Co plating, followed by Cr-Al pack diffusion coating at 800 °C.

Based on the micro-hardness results, a further coating, sample #3, was also prepared with 5 wt.% Co content and subjected to a higher temperature at the coating (1000 °C). The cross-sectional structure of sample #3 is shown in Fig.4.5. It shows that the coated sample consists of two-layers: a first (inner) layer of Ni(Al) and a second layer of a two phase structure of Ni(Al) and Al(Fe, Ni) with the total coated thickness of 280  $\mu\text{m}$ , twice the thickness of the coatings developed at 800 °C. The EDS line analysis of this sample in Fig. 4.5 (right) indicates that the Ni(Al, Co) layer contains (52-48 at.%)Ni, (48-44 at.%)Al, and (4-1.5 at.%)Co and the Al(Fe, Ni) layer (64-60 at.%)Al, (20-14 at.%)Fe, and (23-16 at.%)Ni. The structure shows many cracks and voids at the interface between layer ① and substrate, as well as in the higher parts nearer the surface of layer ②. The inhomogenities of this coating may indicate that the coating will be unable to protect the substrate. The inhomogenous structure may also decrease coating performance significantly and may lead to delamination of the coating. The results suggest the conclusion that the temperature of the coating process affects the deposition of the coating, the coating thickness, and the structure of the phase constituents of the coated sample.

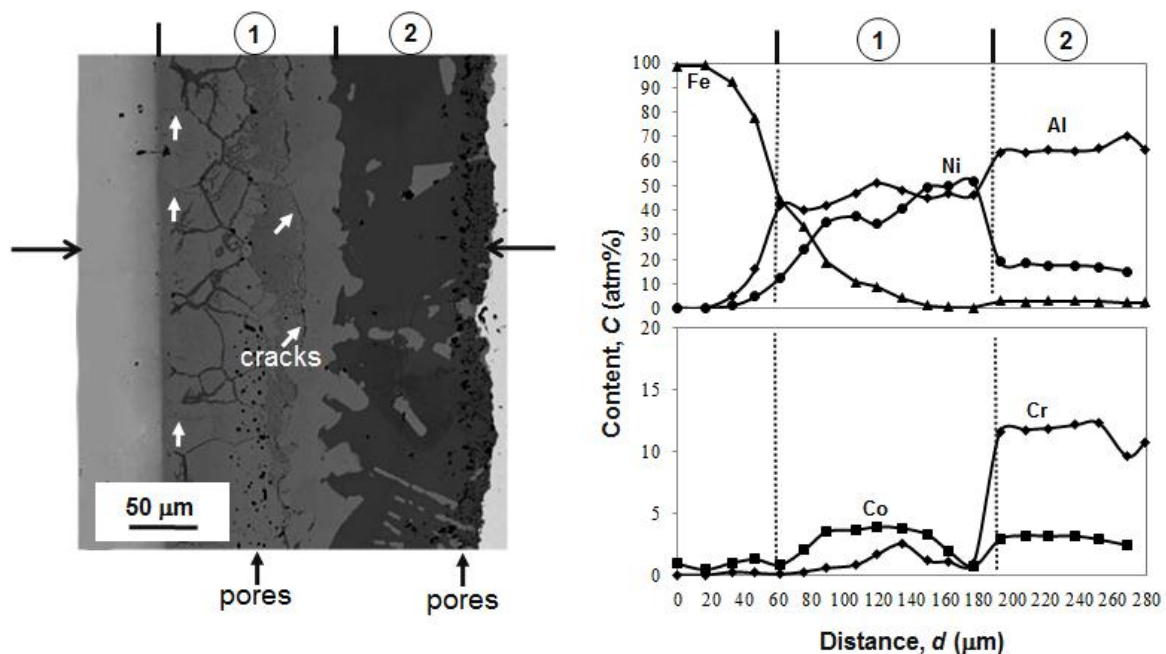


Figure 4.5. Cross-sectional microstructure and composition gradients of Ni(5%)Co plating, followed by Cr-Al pack diffusion coating at 1000 °C.

## 8.5 High temperature oxidation results

The effect of high temperature environment exposure was examined by subjecting the as coated samples to isothermal conditions for different periods, beginning from ambient temperature up to 800 °C. The results of the isothermal oxidation measurements are presented as the mass gain versus time for the coated sample as shown in Fig. 4.6.

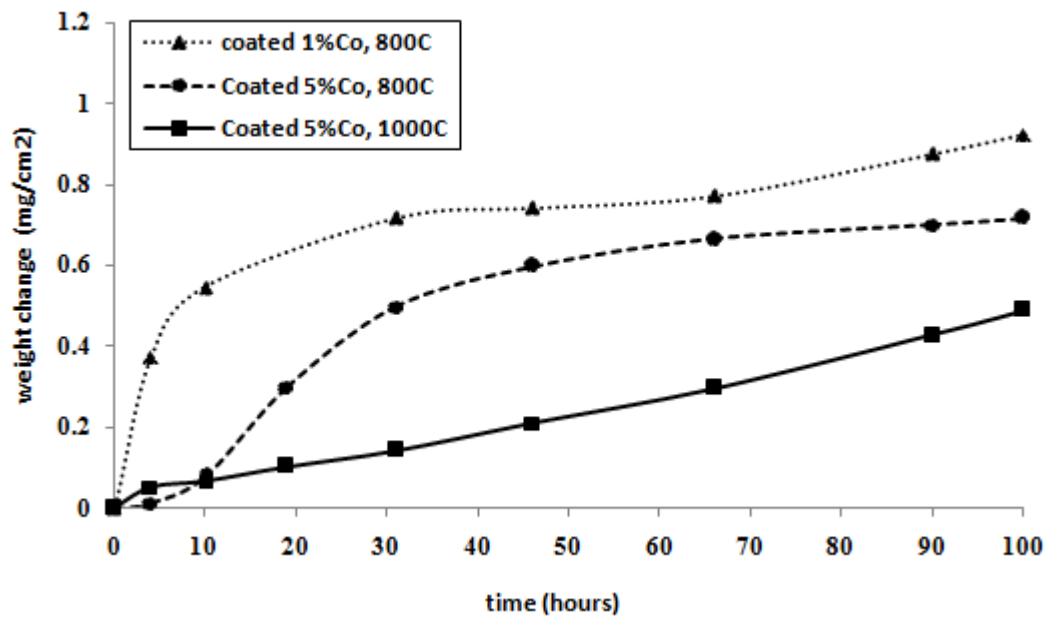


Figure 4.6. Mass gain per unit area versus time during oxidation of coatings at 800 °C for 100 h.

Oxidation is a function of temperature, however as Fig.4.6 shows, there are differences in the oxidation behaviors of the coatings formed at the two temperatures. Sample #3 has the lower oxidation rate and follows an approximately linear oxidation throughout the oxidation process by which unprotective oxide scale was formed. The oxidation kinetic of the sample developed at 800 °C is different from that for the sample developed at 1000 °C. The oxidation rate is parabolic for both samples developed at 800°C, and there are mass increments due to the formation of oxide in the coatings during the oxidation time. Sample #1 is oxidized at a

much higher rate than sample #2. The value of the kinetic constant for sample #1,  $k_p = 1.37 \times 10^{-9} \text{ g}^2 \text{ cm}^{-4} \text{ s}^{-1}$ , is one order of magnitude larger than for sample #2,  $k_p = 8.02 \times 10^{-10} \text{ g}^2 \text{ cm}^{-4} \text{ s}^{-1}$ . This implies that at this temperature condition, sample #2 provides significantly better protection. At 66h of exposure to 800 °C, the oxide thickening reaches the maximum mass gain for sample #2. After this point the increment of mass gain slows and the thickness of the scale remains approximately constant or grows very slowly.

The cross-sectional microstructures of the three oxidized samples are presented in Fig.4.7. The total thickness of the coated layer has remarkably increased due to the continuous oxide formation on the surface during the oxidation. After the oxidation, the thickness was about 165  $\mu\text{m}$ , 150  $\mu\text{m}$ , and 330  $\mu\text{m}$  for samples #1, #2, and #3, respectively. Further, there is an oxide scale on the outermost part of the coating, as indicated by the homogeneous dark area clearly shown on the top of samples #1 and #2 which were developed at 800°C. The thickness of the oxide scale was about 23  $\mu\text{m}$  for sample #1 and 26  $\mu\text{m}$  for sample #2. There was internal oxidation in sample #1, indicated by the oxide particles in the inner layer, probably caused by the reaction of oxygen with the elements of Ni which form a NiO. In sample #3, which was developed at 1000°C, there is only very little oxide scale at the top of the coating, likely due to the porous structure of as-coated sample (Fig.4.5), allowing oxygen to diffuse inwards to the substrate where it reacts with the Al and Ni to form  $\text{Al}_2\text{O}_3$  and NiO.

Fig. 4.7 (right) shows elemental maps of the oxidized samples obtained from the areas in Fig.4.7 (left). There are strong signals of O on the surface of samples #1 and #2. Both Al and O coexisted to form  $\text{Al}_2\text{O}_3$ . Mapping analysis indicates that the internal oxide rich in Ni and O, indicating the formation of NiO phase and is only observed in samples #1 and #3. This phase may have a negative effect on the oxidation resistance. These results were associated

with oxidation kinetic curve in Fig. 4.6, which showed that sample #2 has a slow oxidation rate and provides significant better protection than sample #1 and #3.

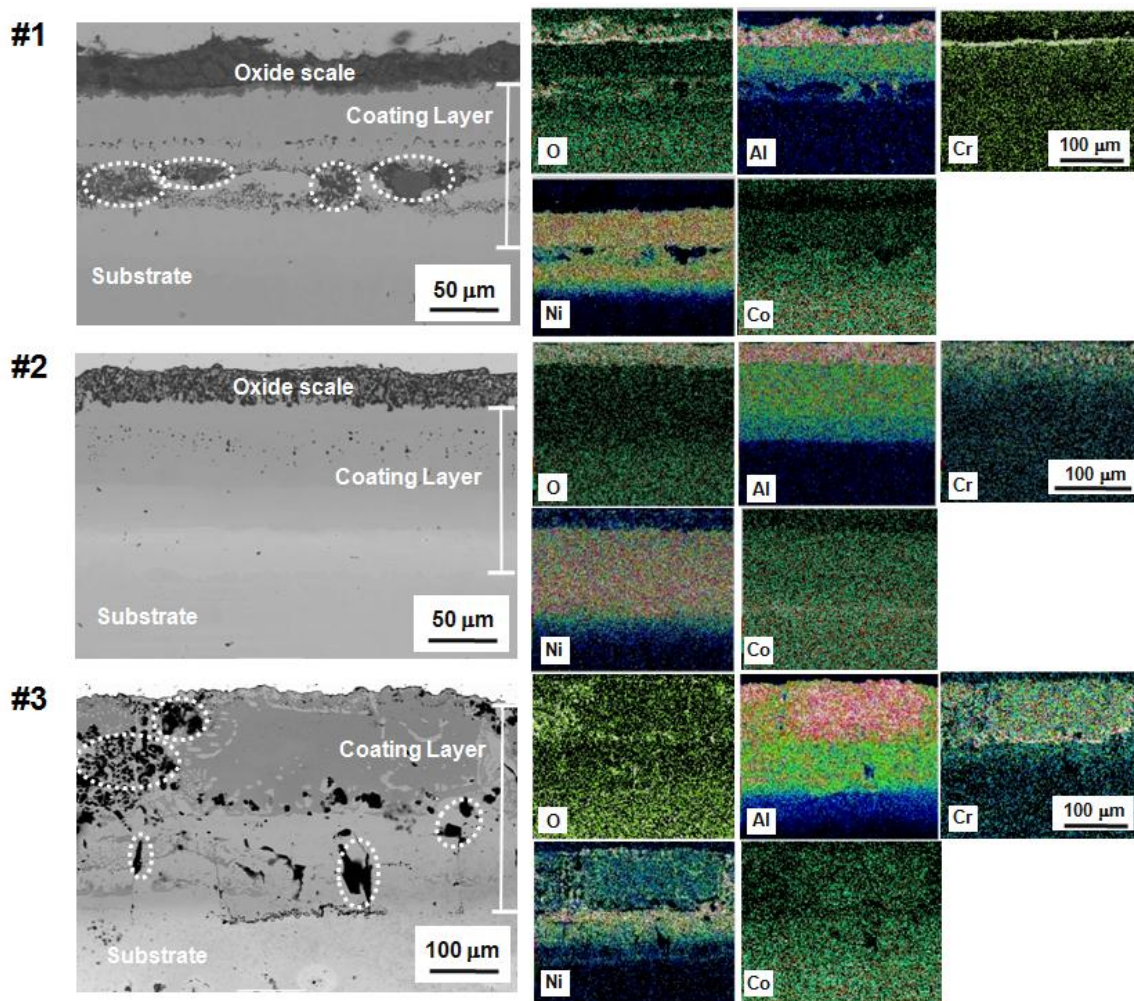


Figure 4.7. Cross-sectional micrographs (left) and elemental distribution (right) of the oxidized samples developed at various conditions: Sample #1: Ni(1%)CoCrAl, coated at 800 °C; Sample #2: Ni(5%)CoCrAl, coated at 800 °C and Sample #3: Ni(5%)CoCrAl, coated at 1000 °C.

## 8.6 Nanostructure of the as-coated sample

An XTEM analysis was performed to examine the detailed microstructure of the coated layer. Fig. 4.8a shows XTEM bright-field images of sample #1 obtained from each of the coated layers. Fine grain is characterized in layers ① and ② and coarse grain with the size

of above 1  $\mu\text{m}$  in layer ③. There are interfacial cracks in layer ②, probably propagated by the growth of voids like those shown in the SEM image (Fig.4.3).

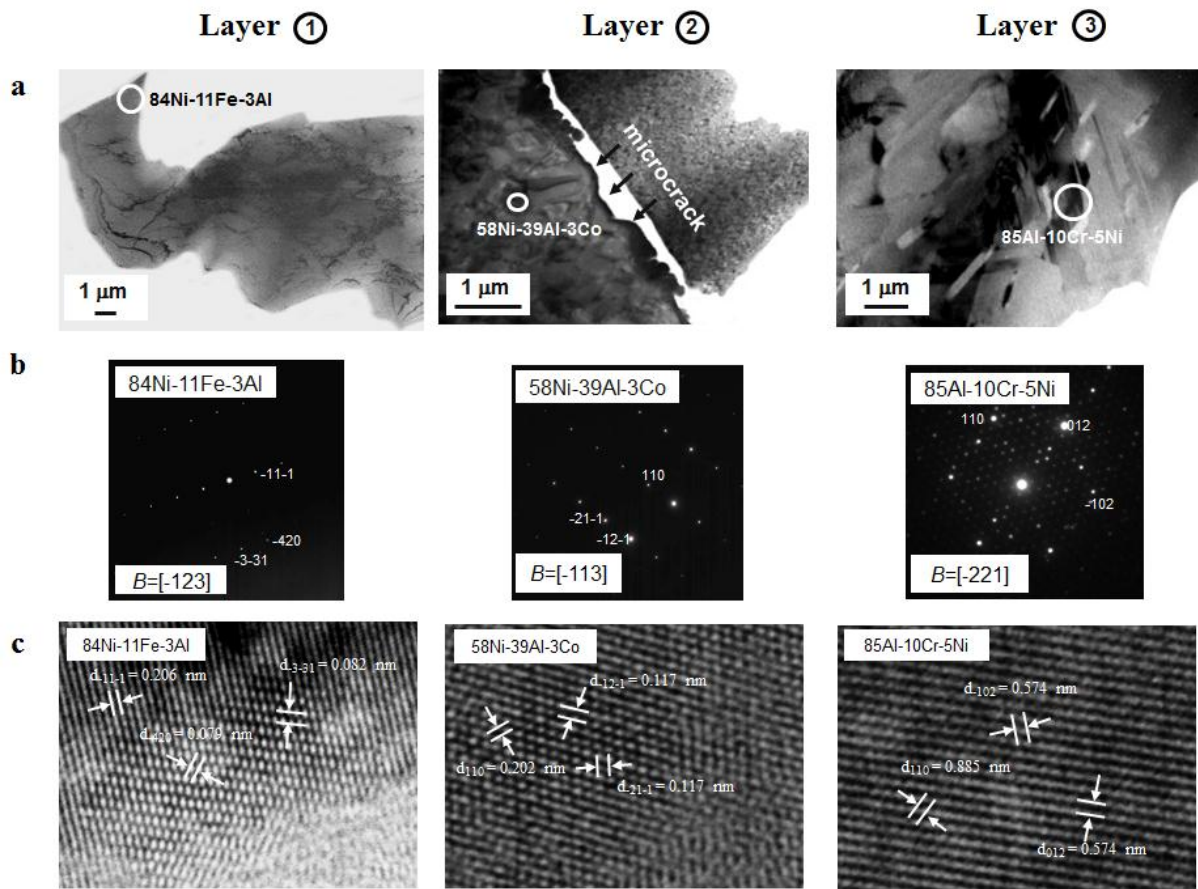


Figure 4.8. Nanostructure of sample #1: (a) bright field XTEM images, (b) SAED patterns and (c) HRTEM images obtained from the circled area.

Chemical composition is acquired by point EDS-TEM analysis. Furthermore, the XTEM observation of sample #2 is presented in Fig.4.9a. It can be seen that the grain size in layers ① and ③ is larger than the grain size in layer ②. Fig. 4.10a shows XTEM images of sample #3. The grain size in layers ② and ③ is smaller than that in sample #2. Void was observed in the interface layer ① and layer ②. It might influence the durability of the coating system. It is recognized that the chemical composition obtained from EDS in the TEM analysis agrees with the EDS result in SEM analysis.

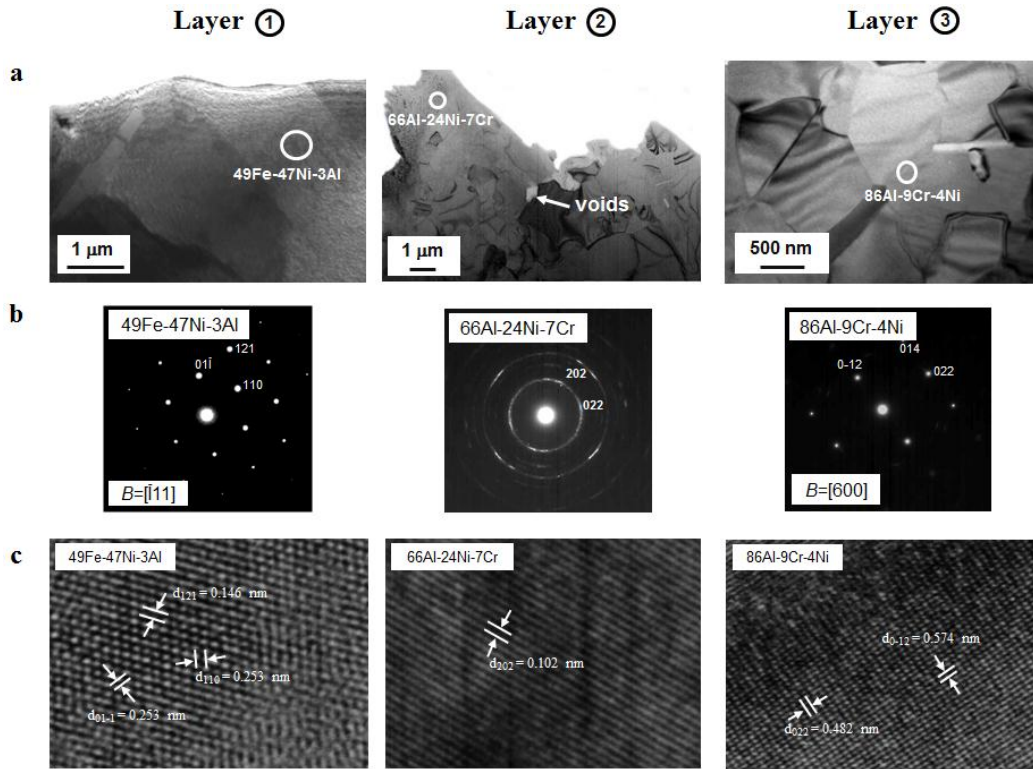


Figure 4.9. Nanostructure of sample #2: (a) bright field XTEM images, (b) SAED patterns and (c) HRTEM image obtained from the circled area.

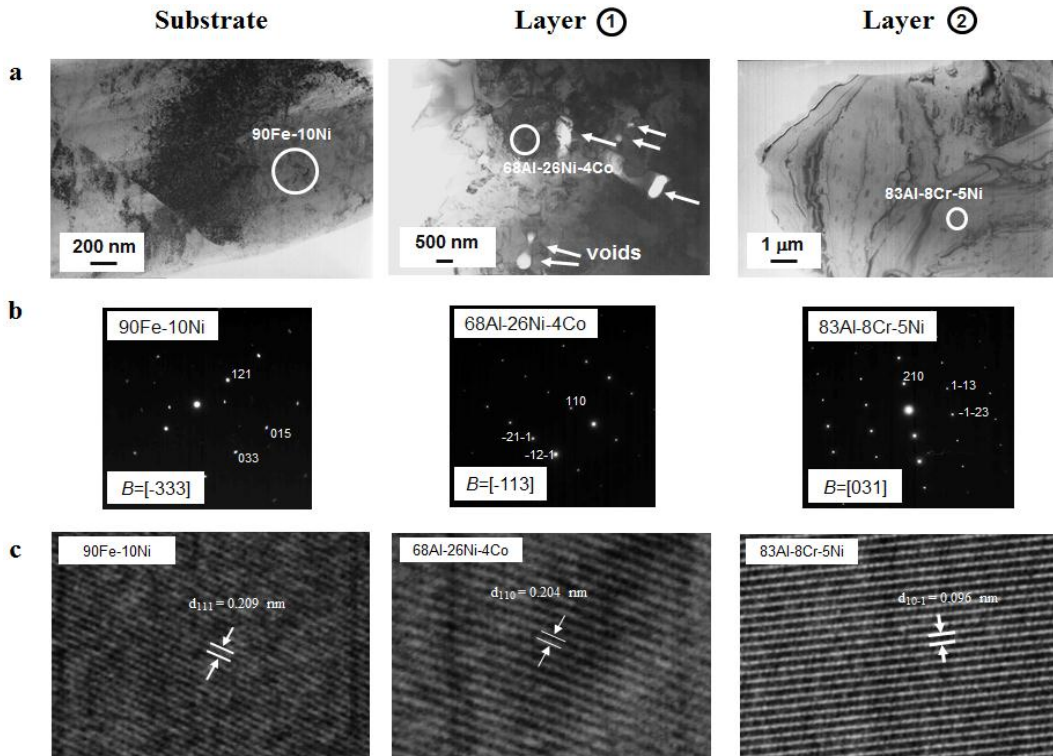


Figure 4. 10. Nanostructure of sample #3: (a) bright field XTEM images, (b) SAED patterns and (c) HRTEM images obtained from the circled area.

The oxidation properties of the coated sample may also depend on grain size besides its composition. The smaller the grain size, the larger the total boundary surface area per unit volume which are vulnerable to oxidation because the interface usually is the preferred diffusion pathway for oxygen. Thus, the best oxidation resistance of sample #2 would partially benefit from its biggest grain size in top coating layer.

## 8.7 Phase constitution of the NiCoCrAl coating layer

Crystallographic technique is the main tool for phase identification in multiphase material. Thus, systematic phase identification by electron diffraction pattern indexation routines was performed. Fig. 4.8b, 4.9b, and 4.10b show the corresponding SAED patterns obtained from circled area in the TEM analysis and associated with its EDS chemical composition. Symbol B in the SAED pattern represents the incident electron beam direction of the diffraction pattern. Based on the composition and diffraction analyses, the crystal structure, phase and lattice parameters were determined as detailed in Table 4.1.

Table 4.1. Chemical composition, phase identification, and lattice parameters in the coated layers identified by SAED patterns.

No	Local Composition - EDS	Crystal Structure	Phase	Lattice Parameter (Å)- DP		
				<i>a</i>	<i>b</i>	<i>c</i>
#1	94Fe-5Ni	BCC	$\alpha$ -Fe	2.86	-	-
	84Ni-11Fe-3Al	FCC	$\gamma$ -(Ni,Fe)	3.54	-	-
	86Ni-10Cr-2Al	FCC	(Ni)	3.53	-	-
	58Ni-39Al-3Co	Cubic	$\beta$ -(Ni,Al)	2.867	-	-
	74Al-23Ni	Orthorhombic	Al <sub>3</sub> Ni	6.59	7.35	4.80
	85Al-10Cr-5Ni	Hex	$\zeta$	17.7	-	12.4
#2	96Fe-4Ni	BCC	$\alpha$ -Fe	2.86	-	-
	49Fe-47Ni-3Al	FCC	$\gamma$ -(Ni,Fe)	3.58	-	-
	66Al-24Ni-7Cr	Cubic	$\beta$ -Al(Ni,Cr)	2.88	-	-
	74Al-23Ni	Orthorhombic	Al <sub>3</sub> Ni	6.59	7.35	4.80

	86Al-9Cr-4Ni	Hex	$\zeta$	17.7	-	12.4
#3	90Fe-10Ni	FCC	$\gamma$ -(Fe,Ni)	3.62	-	-
	84Ni-12Co	FCC	$\alpha$ -(Ni,Co)	3.52	-	-
	68Al-26Ni-4Co	Cubic	$\beta$ -(Al,Ni)	2.91	-	-
	83Al-8Cr-5Ni	Hex	$\zeta$	17.7	-	12.4

The results show that the phase constituent of sample #1 is  $\alpha$ -Fe,  $\gamma$ -(Ni,Fe), (Ni) and  $\beta$ -NiAl with cubic structure for substrate, layer ①, diffusion zone ② and layer ② in bright field TEM image (Fig.4.8a). In addition, orthorhombic  $\text{Al}_3\text{Ni}$  and hexagonal  $\zeta$  phases were identified in the diffusion zone ③ and layer ③, respectively. Representing the phase identification in layer ①, the Fe-Ni binary system could be considered. *Bcc*  $\alpha$  phase was formed in the composition range of 0-15 at.%Ni, whereas the *fcc*  $\gamma$  phase was generated in the range of 35-100 at.%Ni [70]. It was found that  $\alpha$  phase of 94Fe-5Ni has a lattice parameter of  $a = 0.286$  which is smaller than the constant of pure Fe (0.2867 nm). In addition, a cubic phase labeled by  $\gamma$ -(Ni,Fe) was found to have a composition of 84Ni-11Fe-3Al with lattice parameter of  $a = 0.354$  nm. The lattice parameter of the  $\gamma$ -(Ni,Fe) phase increases linearly from pure Ni (0.3519 nm) with increasing Fe constant and probably influenced by the Al constituent in the compound. The composition of other *fcc* (Ni) phase was 86Ni-10Cr-2Al and its Al composition was just 2 at%, consequently Ni-Cr binary phase is considered to be applied. In the case of the lattice parameter of  $\gamma$ (Ni) for Ni-10at.%Cr, the measured value was in excellent agreement with the  $a = 0.353$  nm reported by Mishima et al [71]. Furthermore, the main composition in the layer ② was Ni-Al. Accordingly, it is known that six intermetallic compounds can exist in an Ni-Al system, namely  $\text{Al}_3\text{Ni}$ ,  $\text{Al}_3\text{Ni}_2$ ,  $\text{Al}_4\text{Ni}_3$ ,  $\text{AlNi}$ ,  $\text{Al}_3\text{Ni}_5$  and  $\text{AlNi}_3$  [72]. For the composition of 58Ni-39Al-3Co, it fitted with CsCl type cubic having lattice parameter of  $a = 0.2867$  nm. However, Co concentration in these compounds may affect the lattice parameter to decrease relative to the value  $a = 0.2887$  nm as reported for  $\beta$ -(Ni,Al) at the stoichiometric composition

[73]. In the layer ③, the calculated lattice parameter of 74Al-23Ni was in a good agreement with Al<sub>3</sub>Ni (Fe<sub>3</sub>C-type orthorhombic) crystal structure. The value for the Al<sub>3</sub>Ni phase was  $a = 0.659$  nm,  $b = 0.735$  nm, and  $c = 0.480$  nm which compares well with the experimental value and other theoretical data [74]. At higher Al concentration in the range of 70-88 at.% mixed with 14-20 at.%Cr and 3-9at.%Ni, the  $\zeta$ -phase was formed in this ternary system [75-76]. The  $\zeta$ -phase was found to be stable at the temperature range of 700 °C – 900 °C in similar compositional limits [77]. In the present work, the  $\zeta$ -phase was identified in the 85Al-10Cr-5Ni with hexagonal structure and the lattice parameter was calculated as  $a = 17.7$  nm and  $c = 12.4$  nm.

At same temperature coating process, the phase constituent of sample #2 is similar with sample #1. The difference in Co content did not affect the phase transformation. The 96Fe-4Ni was identified as cubic  $\alpha$ -Fe with the lattice parameter  $a = 0.286$  nm. Moreover, the calculated lattice parameter of 49Fe-47Ni-3Al slightly increases to be  $a = 0.358$  nm from the composition of 84Ni-11Fe-3Al identified in sample #1 due to the high concentration of Fe. The composition of 66Al-24Ni-7Cr obtained from coated layer matches with  $\beta$ -Al(Ni,Cr) cubic structure and the existence of Cr up to 7at.% should be concerned to the calculation of lattice parameter. In this case, the value is very close to the Cr lattice parameter,  $a = 0.28839$  nm and at this point  $\beta$ -Al(Ni,Cr) lattice parameter has been measured to be  $a = 0.288$  nm. The 74Al-23Ni has been described to be orthorhombic Al<sub>3</sub>Ni as mentioned earlier in sample#1. Moreover,  $\zeta$  hexagonal structure was also identified in 86Al-9Cr-4Ni.

In that case of higher temperature, the phase constituent of sample #3 was  $\gamma$ -(Ni,Fe),  $\alpha$ -(Ni,Co),  $\beta$ -(Ni,Al) and  $\zeta$  phase from substrate to outer layer. The 90Fe-10Ni was identified as cubic  $\gamma$ -(Ni,Fe) with lattice parameter  $a = 0.362$  nm. Cubic  $\alpha$ -Fe as identified in 94Fe-5Ni (sample #1) has been changed to cubic  $\gamma$ -(Ni,Fe) when the composition was developed at higher temperature (90Fe-10Ni, sample #3). The phase contained in 84Ni-12Co is  $\alpha$ -(Ni,Co) with

cubic crystal structure while the phase in 68Al-26Ni-4Co is  $\beta$ -(Ni,Al). In this case, the lattice parameter slightly increases to be  $a = 0.291$  nm comparing with similar structure in samples #1 and #2. Otherwise, the  $\zeta$  phase with the homogeneity range at 800 °C was found to be matched with the identified phase of 83Al-8Cr-5Ni at 1000°C and the similar occurrence was investigated by V.Raghavan [78].

In order to verify the phase analysis and lattice parameter calculation for the NiCoCrAl coatings as described earlier, three types of sample were also analyzed using HRTEM image (Fig. 4.8c, 4.9c and 4.10c). The lattice fringe analysis was performed by using a Fourier Mask Filtering method, which was possible by employing a Digital Micrograph<sup>TM</sup> program (DM, Gatan Inc.). The Fourier mask filtering method is one of the techniques to enable a quantitative analysis of high resolution XTEM image. Detail examinations were carried out by comparing the calculation of lattice parameter from SAED patterns in Fig. 4.8b, 4.9b and 4.10b with interplanar spacing from HRTEM images symbolized by  $d$ . It is shown that the measured interplanar spacings in (-11-1), (-3-31) and (-420) from 84Ni-11Fe-3Al (Fig.4.8c) have interplanar spacing of  $d = 0.206, 0.082$  and  $0.0079$  nm, respectively. The result corresponds to the diffraction pattern from the same composition area with incident electron beam direction,  $B = [-123]$  as shown in Fig.4.8b. Therefore, the analysis of interplanar spacing can emphasize the phase identification in the coating layer. By using similar method, verification of all phases is clearly described in HRTEM images.

## 8.8 Conclusions

This paper describes characterization of Ni-based coatings on carbon steel by means of electron microscopy. The following conclusions may be made from the experimental results:

1. Electroplating followed by pack cementation successfully developed NiCoCrAl multi-layer coatings on carbon steel substrate.

2. The thermal treatment had a stronger effect on the coating phase constituents than the Co content in the NiCo electroplating. The addition of 1 wt% or 5 wt% of Co in the NiCoCrAl coating systems increases the hardness value from 810 HVN (1 wt% Co) to 1027 HVN (5 wt% Co). The coating hardness on the substrate was more than nine times that of the initial carbon steel substrate.
3. The value of kinetic constant of the Ni(1%)CoCrAl sample,  $k_p = 1.37 \times 10^{-9} \text{ g}^2 \text{ cm}^{-4} \text{ s}^{-1}$ , is one order of magnitude higher than of the Ni(5%)CoCrAl sample,  $k_p = 8.02 \times 10^{-10} \text{ g}^2 \text{ cm}^{-4} \text{ s}^{-1}$ . This implies that at a 800 °C temperature condition, a sample with 5 wt% Co provides significant protection.
4. Most phases are directly and simply shown by electron diffraction and high resolution XTEM images of the particular coating layers prepared by ion milling.
5. The study compares the experimental and theoretically available values and shows a good match of the lattice parameters.
6. The phase sequence from the substrate of the 800 °C coated sample is  $\alpha(\text{Fe}) \rightarrow \gamma(\text{Ni, Fe}) \rightarrow (\text{Ni}) \rightarrow \beta(\text{Ni, Al}) \rightarrow \text{Al}_3\text{Ni} \rightarrow \zeta$ , and for the 1000 °C coated sample it is  $\gamma(\text{Ni, Fe}) \rightarrow \alpha(\text{Ni, Co}) \rightarrow \beta(\text{Ni, Al}) \rightarrow \zeta$ .
7. Comparing the results of the three samples of coatings, clearly show the advantages of a higher Co concentration.

## Chapter 5

### Oxidation Behavior of Ni-Based Coated Layer

This chapter presents the oxidation behavior of the coated samples developed by different temperature of pack cementation in isothermal oxidation at 800 °C for 100 hours. Different coating compositions provides different protective properties due to the nature of the different oxides growing on them. The composition of the alloy, as well as the exposure time and temperature, greatly influence the oxide layer created.

The service-life of NiCoCrAl coatings depend greatly on the aluminum and chromium content. The depletion of aluminum and chromium are due to formation and re-healing the protective oxide layer which are the main reason of degradation in these coatings. Formation of adherent, continuous, dense, and stable protective oxide is affected by factors such as chemical composition of NiCoCrAl coatings, environmental condition, working temperature and coating processes. Therefore, investigation of the effect temperature process on oxidation behavior of coated carbon steel becomes important.

#### 5.1. Oxidation kinetics

Fig. 5.1(a) shows the oxidation kinetics of NiCoCrAl coated samples at 800 °C for 100 h. The mass gain increases gradually with time and the oxidation kinetics approximately follows parabolic rate law. The results exhibited the sample developed at 1000 °C has better oxidation behavior up to 70 h than the other two samples developed at 800 and 900 °C due to its relatively low oxidation rate. The breakaway oxidation occurred after 90 h of exposure for sample developed at 1000 °C and it might indicate the spallation of oxide scale and it caused less protective for carbon steel substrate. Therefore, the sample developed at 800 °C was more protective for longer oxidation time at this atmosphere. The growing oxide curves were divided

in two parts: an initial fast growing part and followed by a steady part. This describes the two stage of  $\text{Al}_2\text{O}_3$  growth well (transient oxide growth, e.g.  $\delta$ - $\theta$ - $\text{Al}_2\text{O}_3$  or possibly spinel  $\text{NiAl}_2\text{O}_4$ , followed by  $\alpha$ - $\text{Al}_2\text{O}_3$ ).

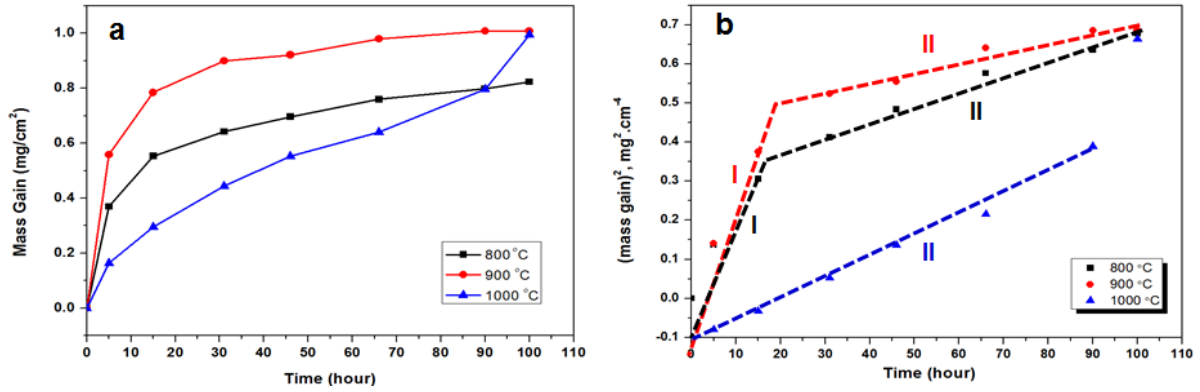


Figure 5.1. (a) The oxidation mass gain and (b) rate constant,  $k_p$ , for three types of the coated samples at 800 °C in air.

Previous work [79] reported that the increase of the mass gain and the thickness of oxide layer followed a square law for diffusion-controlled oxidation behavior. Thus, the parabolic rate constant,  $k_p$ , can be assessed by a linier least-squares algorithm from the following equation [80]:

$$(\Delta m/A)^2 = k_p \cdot t \quad (5 - 1)$$

Where  $(\Delta m/A)$  is the oxidation mass gain per unit surface area (mg/cm<sup>2</sup>),  $t$  is the oxidation time in seconds (s). The square of mass gain obtained from the two stage  $\text{Al}_2\text{O}_3$  growth of all samples had a nearly linier line as shown in Fig. 5.1(b) and its  $k_p$  value is given in Table 5.1. The results revealed that the rate of oxidation for the sample developed at 800 °C was higher (I stage) and lower ( II stage) than those at 900 and 1000 °C, leading to the fast transformation of metastable  $\text{Al}_2\text{O}_3$  at I stage and slow growth of stable  $\alpha$ - $\text{Al}_2\text{O}_3$  at the II stage.

Table 5.1. Measured parabolic rate constant at two stage of oxide growth for three types of the coated samples.

Pack Cementation Temperature, °C	$k_p$ ( $\text{g}^2/\text{cm}^4 \text{ s}$ )	
	I Stage	II Stage
800	$6.62 \times 10^{-6}$	$2.58 \times 10^{-6}$
900	$1.43 \times 10^{-6}$	$4.47 \times 10^{-6}$
1000	-	$2.74 \times 10^{-6}$

## 5.2. Surface morphologies and phases

Fig. 5.2 shows the surface morphologies and corresponding XRD patterns of oxide scale formed on the coated layer. It is observed that a cauliflower-like structure distributed on the surface of the coated sample developed at 800 °C after oxidation (Fig. 5.2(a)).

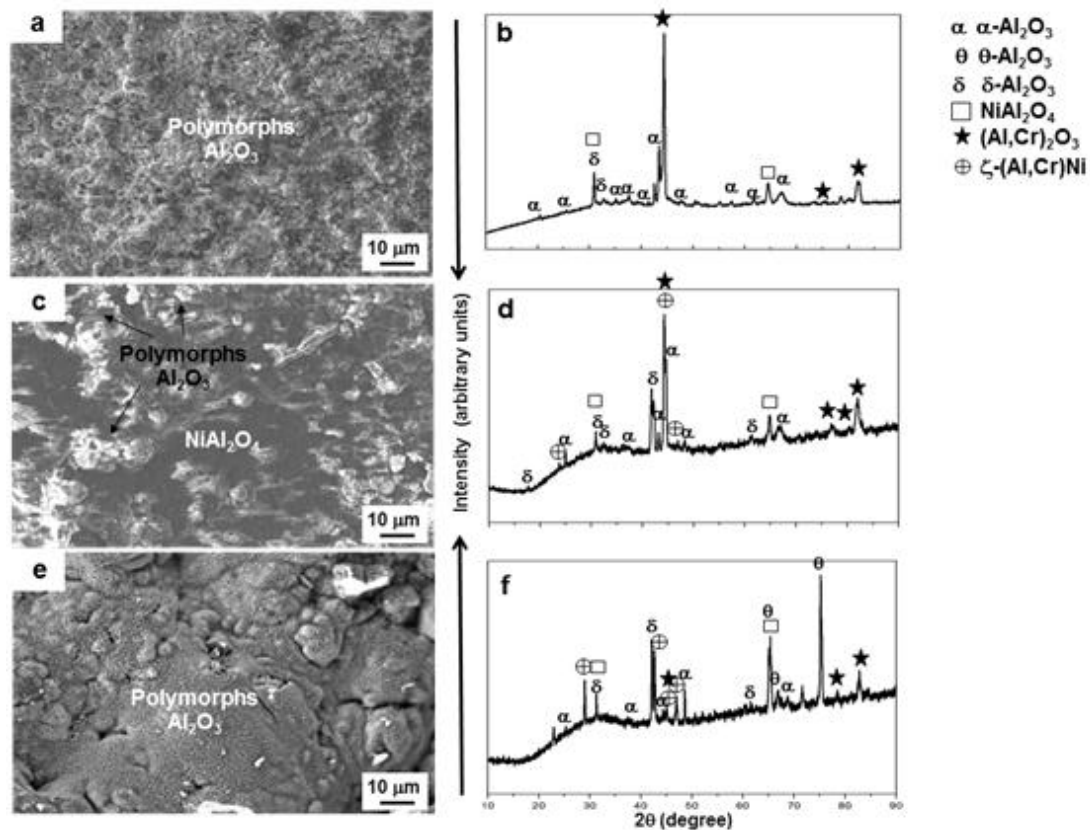


Figure 5.2. (left) SEM images showing the surface morphologies and (right) corresponding XRD patterns of three types of the coated sample after oxidation at 800 °C for 100 h : (a-b) 800 °C, (c-d) 900 °C, and (e-f) 1000 °C.

The XRD pattern, depicted in Fig. 5.2(b), shows that the sample mainly consists of  $\alpha$ - $\text{Al}_2\text{O}_3$  and small amount of  $\delta$ - $\text{Al}_2\text{O}_3$ , spinel  $\text{NiAl}_2\text{O}_4$ , and cubic  $(\text{Al,Cr})_2\text{O}_3$  phases. In the case of the coated sample developed at 900 °C, alumina particle is not homogeneously distributed on the surface as shown in Fig. 5.2(c). This oxide scale is identified as a mixture of predominant  $\delta$ - $\text{Al}_2\text{O}_3$  and  $\alpha$ - $\text{Al}_2\text{O}_3$  accompanied by spinel  $\text{NiAl}_2\text{O}_4$ , cubic  $(\text{Al,Cr})_2\text{O}_3$  and hexagonal  $\zeta$ - $(\text{Al,Cr})\text{Ni}$  phases (Fig. 5.2(d)). Eventually, the surface of the coated sample developed at 1000 °C shows a very rough cauliflower-like structure. This oxide is found to be several polymorphs alumina structures ( $\delta$ ,  $\theta$ ,  $\alpha$ ) and another phases of spinel  $\text{NiAl}_2\text{O}_4$ , cubic  $(\text{Al,Cr})_2\text{O}_3$ , and hexagonal  $\zeta$ - $(\text{Al,Cr})\text{Ni}$  phases. XRD phase identification (Fig. 5.2 (b, d, f)) confirms the formation of transient alumina and spinel phases at a relatively low temperature (800 °C). On the other hand, XRD and surface analysis show the amount of stable  $\alpha$ - $\text{Al}_2\text{O}_3$  increases as indicated by enhancement of its peak intensity in the coated sample developed at 800 °C and covers the entire surface of the coated sample.

### 5.3. Cross-sectional microstructure and elemental diffusion

The FE-EPMA method was employed to obtain the cross-sectional elemental mapping images of three types of as-coated samples as shown in Fig. 5.3. The microstructural images show that the multilayer were successfully formed on all samples. The homogenous layer was established with an approximate thickness of 140  $\mu\text{m}$ , 240  $\mu\text{m}$  and 406  $\mu\text{m}$  for the coated sample developed at 800 °C, 900 °C, and 1000 °C, respectively. These results reveal that the thickness increases with the increasing of the temperature of pack cementation process. The line analysis indicates that the formed phases were  $\alpha$ -Fe -  $\gamma$ (Ni) -  $\beta$ -(Ni,Al) -  $\text{Al}_3\text{Ni}$  -  $\zeta$ - $(\text{Al,Cr})\text{Ni}$  from the substrate to the outermost of the coated sample developed at 800 °C (Fig. 5.3(a)). At relatively higher temperature of the coating process, the formed phases are similar to the coated sample developed at 900 °C (Fig. 5.3(b)) and 1000 °C (Fig. 5.3(c)) and it is

identified as  $\gamma$ -Fe -  $\alpha$ (Ni,Co) -  $\beta$ -(Ni,Al) -  $\zeta$ -(Al,Cr)Ni from the substrate to the outermost layer. Those results are in good agreement with previous work [83] which comprehensively characterized the structure and phases formed on Ni-based coated layer.

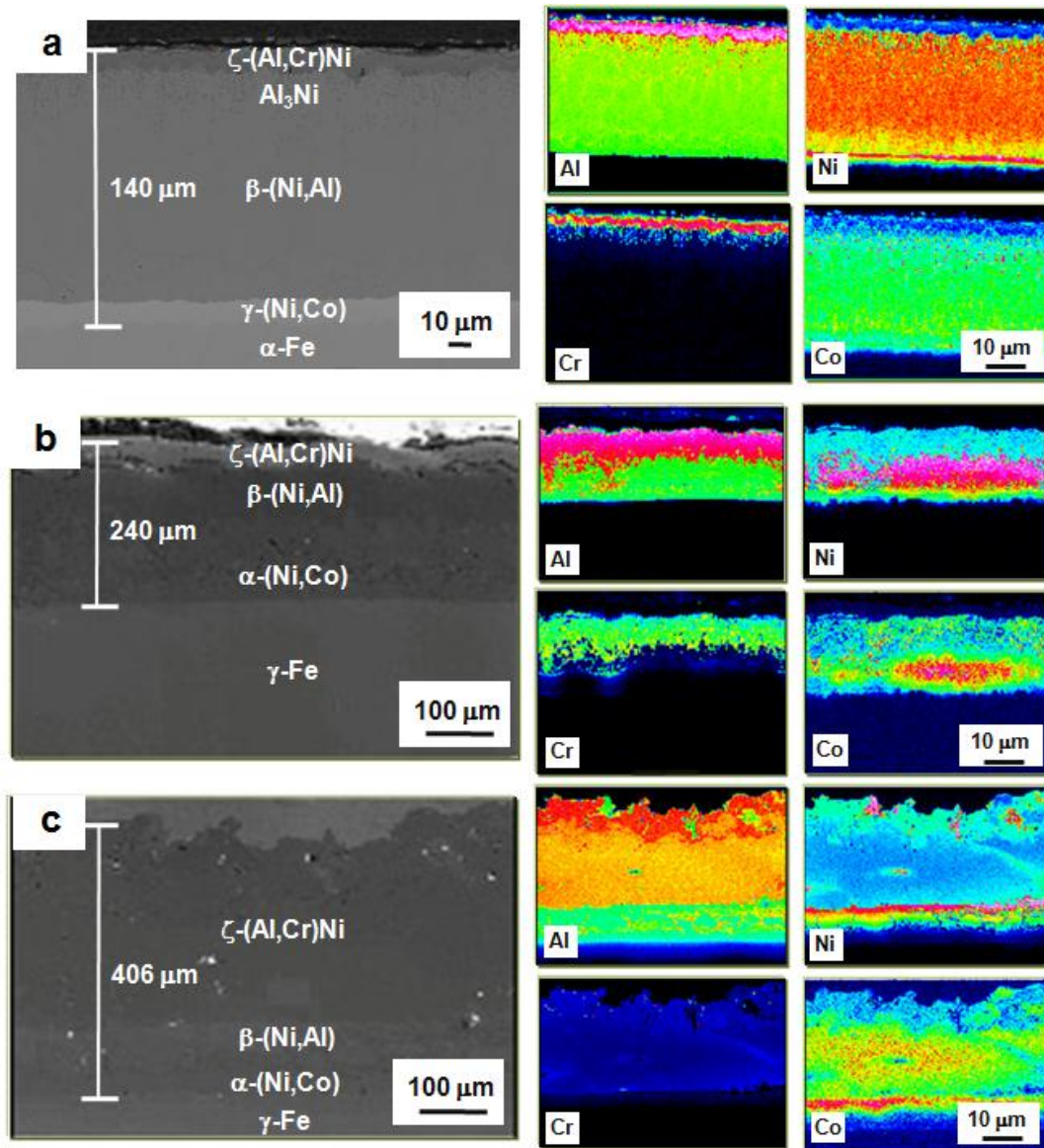


Figure 5.3. Cross-sectional micrographs (left) and corresponding elemental distribution (right) of three types of the samples developed at various temperatures: (a) 800 °C, (b) 900 °C, and (c) 1000 °C.

Trace amounts of Ni, Co, Cr, Al are noticeably detected for all as-coated samples (Fig. 5.3(right)). Different condition of coating can be distinguished in which strong intensity of Cr

was not exhibited in both samples developed at 900 °C (Fig. 5.3(b)) and 1000 °C (Fig. 5.3(c)). Strong intensity of Cr on the top layer of the coated sample developed at 800 °C (Fig. 5.3(a)) promotes the formation of intermetallic phase such as Al<sub>3</sub>Ni which will contribute to stabilizing the oxide scale after oxidation.

#### 5.4. Oxide Formation

The FE-EPMA results for three types of the coated samples after oxidation are shown in Fig. 5.4. The oxide scale thickness is about 6, 15 and 30 μm for sample developed at 800 °C, 900 °C, and 1000 °C, respectively. Thin and less porous oxide scale is continuously formed on the surface of 800 °C coated sample. Further, a good adherent between metal/oxide interfaces is observed on the 800 °C coated sample. The growth of alumina scale is accelerated by formation of orthorhombic Al<sub>3</sub>Ni phase before the oxidation of 800 °C coated sample. The stable α-Al<sub>2</sub>O<sub>3</sub> formed on the 800 °C coated sample is likely to be a diffusion barrier for oxygen to diffuse inward and nickel to diffuse outward from the coated layer.

On the contrary, a quite thick and porous structure has been observed on the 900 °C (Fig. 5.4(b)) and 1000 °C (Fig. 5.4(c)) coated samples. This typical structure propagates the high activity of oxygen to diffuse inward beneath the oxide layer, thus internal oxidation occurs on these two samples. It can be readily recognized from the strong intensity of oxygen element either on the surface or metal layer of 900 °C and 1000 °C coated samples (Fig. 5.4b-c(right)). Moreover, the outward diffusion of Ni, Cr, and Co is also observed in these two samples. The reaction of these elements resulted in the formation of spinel NiAl<sub>2</sub>O<sub>4</sub> and cubic (Al,Cr)<sub>2</sub>O<sub>3</sub> phases which thickens the oxide layer. Therefore, in line with the above described by surface and XRD analysis, it can be concluded that sample developed at 800 °C is a better oxidation resistance than the other two coated samples with different temperature of pack cementation process.

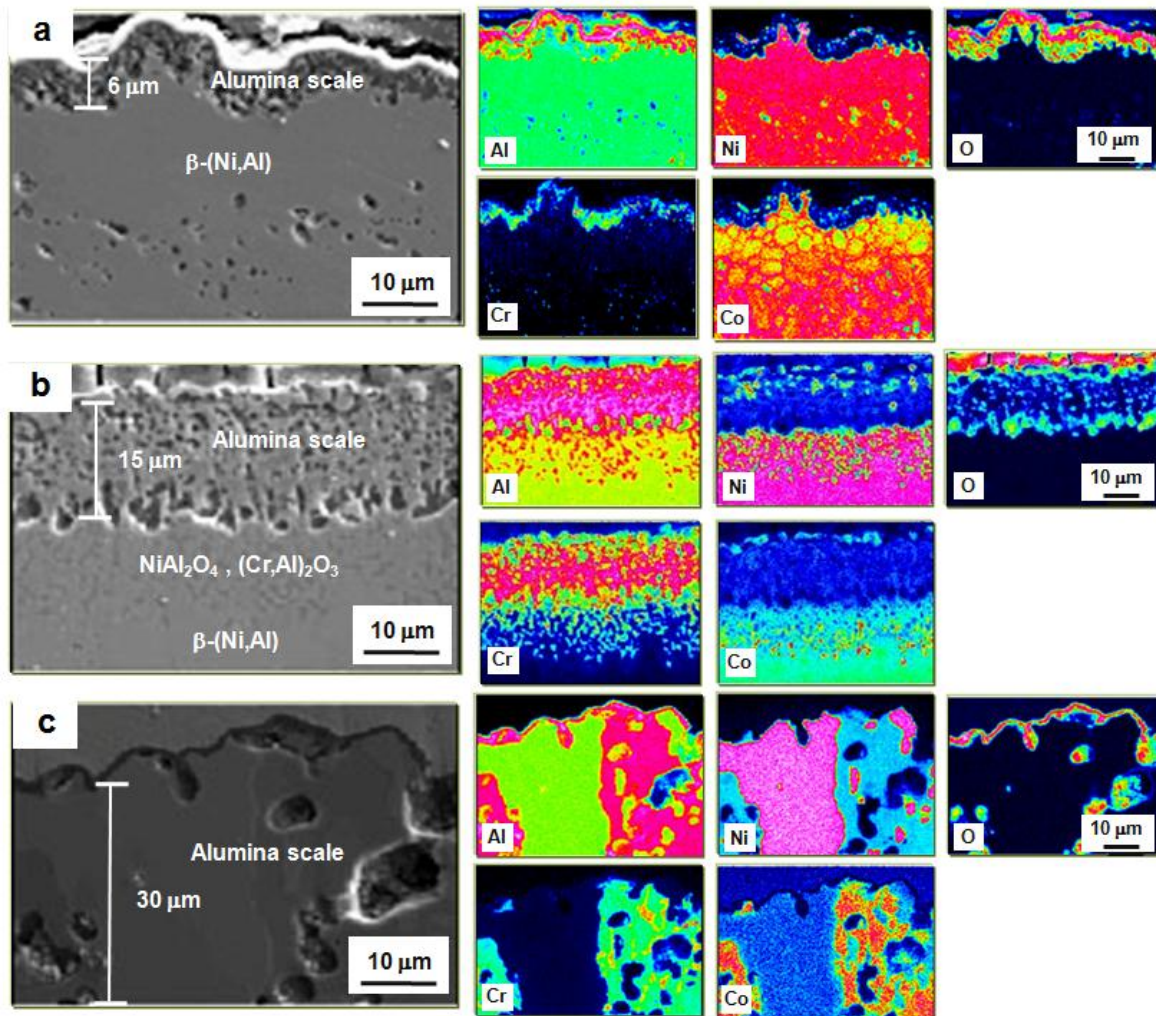


Figure 5.4. Cross-sectional micrographs (left) and corresponding elemental distribution (right) after oxidation at 800 °C for 100 h in air for the samples developed at various temperatures: (a) 800 °C, (b) 900 °C, and (c) 1000 °C.

## 5.5. Conclusions

The isothermal oxidation of NiCoCrAl coated layer at 800 °C was investigated. The following conclusions can be drawn from this investigation:

1. The oxidation kinetics at 800 °C of the coated samples obeys the parabolic rate law. It is primarily controlled by the growth of alumina layer.
2. The investigations show that the temperature of the coating process affects the deposition

of the coating, the coating thickness, and the structure of the phase constituents of as-coated sample, leading to have dissimilar oxidation behavior.

3. The existence of  $\text{Al}_3\text{Ni}$  phase on sample developed at  $800\text{ }^\circ\text{C}$  contributes to stabilizing the formation of  $\alpha\text{-Al}_2\text{O}_3$ .
4. The metastable  $\text{Al}_2\text{O}_3$  associated with spinel structure is formed in all as-coated samples after oxidation at  $800\text{ }^\circ\text{C}$  for 100 h.
5. The sample developed at  $800\text{ }^\circ\text{C}$  shows better oxidation resistance due to the fast transformation of metastable  $\text{Al}_2\text{O}_3$  at the transient stage and slow growth of  $\alpha\text{-Al}_2\text{O}_3$  from the intermediate stage up to the final stage of 100 h.
6. The oxide scale on sample developed at  $800\text{ }^\circ\text{C}$  mainly consists of  $\alpha\text{-Al}_2\text{O}_3$  with continuous, thin, and less porous structure. Thus, it possesses the capability as a diffusion barrier for oxygen to protect the carbon steel substrate when subject to severe oxidation.

## Chapter 6

### Formation of Meta-Stable Al<sub>2</sub>O<sub>3</sub> Scale during Oxidation

This chapter presents the formation of metastable Al<sub>2</sub>O<sub>3</sub> on NiCoCrAl coated layers during initial stage for up to 100 h exposure time under isothermal oxidation at 800 °C in air. The metastable Al<sub>2</sub>O<sub>3</sub>, which is based on the spinel structure often form not only in the transient oxidation stage but also at lower temperature of oxidation [83-85]. Alumina exists in several polymorphs crystalline structures:  $\eta$ -,  $\gamma$ -,  $\delta$ -,  $\theta$ -,  $\beta$ -,  $\kappa$ -,  $\chi$ -, and  $\alpha$ -Al<sub>2</sub>O<sub>3</sub>. These structures have very similar *d*-spacings, which makes difficult the precise solution of the structure by XRD. Therefore, selected-area electron diffraction (SAED) in TEM is a powerful technique to analyze the Al<sub>2</sub>O<sub>3</sub> polymorphs.

For multilayer NiCoCrAl coatings, phase formation and stability are critical issues due to no oxide ternary map diagram of Ni-Cr-Al system at temperature of 800 °C. Few investigations have been conducted at the lower temperature of 950 °C by Nicholas *et al.* [86] and M. Seraffon *et al.* [87]. Kuenzly and Douglass [88] studied oxidation of polycrystalline  $\gamma$ '-Ni<sub>3</sub>Al and found that the scale formed at 900 °C consisted of an outer layer of NiO, an intermediate layer of NiAl<sub>2</sub>O<sub>4</sub> and an inner layer of  $\alpha$ -Al<sub>2</sub>O<sub>3</sub>. Recent data published by M. Seraffon *et al.* showed that Ni-Cr-Al ternary oxide predominantly existed at 900 °C [89]. It has been pointed out that lowering the oxidation temperature from 950 °C to 900 °C would appear to promote the formation of transient Al<sub>2</sub>O<sub>3</sub> and spinel.

#### 6.1. Phase constitution in as-coated and oxidized samples

Fig. 6.1 shows XRD patterns of as-coated and oxide scale formed on the coatings in the initial stages of 1 h and 15 h, the intermediate stage of 46 h, and the final stage up to 100 h of oxidation at 800 °C.

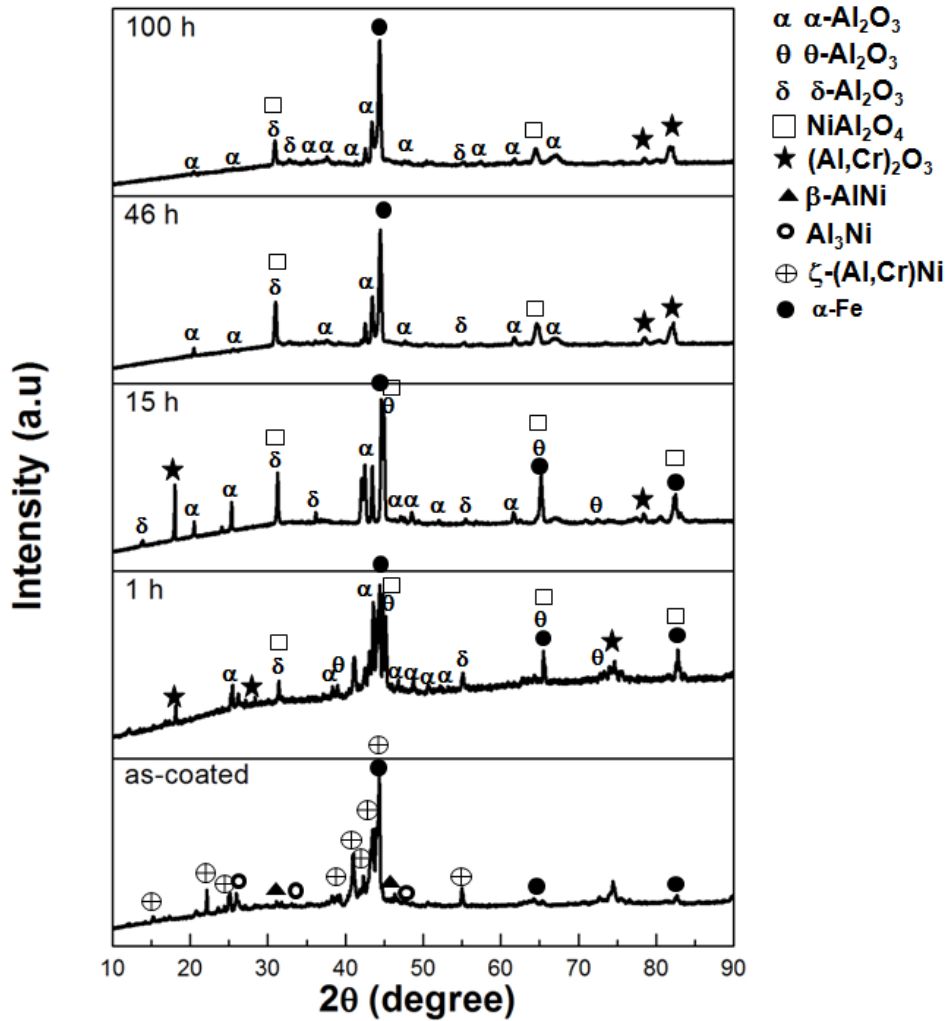


Figure 6. 1. XRD patterns of as coated and after isothermal oxidation at 800 °C in air for various times.

The result shows the phases of as-coated sample mainly consists of  $\zeta\text{-(Al,Cr)Ni}$  with hexagonal structure and a small amount of orthorhombic  $\text{Al}_3\text{Ni}$  and cubic  $\beta\text{-(Ni,Al)}$  structures. The oxide scale formed on the initial stage of 1 h and 15 h of exposure consists of several polymorphs crystalline of alumina structures such as meta-stable  $\delta$ ,  $\theta$ , and stable  $\alpha\text{-Al}_2\text{O}_3$  phases as well as spinel  $\text{NiAl}_2\text{O}_4$  and cubic  $(\text{Al,Cr})_2\text{O}_3$ . However, the oxide scale was identified to be mostly composed of  $\alpha\text{-Al}_2\text{O}_3$  and a small amount of  $\delta\text{-Al}_2\text{O}_3$ , spinel  $\text{NiAl}_2\text{O}_4$ , and cubic  $(\text{Al,Cr})_2\text{O}_3$  after 46 h and 100 h of exposure. The XRD analysis indicates that  $\theta\text{-Al}_2\text{O}_3$  only formed in the initial stage of oxidation and  $\delta\text{-Al}_2\text{O}_3$  formed from 1 h up to 100 h of oxidation.

In addition, with increasing time of oxidation, the relative intensity of peaks for  $\alpha$ - $\text{Al}_2\text{O}_3$  increased gradually, which means that more  $\alpha$ - $\text{Al}_2\text{O}_3$  was formed.

## 6.2. Cross-sectional structures in micro scale

Fig. 6. 2 shows the cross-section of as-coated and oxidized samples. The homogenous multi-layer was developed with an approximate thickness of 140  $\mu\text{m}$  on the as-coated sample (Fig. 6.2A). The point analysis of as-coated sample (Fig. 6.2a) indicates that the dark gray area on the top layer contains (73-85 at%)Al, (8-10 at%)Cr, and (5-11 at%)Ni which can be identified as hexagonal  $\zeta$ -(Al,Cr)Ni phase. A distribution of dark gray precipitates beneath the  $\zeta$ -(Al,Cr)Ni phase contains (61-73 at%)Al and (30-34 at%)Ni which is identified as orthorhombic  $\text{Al}_3\text{Ni}$  phase. Gray area on the intermediate layer of as-coated sample contains (38-47 at%)Ni and (50-57 at%)Al which is identified as cubic  $\beta$ -(Ni,Al) phase. The phases identification by point analysis is correlated with the XRD analysis shown in Fig. 6.1 from as-coated sample.

After initial stage of oxidation for 1 h (Fig. 6.2B), the internal oxide was distributed in the vicinity of surface of the coated sample. It might affect the thickness of oxide scale which was quite thick with approximately 32  $\mu\text{m}$ . In the case of 15 h, 46 h and 100 h oxidized samples (Fig. 6.2C-E), a porous oxide scale was continuously developed on the entire coated sample with a thickness of 14  $\mu\text{m}$ , 7  $\mu\text{m}$ , and 4  $\mu\text{m}$ , respectively. The magnified images obtained from the oxide scale as shown in Fig. 6.2b-e present complex and dispersed microstructure with intragranular voids and microporosity.

By point analysis in SEM, it is hardly to recognize the distribution of metastable  $\delta$ ,  $\theta$ , and stable  $\alpha$ - $\text{Al}_2\text{O}_3$  phases compare to XRD analysis. The irregularity of dark gray area which contains (41-44 at%)Al, (35-59 at%)O, and (10-11 at%)Cr was identified as  $\text{Al}_2\text{O}_3$  phase. The spinel  $\text{NiAl}_2\text{O}_4$  was formed on the bright gray area which contains (24-26at%)Ni, (52-58

at%)Al, and (10-13 at%)O. Cubic  $(Al,Cr)_2O_3$  was formed on the gray area surrounding the  $Al_2O_3$  phase which contains (40-44 at%)Al, (25-29at%)Cr, (7-8at%)Ni, and (22-25 at%)O.

The results suggest that alumina growth is controlled by grain boundary diffusion of aluminum or oxygen. In the initial stage of 1 h and 15 h (Fig. 6.2B-C), the slow growing  $\alpha$ -grains have not fully developed into a complete layer, therefore, the scale thickened through outgrowth either  $\delta$  or  $\theta$ - $Al_2O_3$  phase, and the newly formed top layer was usually porous. However, due to the presence of  $\alpha$ - $Al_2O_3$  from the initial oxidation stage, the development of the  $\alpha$ - $Al_2O_3$  was much faster after 46 h (Fig. 6.2D). Eventually, growth of the oxide scale was dominated by the  $\alpha$ - $Al_2O_3$  grain which had fully covered the surface of 100 h oxidized sample as shown in Fig. 6.2E.

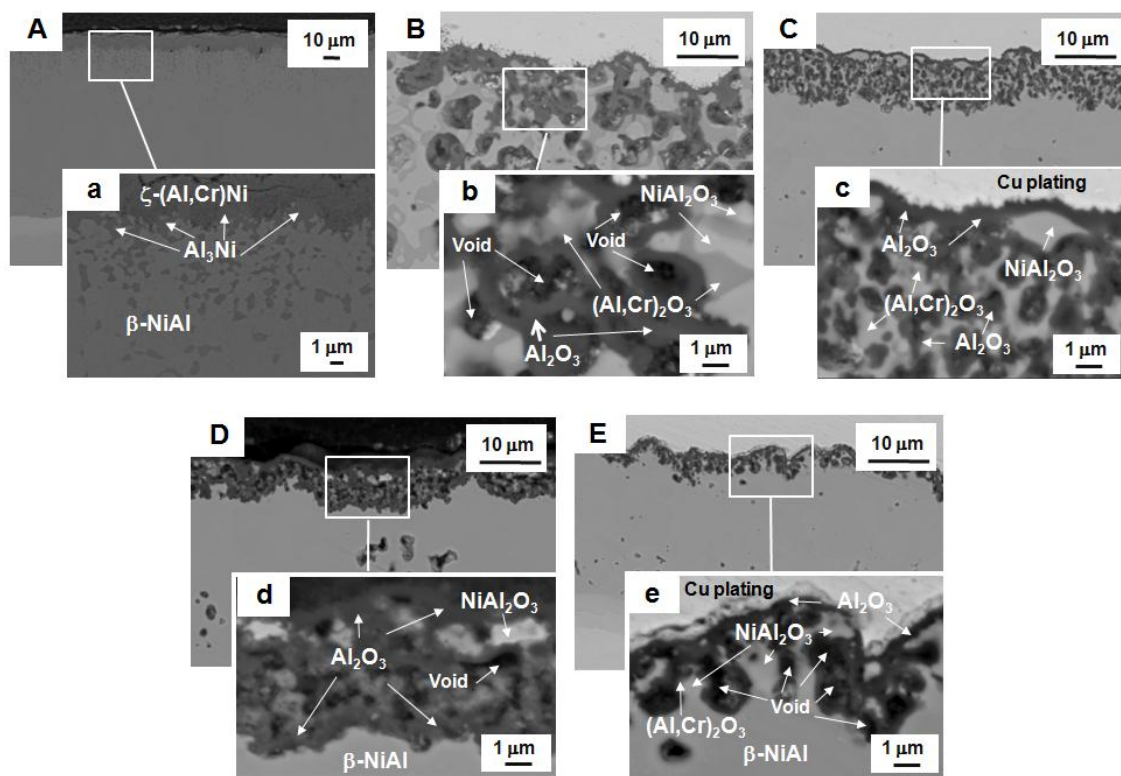


Figure 6. 2. SEM images showing cross-sectional microstructure of the samples: (A) as-coated, (B) 1 h, (C) 15 h, (D) 46 h, and (E) 100 h oxidized samples. Small letter (a-f) indicates enlarge SEM images obtained from the rectangular marked areas.

### 6.3. Cross-sectional structures in nano scale

In order to better characterize the formation from metastable to stable alumina, a cross-sectional TEM (XTEM) sample was prepared for 1 h and 100 h oxidized samples. The results are shown in Fig. 6.3.

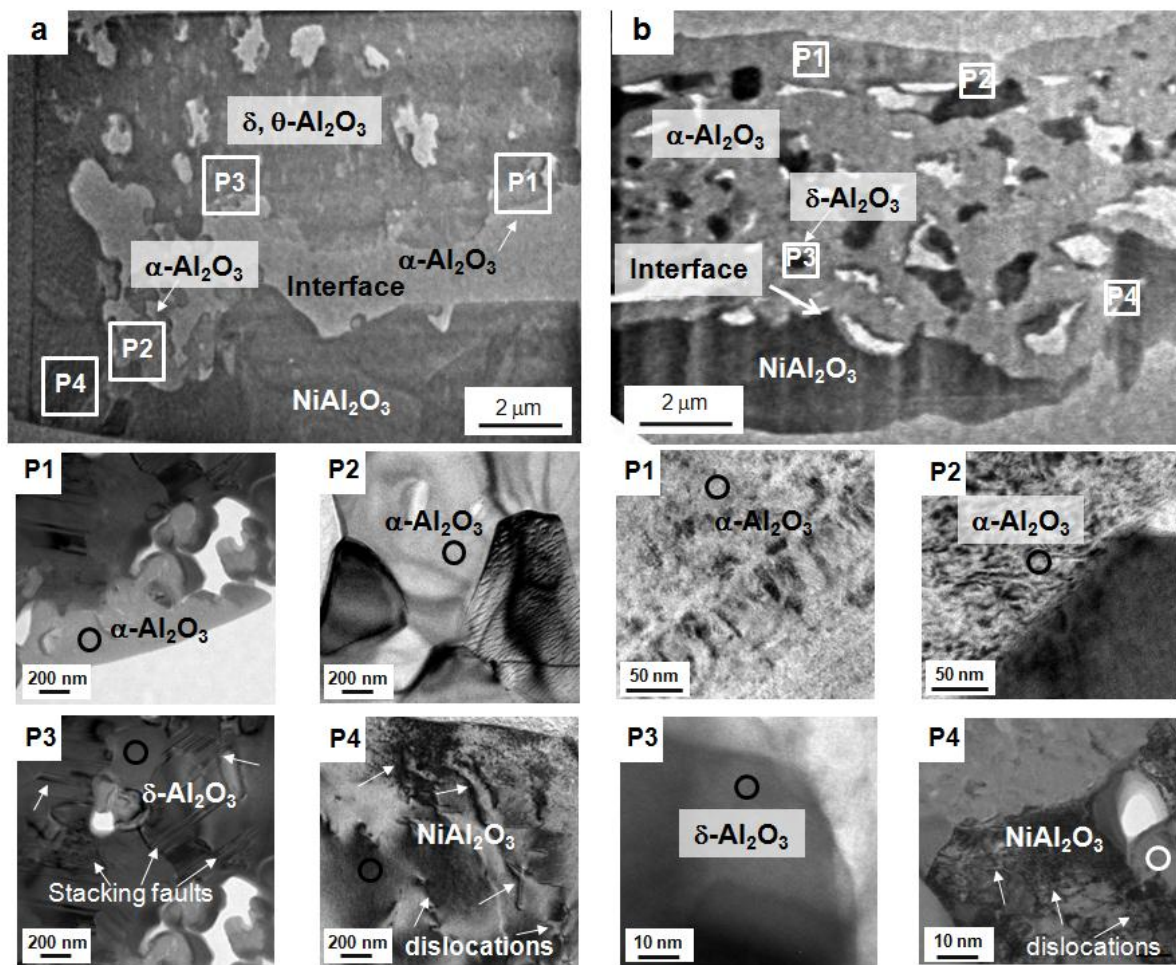


Figure 6.3. Bright field XTEM images of oxidized sample with different exposure time: (a) 1 h and (b) 100 h. A high magnification image obtained from the rectangular area (top image). (P1) and (P2) → fine grain of  $\alpha$ - $\text{Al}_2\text{O}_3$ , (P3) → area where  $\delta$ - $\text{Al}_2\text{O}_3$  is present and (P4) → large grain containing dislocations of spinel  $\text{NiAl}_2\text{O}_4$ .

It has been clearly understood that the 1 h oxidized sample has a thick oxide scale of about 32  $\mu\text{m}$ . The high magnification image observed by SEM in Fig. 6.2(b) is only focused

on the top surface of the coated layer. Therefore, XTEM sample was prepared in the area adjacent the metal/oxide interface of the 1 h oxidized sample as shown in Fig. 6.3(a). Voids of 100 nm in diameter were found randomly distributed in the oxide scale. In addition, apparent cavity was observed in this 1 h oxidized sample, probably propagated by the growth of voids found in the oxide scale. In contrast, good adherence was observed on the metal/oxide interface even though there are still a lot of voids found in the scale of 100 h oxidized sample as shown in Fig. 6.3(b). The magnified images were obtained from the rectangular area as designated by P1, P2, P3 and P4. Point analysis in TEM has been performed as indicated by circled mark. Both area of P1 and P2 in Fig. 6.3(a) and 6.3(b) have similar composition which contains (39-56at%)Al and (41-60at%)O. This composition was identified as  $\alpha$ -Al<sub>2</sub>O<sub>3</sub> phase. A very fine equiaxed grain was observed in the  $\alpha$ -Al<sub>2</sub>O<sub>3</sub> phase. Further, the area of P3 in Fig. 6.3(a) and 6.3(b) having a composition of (60-71at%)Al, (10-23at%)Cr, and (14-17at%)O was identified as  $\delta$ -Al<sub>2</sub>O<sub>3</sub> phase. In this area, planar defect such as stacking faults was clearly observed. The area of P4 depicted in Fig. 6.3(a) and 6.3(b) shows a large spherical grain in size of about 10  $\mu$ m and a high number density of dislocations which contains (50-67at%)Al, (19-20at%)Ni, and (10-23at%)O. The phase composition of these crystalline forms corresponds to spinel NiAl<sub>2</sub>O<sub>4</sub> phase.

Based on these results,  $\alpha$ -Al<sub>2</sub>O<sub>3</sub> grains were seen to nucleate at the scale/alloy interface on 1 h of oxidized sample (Fig. 6.3a). This result is similar to the previous work [90-91] which described that the nucleation of  $\alpha$ -Al<sub>2</sub>O<sub>3</sub> occurs at the scale/alloy interface during oxidation of FeCrAl system. Subsequently, the nuclei of the metastable  $\delta$  and  $\theta$ -Al<sub>2</sub>O<sub>3</sub> phases are forming above the  $\alpha$ -Al<sub>2</sub>O<sub>3</sub> phase. In the case of the 100 h oxidized sample, the presence of the  $\theta$ -Al<sub>2</sub>O<sub>3</sub> phase was not identified. It is possible that this phase forms only during the initial stage of the oxidation as previously revealed by XRD analysis in Fig.6.1. The  $\delta$ -Al<sub>2</sub>O<sub>3</sub> phase was still present on the oxide scale after 100 h of oxidation, however, small peaks of  $\delta$ -Al<sub>2</sub>O<sub>3</sub> phase in

XRD analysis indicated the small amount of this phase in the oxide scale. The transformation of metastable to stable  $\alpha$ -Al<sub>2</sub>O<sub>3</sub> usually requires a relatively longer time particularly at temperatures below 900 °C [92]. The existence of spinel NiAl<sub>2</sub>O<sub>4</sub> and cubic (Al,Cr)<sub>2</sub>O<sub>3</sub> phases in the oxidized sample was likely surrounded by the metastable alumina grain boundary.

#### 6.4. Properties of polymorph alumina

This section describes briefly the complexity of alumina crystalline phases and reviews the properties of the three phases which are encountered in this work. Alumina (Al<sub>2</sub>O<sub>3</sub>) exists in many metastable polymorphs beside the thermodynamically stable  $\alpha$ -Al<sub>2</sub>O<sub>3</sub> (corundum form). The metastable Al<sub>2</sub>O<sub>3</sub> structures can be divided into two broad categories: a *face-centered cubic (fcc)* or ( $\cdots$ ABCABC $\cdots$  stacking sequence) and a *hexagonal close-packed (hcp)* or ( $\cdots$ ABAB $\cdots$  stacking sequence) arrangement of oxygen anions. It is the distribution of cations within each subgroup that results in the different polymorphs. The Al<sub>2</sub>O<sub>3</sub> structures based on *fcc* packing of oxygen include  $\gamma$ ,  $\eta$  (cubic),  $\theta$  (monoclinic), and  $\delta$  (either tetragonal or orthorhombic), whereas the Al<sub>2</sub>O<sub>3</sub> structures based on *hcp* packing are represented by the  $\alpha$  (trigonal),  $\kappa$  (orthorhombic), and  $\chi$  (hexagonal) phases. A brief summary on the structures and properties of common alumina polymorphs is presented in Table 6.1.

Table 6.1. Structure and properties of alumina polymorphs [93].

Phases	Structure (arrangement of oxygen)	Space group
$\alpha$	hcp	<i>R3c</i>
$\gamma$	fcc	<i>Fd3m</i>
$\kappa$	hcp	<i>Pna2</i>
$\delta$	fcc	<i>P4m2</i>
$\theta$	fcc	<i>C2/m</i>

##### 6.4.1 Corundum $\alpha$ -Al<sub>2</sub>O<sub>3</sub>

The  $\alpha$  structure is thermodynamically stable at all temperatures up to its melting point at 2051 °C [84]. The corundum structure belongs to space group  $R3c$  and rhombohedral with two formula units (10 atoms) in the primitive unit cell. However, a more often used unit cell is the hexagonal representation containing six formula units [93]. The crystal structure of  $\alpha$ - $\text{Al}_2\text{O}_3$  is the corundum structure which consists of a hexagonal close packed (*hcp*) O anion arrangement with Al cations filling up 2/3 of the central octahedral sites (Fig. 6.4) with the lattice parameters  $a = 0.476$  nm and  $c = 1.299$  nm.

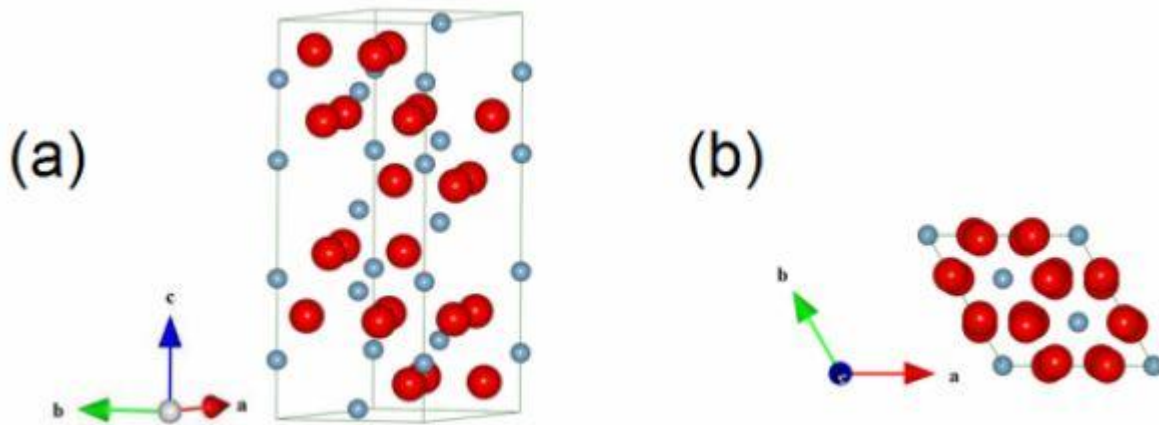


Figure 6.4. Hexagonal unit cell of  $\alpha$ - $\text{Al}_2\text{O}_3$  with (a) side view and (b) (0001) projection [93].

#### 6.4.2 Tetragonal $\delta$ - $\text{Al}_2\text{O}_3$

$\delta$ - $\text{Al}_2\text{O}_3$  belongs to space group  $P4m2$  having a tetragonally deformed spinel lattice with cell dimensions of  $a = 0.796$  nm and  $c = 0.235$  nm. This unit cell contains 80 ions with 4 cation vacancies randomly distributed over octahedrally coordinated sites.

#### 6.4.3 Monoclinic $\theta$ - $\text{Al}_2\text{O}_3$

The  $\theta$  phase of alumina is metastable and transforms into the  $\alpha$  phase at about 1050 °C [84]. The  $\theta$  structure is based on an *fcc* oxygen lattice. Within this oxygen framework, half the

aluminum ions occupy octahedral interstitial sites and half occupy tetrahedral (with four oxygen neighbors) sites, as shown in Fig. 6.5. This is also in contrast to  $\alpha$  phase. The oxygen ions have three different possible surroundings, each of which is occupied by 1/3 of the oxygen ions. Two of these oxygen sites have three aluminum nearest neighbors and the third has four. The structure is monoclinic, belonging to space group  $C2/m$ , and the unit cell contains four formula units (20 atoms) with lattice parameters  $a = 0.56$  nm  $b = 0.29$  nm,  $c = 1.18$  nm and  $\beta = 103.7^\circ$ .

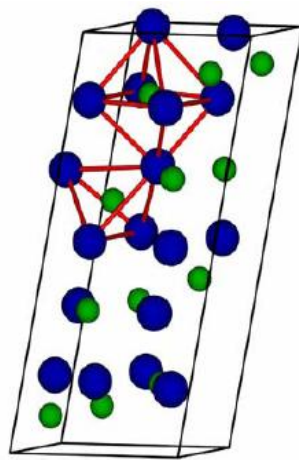


Figure 6.5. The  $\theta$ - $\text{Al}_2\text{O}_3$  monoclinic unit cell. Large sphere represent O atom and small Al. Example of tetra- and octahedral Al position are indicated [93].

As previously mentioned, there is uncertainty in the existence of the  $\delta$ - $\text{Al}_2\text{O}_3$  phase because it is very difficult to distinguish from  $\theta$ - $\text{Al}_2\text{O}_3$  phase. Therefore, the identification of the phases, especially the polymorphs crystalline structures in the coated layer, is very important to solve this problem. The phase identification using selected area electron diffraction (SAED) method was carried out in this study.

## 6.5. Polymorphic crystal structures of alumina

Phase formed in the coated layer was characterized by the SAED patterns. Indexing SAED pattern can be performed by measuring the spacing between a transmitted spot and a reflected spot. In this case the distance was measured between the two closest spots to the origin. Details of the measurement process of the diffraction pattern will be described briefly:

- The distance,  $r_{hkl}$ , on the pattern between the spot  $hkl$  and the spot 000 is related to the interplanar spacing between the  $hkl$  planes of atoms,  $d_{hkl}$ , by the following equation [93]:

$$r_{hkl} = \frac{\lambda L}{d_{hkl}} \quad (6-1)$$

Where,  $L$  is the distance between the sample and the film/screen.

We can therefore say that the diffraction pattern is a projection of the reciprocal lattice with projection factor  $lL$ , because reciprocal lattice vectors have length  $1/d_{hkl}$ .

- Since the diffraction pattern is a projection of the reciprocal lattice, the angle between the lines joining spots  $h_1k_1l_1$  and  $h_2k_2l_2$  to spot 000 is the same as the angle between the reciprocal lattice vectors  $[h_1k_1l_1]$  and  $[h_2k_2l_2]$ . This angle is  $\phi$  in the Fig. 6.6.

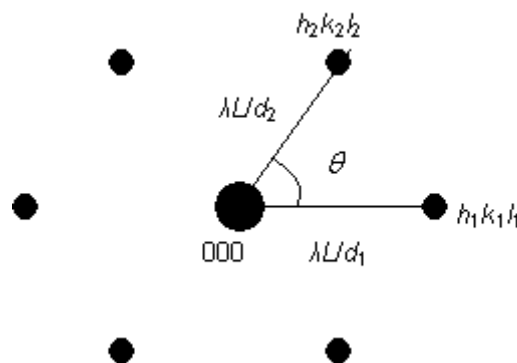


Figure 6.6. Schematic illustration for indexing the electron diffraction pattern.

Using these two relations between the diffraction pattern and the reciprocal lattice, we are now able to index the electron diffraction pattern from a specimen of a crystal structure. To verify the measurement of the  $hkl$  planes and  $\phi$  angle, the following equations need to be brought into play:

$$\begin{aligned}
 \text{Cubic:} \quad \cos \phi &= \frac{h_1 h_2 + k_1 k_2 + l_1 l_2}{\left( (h_1^2 + k_1^2 + l_1^2)(h_2^2 + k_2^2 + l_2^2) \right)^{1/2}} \\
 \text{Tetragonal:} \quad \cos \phi &= \frac{\frac{h_1 h_2 + k_1 k_2}{a^2} + \frac{l_1 l_2}{c^2}}{\left( \left( \frac{h_1^2 + k_1^2}{a^2} + \frac{l_1^2}{c^2} \right) \left( \frac{h_2^2 + k_2^2}{a^2} + \frac{l_2^2}{c^2} \right) \right)^{1/2}} \\
 \text{Hexagonal:} \quad \cos \phi &= \frac{h_1 h_2 + k_1 k_2 + \frac{1}{2}(h_1 k_2 + h_2 k_1) + \frac{3a^2 l_1 l_2}{4c^2}}{\left( \left( h_1^2 + k_1^2 + h_1 k_1 + \frac{3a^2 l_1^2}{4c^2} \right) \left( h_2^2 + k_2^2 + h_2 k_2 + \frac{3a^2 l_2^2}{4c^2} \right) \right)^{1/2}} \\
 \text{Monoclinic:} \quad \cos \phi &= \frac{d_1 d_2}{\sin^2 \beta} \left[ \frac{h_1 h_2}{a^2} + \frac{k_1 k_2 \sin^2 \beta}{b^2} + \frac{l_1 l_2}{c^2} - \frac{(l_1 h_2 + l_2 h_1) \cos \beta}{ac} \right]
 \end{aligned}$$

*Rhombohedral:*

$$\cos \phi = \frac{a^4 d_1 d_2}{v^2} [\sin^2 \alpha (h_1 h_2 + k_1 k_2 + l_1 l_2) + (\cos^2 \alpha - \cos \alpha) (k_1 l_2 + k_2 l_1 + l_1 h_2 + l_2 h_1 + h_1 k_2 + h_2 k_1)]$$

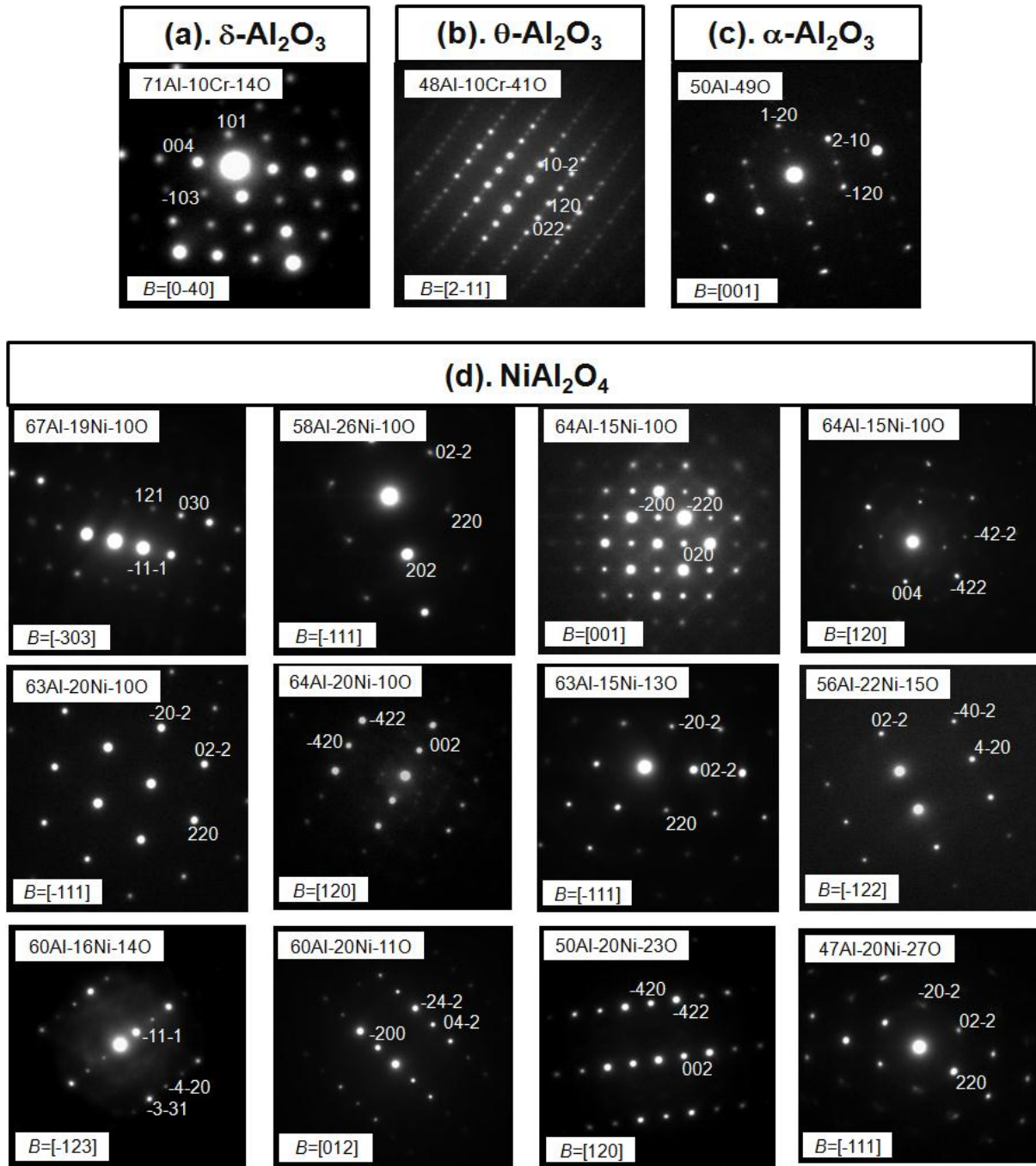
- Lattice constant of the crystal can be determined by using these equations:

$$\begin{aligned}
 \text{Cubic:} \quad \frac{1}{d^2} &= \frac{h^2 + k^2 + l^2}{a^2} \\
 \text{Tetragonal:} \quad \frac{1}{d^2} &= \frac{h^2 + k^2}{a^2} + \frac{l^2}{c^2} \\
 \text{Hexagonal:} \quad \frac{1}{d^2} &= \frac{4}{3} \frac{h^2 + hk + k^2}{a^2} + \frac{l^2}{c^2}
 \end{aligned}$$

$$\text{Monoclinic: } \frac{1}{d^2} = \frac{1}{\sin^2\beta} \left( \frac{h^2}{a^2} + \frac{k^2 \sin^2\beta}{b^2} + \frac{l^2}{c^2} - \frac{2hl \cos\beta}{ac} \right)$$

$$\text{Rhombohedral: } \frac{1}{d^2} = \frac{(h^2 + k^2 + l^2)\sin^2\alpha + 2(hk + kl + hl)(\cos^2\alpha - \cos\alpha)}{a^2(1 - 3\cos^2\alpha + 2\cos^3\alpha)}$$

SAED obtained in the coated layer is divided into three groups which is transition  $\text{Al}_2\text{O}_3$ , spinel  $\text{NiAl}_2\text{O}_4$  and cubic  $(\text{Al,Cr})_2\text{O}_3$  phases as shown in Fig. 6.7.



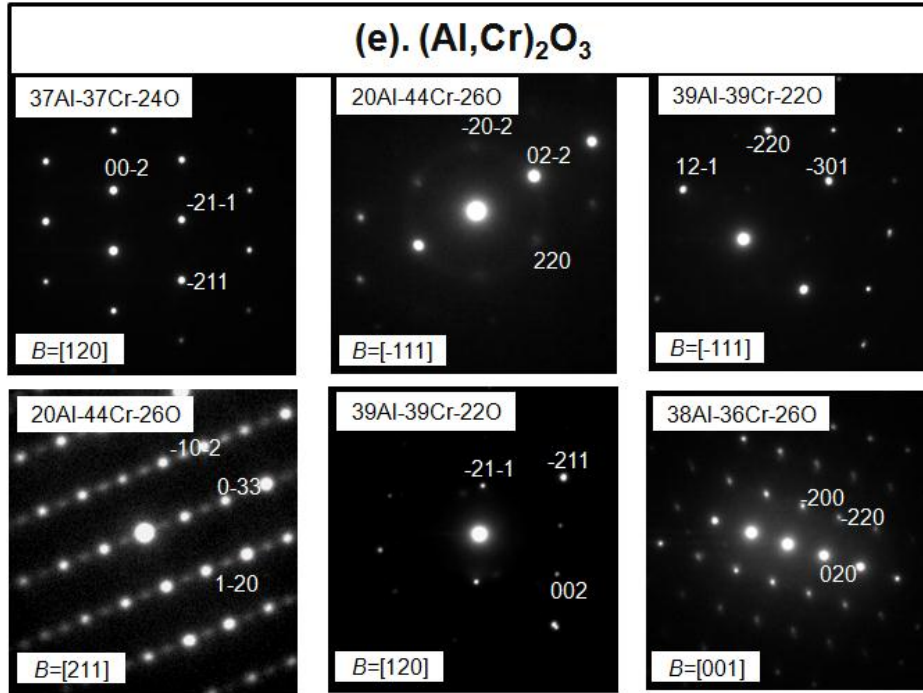


Figure 6.7. SAED patterns showing several polymorphic crystal structures of alumina: (a).  $\delta$ - $\text{Al}_2\text{O}_3$ , (b).  $\theta$ - $\text{Al}_2\text{O}_3$ , (c).  $\alpha$ - $\text{Al}_2\text{O}_3$ , (d). spinel  $\text{NiAl}_2\text{O}_4$ , and (e). cubic  $(\text{Al,Cr})_2\text{O}_3$ . Symbol B in the SAED pattern represents the incident electron beam direction of the diffraction pattern.

By using the diffraction pattern, the crystal structure and lattice parameter can be determined as summarized in Table 6.2.

Table 6.2. Lattice parameter determined from the coated layers.

Designation	Structure	Lattice Parameter (nm)		
		<i>a</i>	<i>b</i>	<i>c</i>
$\alpha$ - $\text{Al}_2\text{O}_3$	Rhombohedral	0.48		1.29
$\theta$ - $\text{Al}_2\text{O}_3$	Monoclinic	0.56	0.29	1.19
$\delta$ - $\text{Al}_2\text{O}_3$	Tetragonal	0.79		2.35
$\text{NiAl}_2\text{O}_4$	Cubic	0.55 – 0.81		
$(\text{Al,Cr})_2\text{O}_3$	Cubic	0.41 – 0.60		

The results show that the meta-stable alumina like  $\delta$ ,  $\theta$  and stable  $\alpha$ - $\text{Al}_2\text{O}_3$  phases were identified in the coated layer. A comparison of lattice parameter by the experimental and reference results was examined in order to prove the precision of the lattice parameter measurement in the present study. The phase that has been analyzed in Fig. 6.7(a) was determined to be  $\delta$ - $\text{Al}_2\text{O}_3$  with tetragonal structure having a lattice parameter of  $a = 0.79$  nm and  $c = 2.35$  nm [95]. Phase composition in Fig. 6.7(b) corresponds to  $\theta$ - $\text{Al}_2\text{O}_3$ . Such phase has monoclinic symmetry (space group  $C2/m$ ) which is a structural isomorphs of  $\beta$ - $\text{Ga}_2\text{O}_3$  with the lattice parameters is  $a = 0.56$  nm  $b = 0.29$  nm,  $c = 1.19$  nm and  $\beta = 103.7^\circ$  [84]. Rhombohedral  $\alpha$ -alumina with lattice parameters of  $a = 0.48$  nm and  $c = 1.29$  nm [94-96] is the most thermodynamically stable phase of alumina. The SAED pattern is shown in Fig. 6.7(c)

For the spinel  $\text{NiAl}_2\text{O}_4$  and cubic  $(\text{Al,Cr})_2\text{O}_3$  phases, the lattice parameter measurement is relatively changed due to the existence of other elements such as cobalt and nickel. By calculating the lattice parameter from several SAED patterns obtained in the different area of XTEM samples, the changes are illustrated in Fig. 6.8.

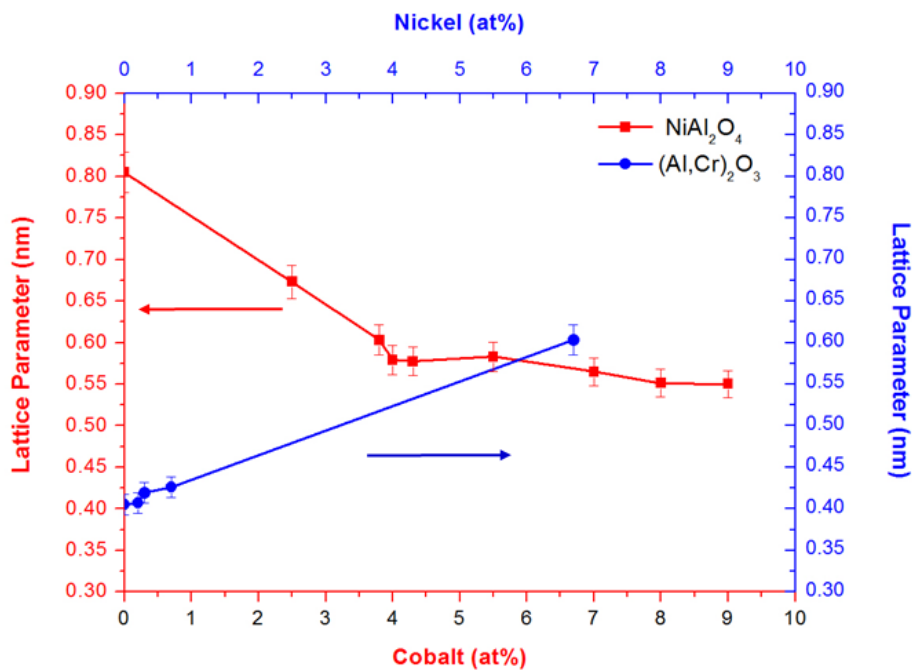


Figure 6.8. Measured lattice parameter of spinel  $\text{NiAl}_2\text{O}_4$  (red line) and cubic  $(\text{Al,Cr})_2\text{O}_3$  (blue line) phases obtained from the coated sample oxidized at  $800^\circ\text{C}$  for up to 100 h.

Both spinel  $\text{NiAl}_2\text{O}_4$  and cubic  $(\text{Al,Cr})_2\text{O}_3$  phases were established as *face center cubic* (*fcc*) structure. Unmixed spinel  $\text{NiAl}_2\text{O}_4$  or without Co content has a lattice parameter of  $a = 0.80$  nm [98]. The results show that the lattice parameter decreases with increasing cobalt content until its content less than 4 at% and it has a tendency to be stable up to 9 at% Co. At this point, the lattice parameter was determined to be  $a = 0.55$  nm. In contrast, the lattice parameter of cubic  $(\text{Al,Cr})_2\text{O}_3$  phase identified in the coated layer appeared to have a linear trend. As described in Ref. [99], the lattice parameter of cubic  $(\text{Al,Cr})_2\text{O}_3$  was 0.41 nm and it increases with increasing of nickel content as plotted in Fig.6.8 (blue line). Therefore, when the nickel content reaches 7 at%, the lattice parameter found to be 0.60 nm. The changes can also be caused by the differences in Ni, Co, Fe, Al and Cr atomic radii: Ni (0.162 nm) < Co (0.167 nm) < Fe (0.172 nm) < Al (0.182 nm) < Cr (0.185 nm). The lattice parameter of the spinel  $\text{NiAl}_2\text{O}_4$  with Co content phase is smaller than that of pure  $\text{NiAl}_2\text{O}_4$  and the lattice parameter of the cubic  $(\text{Al,Cr})_2\text{O}_3$  phase with Ni content is larger than that of pure  $(\text{Al,Cr})_2\text{O}_3$ .

## 6.6. Composition of oxide grown obtained on Ni-Cr-Al system at 800 °C

Table 6.3 summarizes the composition of oxide species evaluated by the combination of EDS in SEM and TEM analysis. By using this compositional range, oxide morphology map for ternary Ni-Cr-Al evaluated at 800 °C can be plotted as shown in Fig 6.9. The dotted line represents three primary oxidation region observed by Nicholls *et al.* [86] at temperature over 1000 °C. It is a well-known sequence of alumina phase transformation:  $\gamma \rightarrow \delta \rightarrow \theta \rightarrow \alpha$ , achieved at various conditions [95-96]. In line with the results shown in Fig.6.9, at high to low concentration of Al, a sequence of alumina phase transformation in this study also has a good agreement with the reference and the results followed  $\delta \rightarrow \theta \rightarrow \alpha\text{-Al}_2\text{O}_3$ . No  $\gamma\text{-Al}_2\text{O}_3$  phase was formed on the coated sample based on the diffraction pattern analysis.  $\gamma$  and  $\delta\text{-Al}_2\text{O}_3$  phases have similar tetragonal structures, however, the lattice parameter of those phases is

different. The lattice parameter of  $\gamma$ - $\text{Al}_2\text{O}_3$  phase is  $a = 0.795$  nm and  $c = 0.779$  nm. Thus, the measured lattice parameter of  $a = 0.79$  nm and  $c = 2.35$  nm has clearly identified to be  $\delta$ - $\text{Al}_2\text{O}_3$  phase. Moreover, at the region of high concentration of Al, Ni and Cr, the spinel and cubic structure were found.

Table 6.3. Compositions obtained in the coated layer corresponding to oxide species.

Oxides	Composition (at%)				
	Ni	Co	Cr	Al	O
$\alpha$ - $\text{Al}_2\text{O}_3$				41 - 56	40 - 56
$\theta$ - $\text{Al}_2\text{O}_3$			10 - 15	48 - 57	35 - 41
$\delta$ - $\text{Al}_2\text{O}_3$	2 - 4		6 - 23	60 - 74	10 - 19
$\text{NiAl}_2\text{O}_4$	14 - 26	2 - 9		50 - 68	10 - 33
$(\text{Al,Cr})_2\text{O}_3$	0.2 - 8		25 - 36	20 - 44	22 - 30

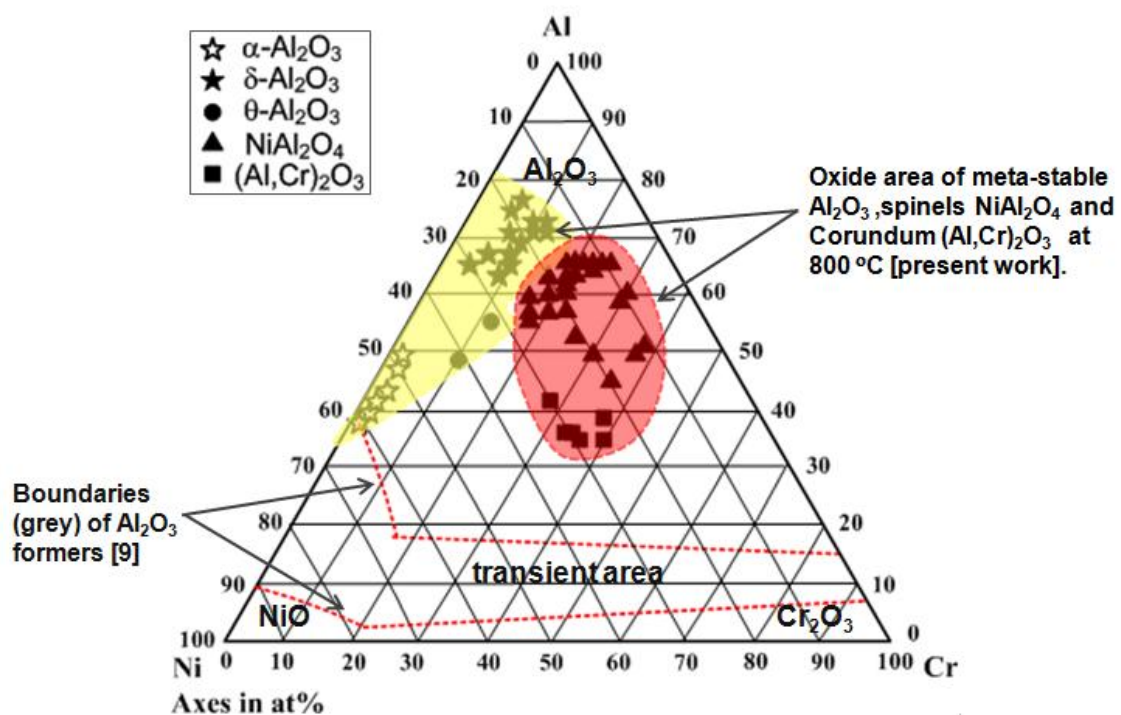


Figure 6.9. Approximation of oxide morphology map for ternary Ni-Cr-Al based on the established phases in the NiCo-Cr-Al coatings after oxidation at 800 °C for 100 h. Boundaries of alumina formers are plotted as characterized by Nicholls *et al.* [86].

These data were compared to the results with similar samples of NiCoCrAl coatings deposited by magnetron sputtering [89], in order to achieve a better knowledge of oxidation behavior. The results, presented by Serrafon *et al.* in Fig. 6.10, showed that the oxide domain for metastable alumina formation is likely to be similar. However, the oxide domain changed significantly for spinel  $\text{NiAl}_2\text{O}_4$  and cubic  $(\text{Al,Cr})_2\text{O}_3$  phases with the reduction of temperature from  $950^\circ$  to  $800^\circ\text{C}$ .

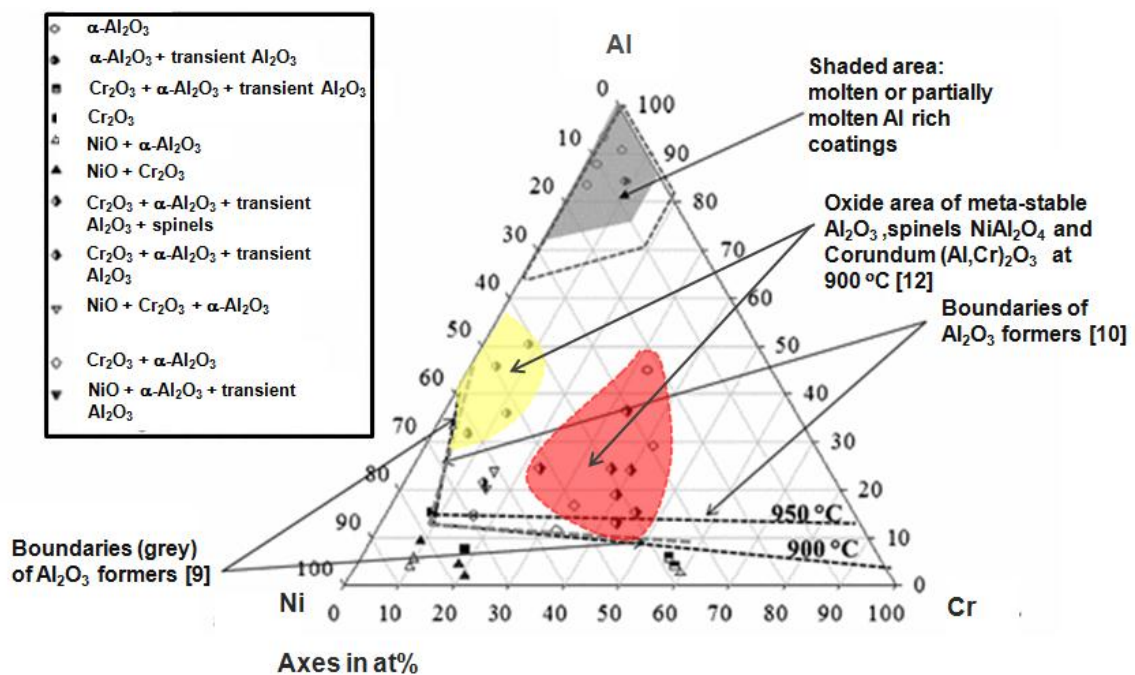


Figure 6.10. Oxide composition grown on Ni–Cr–Al coatings after oxidation at  $900^\circ\text{C}$  for 500 h presented by Serrafon *et al.* [89]. Boundaries of alumina formers are compared to those obtained at  $900^\circ\text{C}$  and  $950^\circ\text{C}$  [87] and by Nicholls *et al.* [86].

At  $950^\circ\text{C}$  the spinel and cubic structure formed from the transient zone plotted by Nicholls *et al.* [86] to above 50 at% Al. At  $800^\circ\text{C}$  the spinel and cubic structures formed from 30 – 70 at% Al as well as a high concentration of Ni and Cr. There are some reasons for the distinctions: (1) a different coating process affects the composition of as-coated sample before oxidation test, (2) the lowering oxidation temperature considerably affects the formation of

mixed oxide like spinel and cubic structure that contains a crystal defect like stacking faults and dislocations (Fig. 6.3), and (3) the lattice parameter changes due to the impurity of other element like cobalt and nickel as previously described in this study (Fig. 6.8). It is worth noting that the result in present study is the first result which will contribute to the oxide ternary map of Ni–Cr–Al at 800 °C.

## 6.7. Conclusions

This paper describes the results of micro-nano analysis for metastable  $\text{Al}_2\text{O}_3$  scale formed on NiCoCrAl coated layer during isothermal oxidation. Several important features are revealed from the experimental results:

1. The NiCoCrAl coatings show a good oxidation resistance even when complex oxide scales formed due to its good adhesion with the coating. Similarly, the coating was found to be successful in maintaining its integrity with the carbon steel substrate.
2. The oxide scale formed on the initial stage of 1 h and 15 h of exposure consists of several polymorphs crystalline of alumina structure such as meta-stable  $\delta$ ,  $\theta$ , and stable  $\alpha$ - $\text{Al}_2\text{O}_3$  phases. However, the oxide scale of 100 h sample was identified to be mostly composed of  $\alpha$ - $\text{Al}_2\text{O}_3$  and a small amount of  $\delta$ - $\text{Al}_2\text{O}_3$ .
3. The existence of spinel  $\text{NiAl}_2\text{O}_4$  and cubic  $(\text{Al,Cr})_2\text{O}_3$  phases from initial of oxidation stage up to 100 h of exposure in the oxidized sample is likely surrounded by the meta-stable alumina grain boundary.
4. Voids formed in the scale may also arise during the transformation of meta-stable  $\delta$ - $\theta$  to stable  $\alpha$ - $\text{Al}_2\text{O}_3$ .
5. The  $\delta$ - $\text{Al}_2\text{O}_3$  and  $\theta$ - $\text{Al}_2\text{O}_3$  phases are successfully identified in the oxide scale by SAED pattern.
6. Lattice parameter of meta-stable alumina is matched with the references. However the

lattice parameter changes for spinel and cubic structure due to the existence of either crystal defects or Co/Ni content.

7. A sequence of alumina phase transformation formed on the NiCoCrAl coated layer could be assumed to follow diffusion pathway plotted on the oxide ternary map diagram at 800°C which is  $\delta \rightarrow \theta \rightarrow \alpha\text{-Al}_2\text{O}_3$ .

## Chapter 7

### Non – Destructive Characterization of Corroded Carbon Steel

This chapter presents non-destructive characterization to evaluate internal corrosion in simulated piping system by applying neutron radiography and tomography (NRT). Details of experimental simulation were presented in chapter 3.

The problems of corrosion and deposit are crucial issues in the pipelines of the geothermal power plant industries. The geothermal fluid, water and steam, and their mixtures contain many kinds of corrosive chemicals such as chlorides, sulfates, hydrogen sulfide, etc. Gaseous HCl is often a primary cause of well-casing and pipe-system corrosion in geothermal systems [100-104].

Carbon steels are commonly used as piping systems due to higher temperature limit than fiberglass reinforced plastic and asbestos cement for geothermal power plant. Although carbon steels can develop a passive layer of iron oxide, ingress of aggressive environments such as chlorides can lead to breakdown of the passive layer accelerating the corrosion of unprotected surface ultimately leading to the formation of hydrated iron oxide (rust):  $\text{Fe}_2\text{O}_3 \cdot \text{H}_2\text{O}$  [105-109]. Therefore, geothermal fluid and gas pipeline made of carbon steels can be susceptible to internal localized corrosion.

The condition of critical components in these industries can be monitored by the proper use of non-destructive testing (NDT) methods. Neutron radiography and tomography (NRT) is an important NDT technique and it is the only radiography technique that is able to investigate internal structure of material [110-111]. However, this technique is far less used in this field. NR is quite sensitive in detection of hydrogenous materials such as water, water-logged ceramics, and organic materials such as wood or water-logged wood, plants, seeds, food

remnants, leather, textiles, paper, fragrances, tar, epoxy resins, etc. This enables to uncover fine structures inside thick metal layers which are not accessible for X-ray radiography.

### 7.1. Scattering interactions

Neutron penetrates almost all metals used for construction purpose with little loss in intensity. In contrast they are considerably attenuated in passing through materials containing hydrogen, such as water, oil or several types of synthetics. On the other hand in the case of X-ray radiation, this dependence may be characterized by more or less continuously increasing curves. This means that the radiation is absorbed to a great extent by heavy elements whereas it penetrates light material such as hydrogen without significant loss in intensity. Fig. 7.1 shows beams of X-rays and neutrons interact with material by different mechanisms described as follows:

- **X rays (blue) and electron beams (yellow)** → both interact with electrons in the material; with X-rays the interaction is electromagnetic, whereas with an electron beam it is electrostatic. Both of these interactions are strong, and neither type of beam penetrates matter very deeply.
- **Neutrons (red)** → interact with atomic nuclei via the very short-range strong nuclear force and thus penetrate matter much more deeply than x rays or electrons. If there are unpaired electrons in the material, neutrons may also interact by a second mechanism: a dipole-dipole interaction between the magnetic moment of the neutron and the magnetic moment of the unpaired electron.

Fig.7.2 shows the different contrast of observing elements related to their atomic under neutron and X-ray beams. Some of the lightest elements ( $H_2O$  and  $O_2$ ) darker in contrast than the heavy elements, such as Cr, Nb, Zn, Mo, etc. This become of particular interest to

investigate the corrosion products which have hydrogen in their composition. Therefore, the utilization of NRT is more suitable for visualizing the internal structure of the pipeline system when exposed to the corrosive environment.

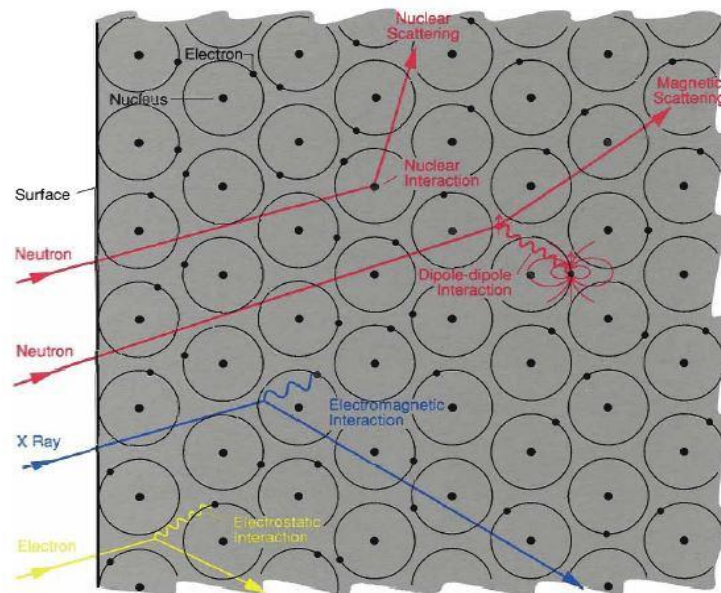


Figure 7.1. Different mechanism of scattering interaction of X-ray and neutron beams [50].

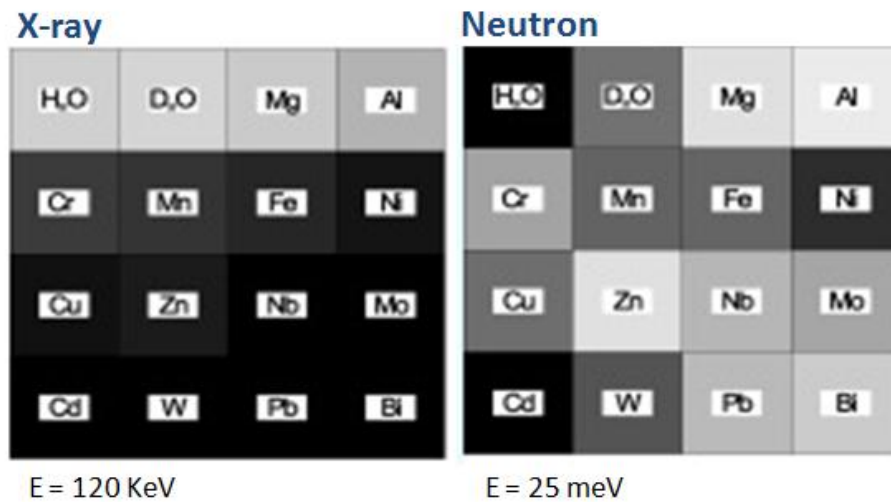


Figure 7.2. Different contrast of observing element under X-ray and neutron beams according to their thermal conductivity [66].

## 7.2. Outer Corrosion

Fig.7.3 shows photographs of the piping components after acid vapor corrosion test using 37% HCl for 48 h. The effect of different materials and coated pipe on the corrosion resistance was obviously observed. On the other hand, the different distance/position of piping component from the acid source was also one of the factors that might the dissimilar corrosion behavior.

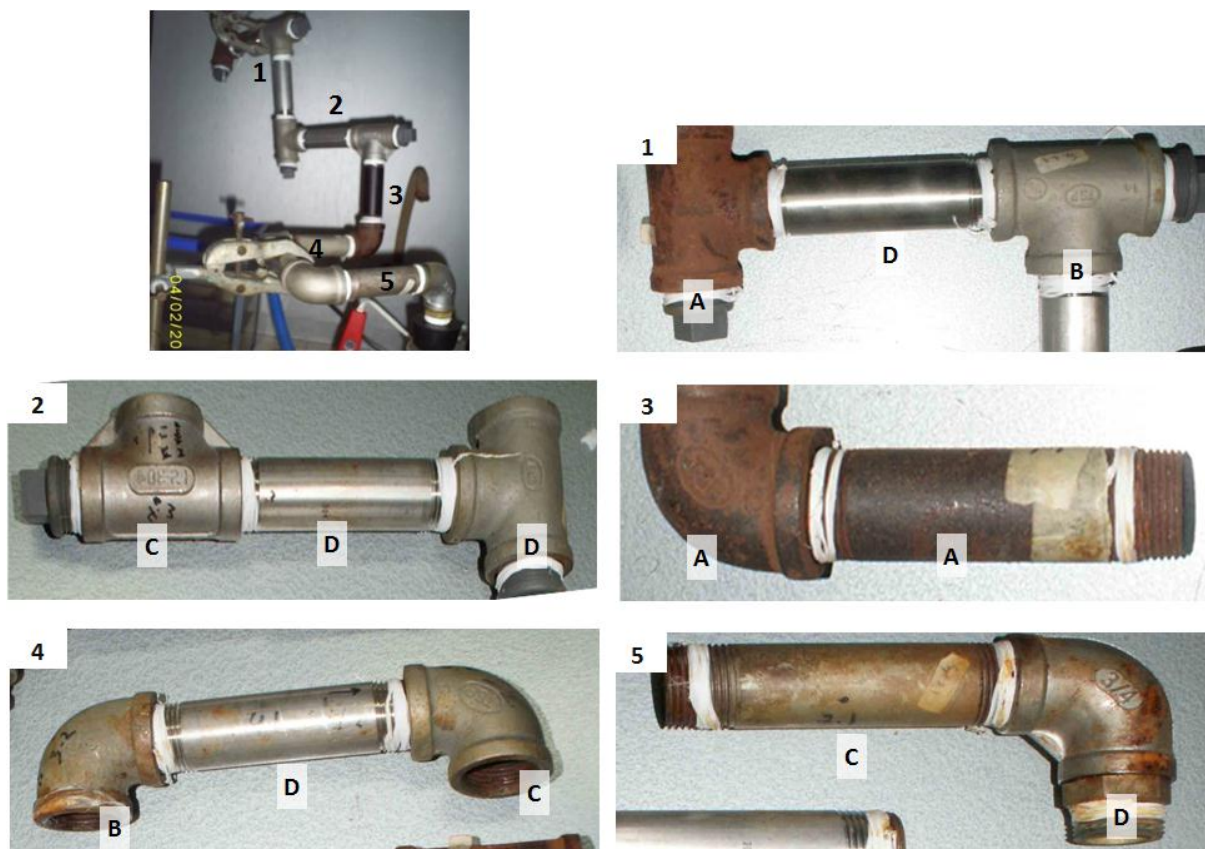


Figure 7.3. Photographs showing the piping components after acid vapor corrosion test using 37% HCl for 48 h. Left top image showing the piping construction. (1-5) designating the location of the pipe components. (A-D) index designating the pipe materials described in Table 3.

By visual inspection, the corrosion attacked by  $\text{Cl}^-$  gas could also be observed at the outer surface of the pipe. It revealed that pipe code A (uncoated ST37) was severely corroded

at both position 1 and 3. The pipe code B (NiCo coated ST37) was slightly corroded at position 1 and 4. In the case of pipe code C (NiCo coated + heated at 800 °C for 2 h of ST37) showed different corrosion behavior. Tee shape of pipe C at position 2 was less corroded than elbow and straight shapes at position 4 and 5, respectively. The comparison could be made for straight pipe with code D (uncoated 304 SS) at different position of 1, 2 and 4. It revealed the effect of position from the acid source might cause the pipe D at position 5 was much more corroded than those at position 1 and 2. From these results, it noticed that pipe A of ST37 or low carbon steel without coating was extensively damaged at all positions in this simulated corrosion test due to vapor come from the chloride acid is very corrosive to carbon steel. NiCo coated for pipe B and C could protect the ST37 substrate for aggressive corrosion at location far from the HCl source. At position 5 where close to acid inlet is very critical. It speculated that flow of vapor chloride acid is high and increased corrosion. The corrosion products at the inner surface of the pipe will further illustrated by neutron radiography and tomography (NRT).

### **7.3. Internal Corrosion (rust and blister in 2D and 3D NRT images)**

Neutron radiography and tomography (NRT) was successfully performed on piping corroded samples. Fig. 7.4 shows a 2D neutron transmission radiograph of the pipes at position 1. The different contrast showing attachment of corroded metal or rust was observed in Tee shape of pipe A (uncoated ST37) as dark area. For Tee shape of pipe B which coated by NiCo, the corrosion product was not observed due to the formation of protective scale and it speculated that NiO protective scale could be formed on the pipe wall. It was clarified that the Tee shape of pipe A was subjected to the severe corrosion as compared with Tee shape of pipe B. Different contrast at left and right hand side of straight pipe was also observed. The reason is probably caused by high acid vapor pressure at the bottom of straight pipe during corrosion test. The high contrast of the surface corroded area is the result of the presence of hydrogen,

which has a high neutron attenuation coefficient, in the chemical composition of corrosion products.

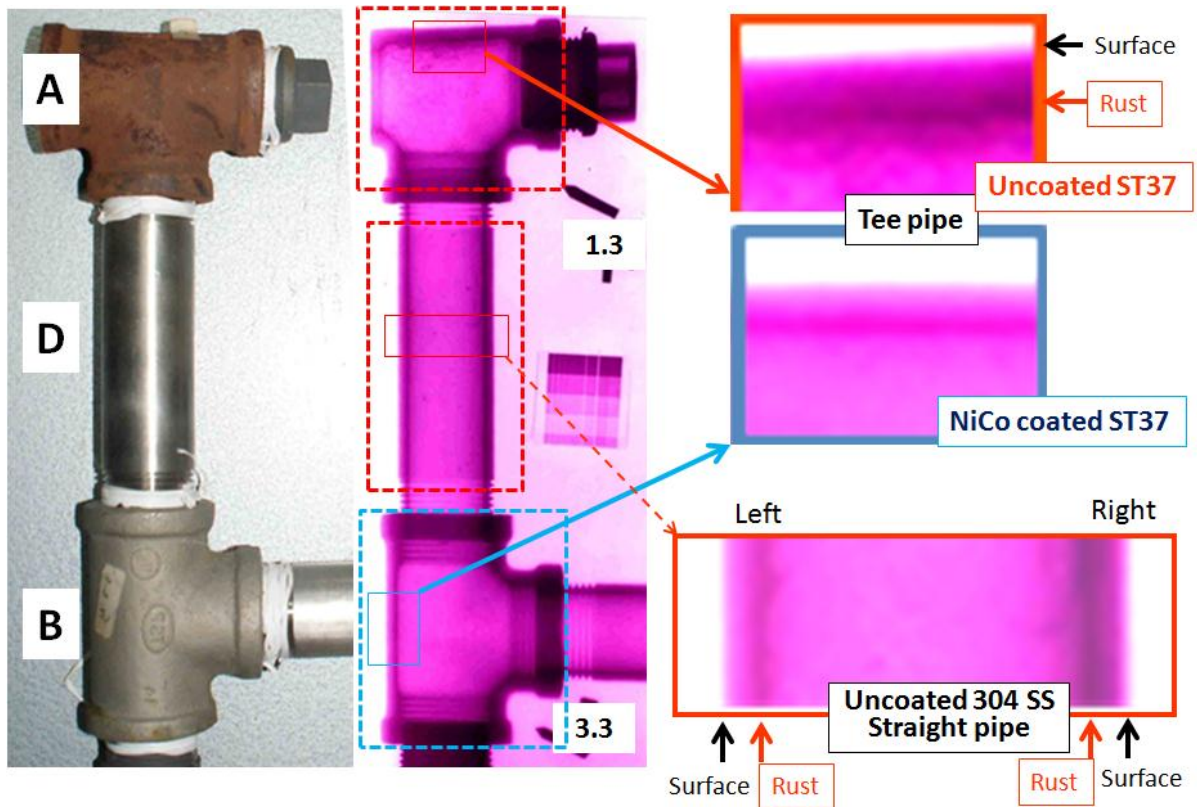


Figure 7.4. Photograph of pipe components at position 1 and corresponding neutron 2D radiography image. Magnified images obtained from the mid plane of all pipes area.

In the case of position 2, different thickness of rust could be observed on the wall surface of Tee pipe as shown in Fig 7.5. Pipe C with NiCo coated layer at this position was hardly form a protective scale and shown similar condition with pipe D (uncoated 304 SS). Chlorides can lead to breakdown of the passive layer accelerating the corrosion of unprotected surface ultimately leading to the formation of rust. For stright pipe, different corrosion mechanism could be occurred. Dark localized particle on the pipe wall was clearly seen in Fig

7.5. In order to understand the type of corrosion product, analysis of the pipe at position 2 will further characterized by 3D tomography as shown in Fig. 7.6.

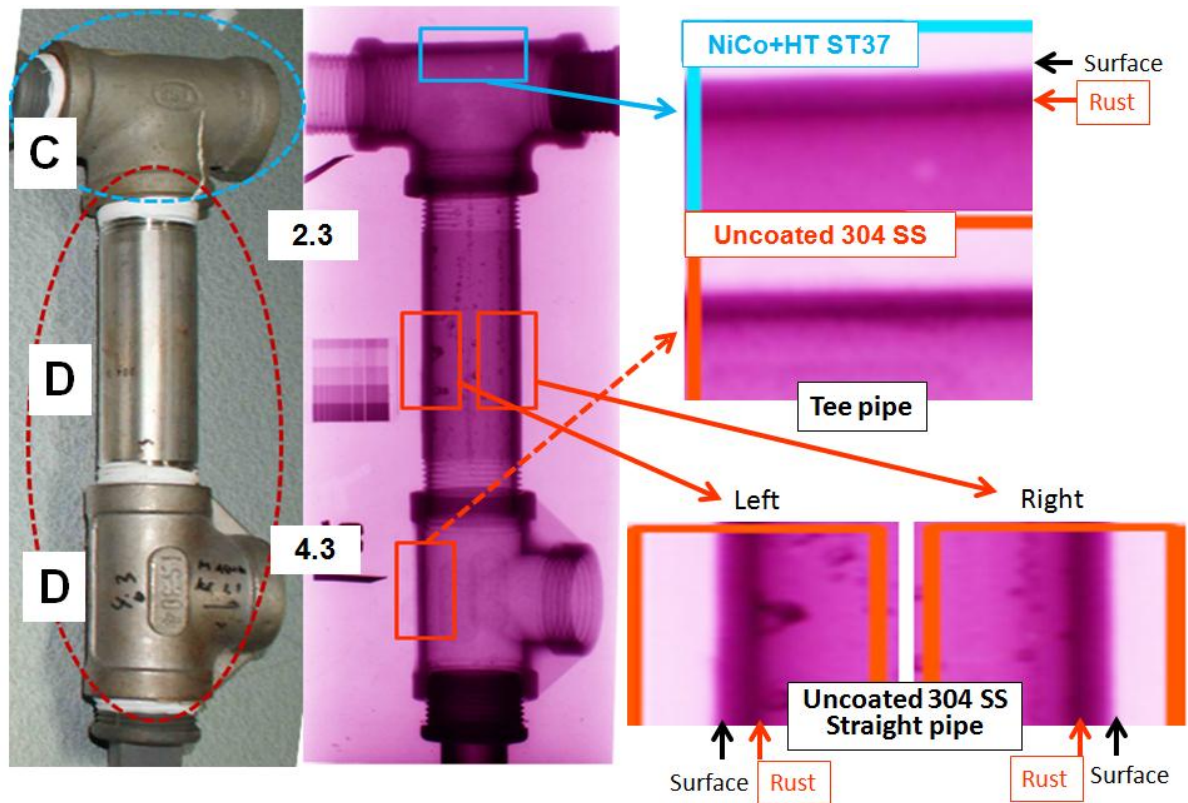


Figure 7.5. Photograph of pipe components at position 2 and corresponding neutron 2D radiography image. Magnified images obtained from the mid plane of all pipes area.

Characterization of tomogram slices provides more detail about the extension of the corroded area as shown in Fig 7.6. In fact, the inner surface of the straight shape of pipe D was found heavily corroded. This figure shows blister formation on the wall surface of stright pipe. The reason is due to the trapped gas accumulation and comes in contact with exposed pipe wall, then the blister locally developed. Another possibility for the formation of blister in this simulated corrosion test is due to when piping contains hydrogen, hydrogen attack can occur and it can take the form of hydrogen blistering. Blisters basically cause the pipe wall to delaminate. In the case of Tee shape, comparison could be made from pipe C and D (Fig.7.6).

For pipe D, it was found that the inner surface of the pipe was not uniformly or severely corroded. The higher contrast region around the edge is now more visible and represents the corrosion products or rust on the inside of pipe D. In contrast, pipe C with NiCo coated layer was good inside the surface wall. Thus, NiCo coated layer acts as protective layer for chloride when the ST37 or carbon steel pipe subjected to severe corrosion.

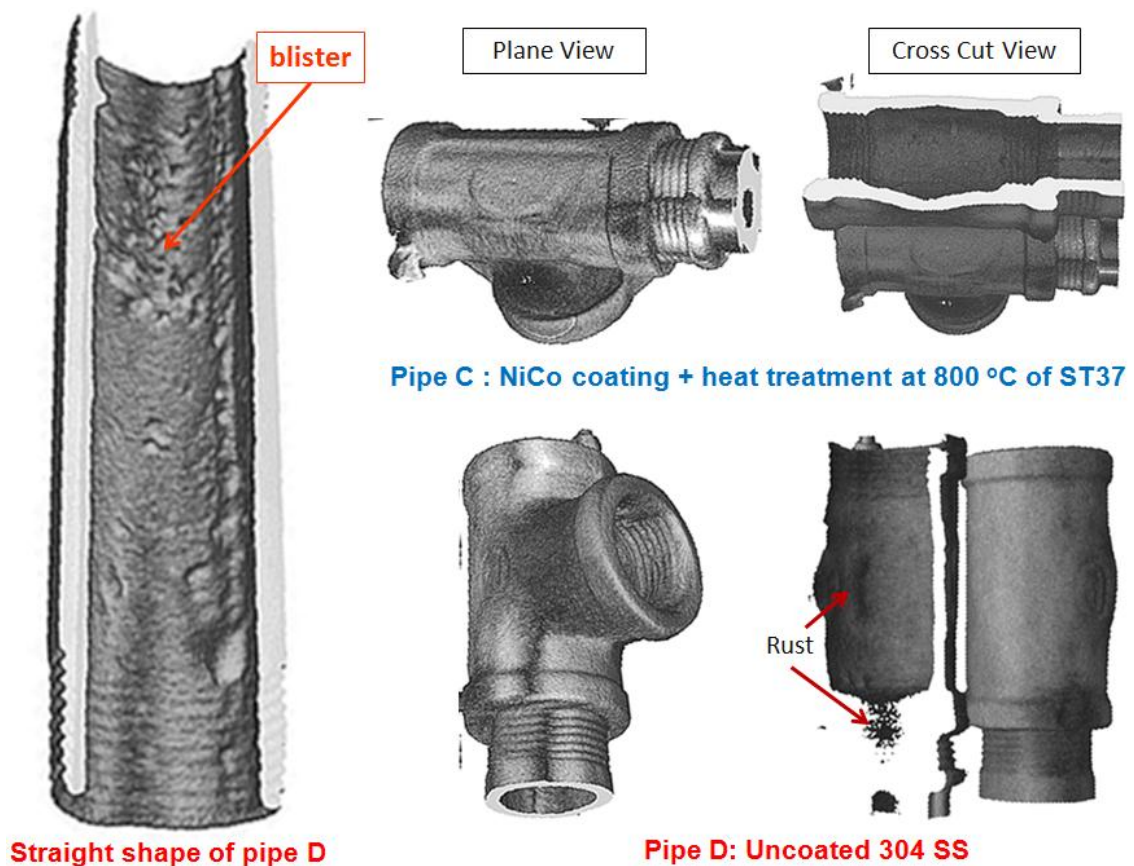


Figure 7.6. Neutron 3D tomography images of pipe components at position 2.

#### 7.4. Conclusions

This paper characterizes internal corrosion on coated piping system by non-destructive testing. The following conclusion can be drawn from this investigation:

1. The fundamentally different transmission properties of neutrons allow neutron

radiography and tomography to be an excellent qualitative diagnostic tool for internal corrosion behavior.

2. The results also conclusively showed the advantage of 3D neutron tomography for more complicated geometry elucidation by producing accurate three dimensional images of objects, from which virtual cuts through any required plane can be visualized.
3. By NRT method, rust and blister formation were clearly detected inside of the corroded pipe.
4. The high contrast of the surface corroded area is the result of the presence of hydrogen and oxygen, which has a high neutron attenuation coefficient, in the chemical composition of corrosion products.
5. The flow of acid vapor in the simulated piping system showed a very complicated behavior and it possibly depends on fluid dynamics of gas flow.
6. In this experimental condition, NiCo coated carbon steel showed much improvement to corrosion than 304 stainless steel.

## Chapter 8

### General Discussion and Conclusion

In this chapter, a modeling structure and corresponding phases formed on coated carbon steel are presented. The formation of intermetallic phases with high melting point and oxidation resistant is also clarified. Ni-based coated layer has ability to improved oxidation and corrosion resistance of carbon steel substrate when applied to the geothermal steam turbine and pipeline system. The performances of this coating system were summarized in this chapter to make some recommendation for further research and development in this field.

#### 8.1 Modelling structure and phase characterization

Fig. 8.1 shows a schematic illustration for three types of the coating systems which developed at different temperature of pack cementation process. The characterization results described in chapter 4 clearly revealed that the coated sample consist of three layers: the first (inner) layer of Ni(Co), the second (intermediate) layer of Ni(Al) and the third (outer) of Al(Cr,Ni). The coating temperature affects the coating thickness, and the phase constituents. Sample developed at 800 °C has a thickness in the range of 120 -160  $\mu\text{m}$ . The thickness of 900 and 1000 °C coated samples was about 2 and 3 times thicker than 800 °C coated samples, respectively. The complex structure containing void and crack was observed on sample developed at higher temperature. Based on the results in Fig 4.5, the reason is due to the fast outward diffusion of nickel to the Al rich layer and slow inward diffusion of Al to the inner layer thus the formed structure always containing cracks and voids. Another factor is due to the absence of intermetallic  $\text{Al}_3\text{Ni}$  phase from the inter-diffusion zone between Ni and Al. Therefore, the illustration in Fig. 8.1 describes the NiCoCrAl coating is not a simple two phase microstructure of  $\beta$  and  $\gamma$  phase, but it is considerably more complex with the presence of  $\text{Al}_3\text{Ni}$

and hexagonal  $\zeta$  phase. It might conclude that the phases constituents of the coated sample from substrate to the outer layer are describe as follow:

- 800 °C coated sample:  $\alpha(\text{Fe}) \rightarrow \gamma\text{-(Ni, Co)} \rightarrow \beta\text{-(Ni,Al)} \rightarrow \text{Al}_3\text{Ni} \rightarrow \zeta$ .
- 900 and 1000 °C coated sample:  $\gamma\text{-(Ni, Fe)} \rightarrow \alpha\text{-(Ni,Co)} \rightarrow \beta\text{-(Ni,Al)} \rightarrow \zeta$ .

From these results, it should be pointed out that 800 °C coated sample having more homogeneous layer than those samples developed at higher temperature. The stability of the phases formed on 800 °C coated samples is also important when subjecting this sample to the application in geothermal power plant.

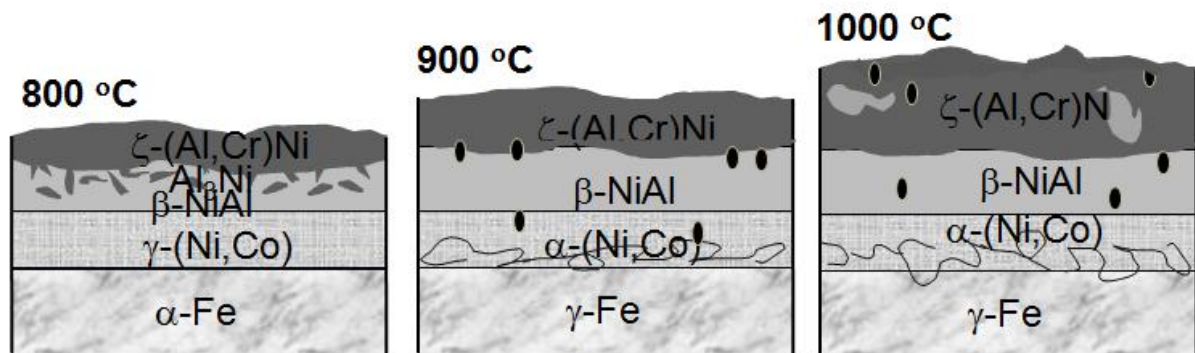


Figure 8.1. Schematic illustration showing the cross-sectional structure of the NiCoCrAl coated layer on carbon steel substrate with different coating temperature.

## 8.2 Performance of Ni-based coated carbon steel on oxidation and corrosion

The oxidation behavior of NiCoCrAl coatings deposited on carbon steel was evaluated at 800 °C for 100 hours in atmospheric air. The effect of different coating process on the oxidation of carbon steel was studied and comprehensively described in chapter 5. The oxidation mechanism was discussed based on the oxidation rate and formation of oxide scale on all of coated samples. It conclude that the oxidation kinetics was controled by the growth of alumina layer. Two stage of alumina growth had been presented which was transient stage for meta-stable alumina formation and steady stage for stable  $\alpha\text{-Al}_2\text{O}_3$ . In the case of 800 °C coated sample, the fast transformation from  $\delta\text{-}\theta$  to  $\alpha\text{-Al}_2\text{O}_3$  and slow growth of  $\alpha\text{-Al}_2\text{O}_3$  up to 100 h

exposure time confirmed that this sample has a good oxidation resistance. Details description on this part were presented in session 5.1. In line with the above description, the structure of as-coated sample developed at 800 °C also affected to the oxidation behavior. The performance of NiCoCrAl coatings depend greatly on the aluminum and chromium content. By referring to the results in session 5.3, it observed the high concentration of Cr on the top or aluminum layer. It is well known that Cr has the effect of increasing the Al activity and diffusivity and lowering the oxygen activity thus protective Al<sub>2</sub>O<sub>3</sub> scales formed with slow growth. In another words, α-Al<sub>2</sub>O<sub>3</sub> scale with continuous, thin and less porous structure was developed on the surface of 800 °C coated sample.

The performance of Ni-based layer after oxidation showed that this coatings system can be applied to the steam turbine. However, it should be noticed that this system is not suitable for geothermal pipeline. The reason is due to a high concentration of aluminum generally improve the oxidation and high concentration of Cr or Ni can improve corrosion resistance. Therefore, detailed study for developing NiCo coated layer on carbon steel is very important.

As described in chapter 7, simulated piping system was evaluated by acid vapor corrosion test using 37% HCl for 48 h. The performance of uncoated and coated carbon steel ST37 was compared with 304 SS pipes after acid vapor corrosion test. Neutron radiography and tomography (NRT) as a new method can accelerate simulation for materials testing. The results showed the existence of corrosion product in the form of rust and blister inside the uncoated carbon steel pipe wall. Chlorides can lead to breakdown of the passive layer accelerating the corrosion of unprotected surface ultimately leading to the formation of rust. Blister formed inside the uncoated 304 SS and it was verified by 3D tomography results. There was no dark contrast observed inside the NiCo coated pipe. It revealed that metallic or ceramic protective scale form and those elements were difficult to be penetrated by NRT.

### 8.3 The influence of the coating systems on the oxidation and corrosion

Fig. 8.2 shows the effectiveness of the NiCoCrAl coatings to the oxidation resistance compared with carbon steel without coating during isothermal condition at 800 °C for 100 h. The mass gain of carbon steel without coating increases linearly and very fast and the mass gain was about 460 mg/cm<sup>2</sup> after 100 h. On the contrary, it is well recognized that oxidation mass gain of NiCoCrAl coated sample was very slow. The mass gain increases gradually with the time and the oxidation kinetics follows parabolic rate law. The mass gain was about 0.82 mg/cm<sup>2</sup> after 100 h. It calculated to be about 575 times decreasing the mass gain compared with carbon steel without coating in this condition. The formation of protective alumina scale showed very crucial to protect the substrate after oxidation.

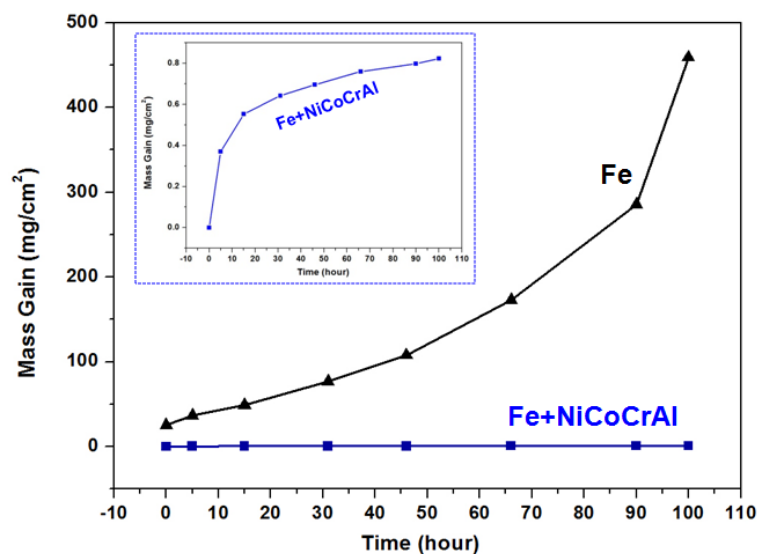


Figure 8.2. The oxidation mass gain performed at 800 °C for 100 h of carbon steel without and with NiCoCrAl coatings. Inset figure shows the magnified oxidation mass gain of NiCoCrAl coatings.

In the case of corrosion atmosphere, the behavior of different coating system was described in Fig. 8.3. Immersion test was carried out by using chloride acid in the concentration of 37% for 24 hours. By these results, it could be understood that NiCoCrAl was not suitable

in this condition. The best corrosion performance was obtained from NiCo and NiCoCr coated samples. However, the slowest mass change for NiCoCr pointed out that this system more suitable for longer exposure time. The formation of protective oxide like chromia might be one reason why this system more protective than NiO. Therefore, future work for protecting the pipeline from severe corrosion should be considered.

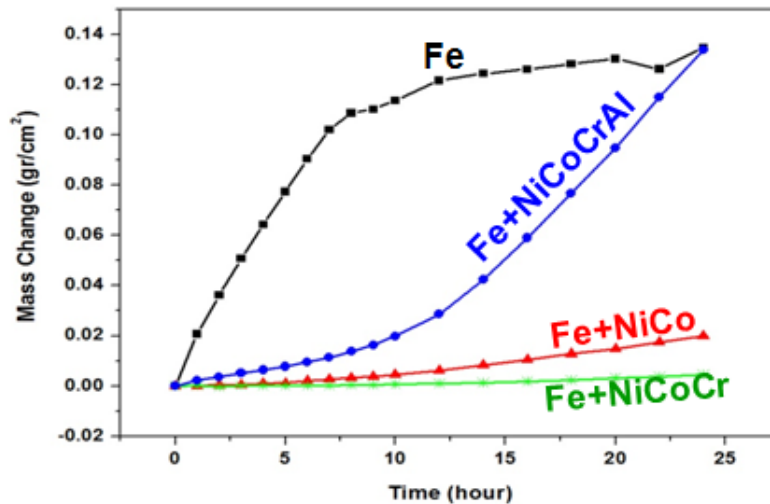


Figure 8.3. The corrosion mass change evaluated by immersion test using 37% HCl for 24 hours of several coating systems.

#### 8.4 Recommendations for future research and development

It would be interesting to do further investigation as describe follow:

- The influence of longer oxidation exposure time  
More detailed studies for 800 °C coated samples after oxidation for longer exposure time should be performed. That will provide a single and stable alumina phase and expect to be dense of oxide scale.
- The investigation of the effect of Cr in the coated sample on the corrosion resistance should be performed. The protective chromia can be formed and it is well known to have more protective than NiO oxide scale.
- The Cr pack cementation method used in the present study is difficult to apply for

complex shape of material. Other common method like thermal spray is also difficult to coat homogeneously inside the pipe.

- NiCo+Cr coated by plating are challenging work due to the limitation of the related references. Therefore by designing and selecting appropriate parameters used for electroplating will greatly affect to get optimum condition of the proposed coatings.

## References

- [1]. Energy information administration (EIA), Countries Report, March 5, 2014.
- [2]. Hitachi, Evaluation of Life Cycle CO<sub>2</sub> Emissions of Power Generation Technologies: Update for State-of-the-art Plants, 2010.
- [3]. R. Bertani, World geothermal power generation 2005–2010. Update report. Proceedings World Geothermal Congress 2010, Bali, Indonesia, (2010) 41.
- [4]. Fauzi, Suryadarma, S. Soemarinda, E. E. Siahaan, The Role of Pertamina in Geothermal Development in Indonesia, Proceedings World Geothermal Congress 2005, Antalya, Turkey, 24-29 April 2005.
- [5]. G.H. Koch, M.P.H. Brongers, N.G. Thompson, Y. P. Virmani, J.H. Payer, Corrosion costs and preventive strategies in the United States. Nace International, (2002).
- [6]. V. Viswanathan, R. Purgert, and P. Rawl, Coal-fired power materials, Advanced Materials and Processes, August 2008.
- [7]. D. Kevin. P.E. Rafferty, Piping, Geo-Heat Center, Klamath Falls, Oregon 97601.
- [8]. Casper, Pinchback, Geothermal Scaling and Corrosion, American Society for Testing and Materials, 1980.
- [9]. Y. Kurata, N. Sanada, H. Nanjo, J. Ikeuchi, Material damages in geothermal power plant, Proc.14<sup>th</sup> New Zealand Geothermal Workshop, (1992) 159 – 164.
- [10]. J.R. Nicholls, Designing oxidation resistant coatings, Journal of Metals, 52 (2000) 28-35.
- [11]. F.T. Talboom, R.C. Elam, and L.W. Wilson, Evaluation of advanced superalloy protection systems, ReprotCR7813, Houston, NASA, (1970).
- [12]. A. Feuerstein, J. Knapp, T. Taylor, A. Ashary, A. Bolcavage, and N. Hitchman, Technical and economical aspects of current thermal barrier coating systems for gas turbine engines by thermal spray and EBPVD: A review, Journal of Thermal Spray

- Technology, 17 (2008) 199-213.
- [13]. L.C. Driver, HVOF spraying of WC-Co & MCrAlY coatings for aero engine components, PhD thesis, Department of Mechanical, Materials and Manufacturing Engineering, University of Nottingham, Nottingham, (2004).
- [14]. A.G. Evans, D.R. Mumm, J.W. Hutchinson, G.H. Meier, and F.S. Pettit, Mechanisms controlling the durability of thermal barrier coatings, *Progress in Materials Science*, 46 (2001) 505-553.
- [15]. R. Prescott, and M.J. Graham, The formation of alumina oxide scales on high-temperature alloys, *Oxidation of Metals*, 38 (1992) 233-254.
- [16]. S. Bose, *High temperature coatings*, Elsevier, Amsterdam, (2007).
- [17]. M. Kutz, *Handbook of environmental degradation of materials*, William Andrew Inc., New York, (2005).
- [18]. Y. Tamarin, *Protective coatings for turbine blades*, ASM International, Ohio, (2002).
- [19]. J.M. Miguel, J.M. Guilemany, S. Vizcaino, Tribological study of NiCrBSi coating obtained by different process, *Tribol. Int.* 36 (2003) 181-187.
- [20]. A. Fossati, M. D. Ferdinando, A. Lavacchi, A. Scrivani, C. Giolli and U. Bardi, Improvement of the Oxidation Resistance of CoNiCrAlY Bond Coats Sprayed by High Velocity Oxygen-Fuel onto Nickel Superalloy Substrate, *Coatings 1* (2011) 3-16.
- [21]. T.Narita, T.Izumi, T.Nishimoto, Y.Shibata, K.Z.Thosin, S.Hayashi, *Advanced Coatings on High Temperature Applications*, *Materials Science Forum* Vol. 522-523 (2006) 1-14.
- [22]. Mordechai Schlesinger and Milan Paunovic, *Modern Electroplating*, Fourth Edition sponsored by the Electrochemical Society, Inc., New Jersey, John Wiley and Sons Publication (2000).
- [23]. William H. Safranek, *The properties of Electrodeposited Metals and Alloys*, A Handbook: Elsevier Publication (1974).

- [24]. J.W. Dini, H.R. Johnson, J.R. Helms, Sandia Livermore Laboratories Report No. SCL-DR-720090, (1972).
- [25]. Elvira Gomez, Salvador Pane, Elisa Valles, Electrodeposition of Co-Ni and Co-Ni-Cu systems in sulphate-citrate medium, *Electrochim. Acta* 51 (2005) 146-153.
- [26]. Liping Wang, Yan Gao, Qunji Xue, Huiwen Liu, Tao Xu, Microstructure and tribological properties of electrodeposited Ni-Co alloy deposits, *Appl. Surf. Sci.* 242 (2005) 326-332.
- [27]. R.J. Walter, Tensile properties of electrodeposited Nickel-Cobalt", *Plat. Surf. Finish.*, 73 (10) 48(1986).
- [28]. W.J.D. Jones, G.M.C. Lee, The Nickel Sulfamate Method, *Trans. Inst. Met. Finish.* 55 (1977) 70.
- [29]. Abner Brenner, *Electrodeposition of Alloys, Principles and Practice*, Vol. II, Academic Press.
- [30]. D. Golodnitsky, N.V. Gudin, G.A. Volyanuk, *Plating Surf. Finish.* 2 (1998) 65.
- [31]. V.A. Ravi, P.A. Choquet., R.A. Rapp, Chromizing-Aluminizing of Ni- and Fe-base Alloys by the Pack cementation Technique, *Oxidation of High-Temperature Intermetallics*, (1989) 127-145.
- [32]. S.C. Kung, R.A. Rapp, Analyses of the Gaseous Species in Halide-Activated Cementation Coating Packs, *Oxidation of metals*, 32 (1989) 89-109.
- [33]. B.K. Gupta, L.L. Seigle, The effect on the kinetics of pack aluminization of varying activator, *Thin solid films*, 73 (1980) 365-371.
- [34]. R.A. Rapp, Pack cementation diffusion coatings of steels for fossil fuel environments, *Proceedings of Corrosion 89*, April 17-21, New Orleans, Louisiana (1989) paper 532.
- [35]. W. Da Costa, B. Gleeson, D.J. Young, Codeposited Cr-aluminide coatings I. Definition of the Codeposition Regimes, *Journal of Electrochemical Society*, 141, 6, (1994) 1464-1471.

- [36]. O. Kubaschewski, P. Hobil, and B.E. Hopkins, Oxidation of metals and alloys, Butterworths Scientific London, (1953).
- [37]. M. Schütze, Protective oxide scales and their breakdown, Edited by D.R. Holmes, The institute of corrosion and Wiley series on corrosion and protection, J. Wiley & Sons, ISBN 0-471-95904 9 (1997).
- [38]. C.S. Tedmon, The effect of oxide volatilisation on the oxidation kinetics of Cr and Fe-Cr alloys, Journal of the Electrochemical society, 113, 8 (1966) 766-768.
- [39]. H. Asteman, J.E. Svensson, L.G. Johansson, Oxidation of 310 steel in H<sub>2</sub>O/O<sub>2</sub> mixtures at 600 °C: the effect of water-vapour-enhanced chromium evaporation, Corrosion Science, 44 (2002) 2635-2649.
- [40]. A.Yamauchi, K. Kurokawa., H. Takahashi, Evaporation of Cr<sub>2</sub>O<sub>3</sub> in atmospheres containing H<sub>2</sub>O, Oxidation of Metals, 59, 5/6 (2003) 517-527.
- [41]. M. Schütze, D. Rensch, M. Schorr, Parameters determining the breakaway oxidation behaviour of ferritic-martensitic 9 %Cr steels in H<sub>2</sub>O containing environments, Corrosion Engineering, Science and Technology, 39, 2 (2004) 157-166.
- [42]. M. Schütze, Mechanical interactions in oxide scales, Electrochemical Society Proceedings, 98-9 (1998) 1-17
- [43]. N. Briks, and G.H. Meier, Introduction to high temperature oxidation of metals, Edward Arnold Ltd, London, (1983).
- [44]. P. Kofstad, High temperature oxidation of metals, John Wiley & Sons, New York, (1966).
- [45]. C.S. Giggins, and F.S. Pettit, Oxidation of Ni-Cr-Al alloys between 1000 degrees and 1200 degrees C, Journal of the Electrochemical Society, 118 (1971).
- [46]. P. Didik, S. Eni, D. Fredina, and K. A. Zaini, The influence of Cr and Al pack cementation on low carbon steel to improve oxidation resistance, AIP Conf. Proc. 1454, (2012) 234-237.

- [47]. N. Miyajima, C. Holzapfel, J. Microscopy 238 (2010) 200-209.
- [48]. S. Tateno, R. Sinmyo, K. Hirose and H. Nishioka, Rev. of Sci. Inst. 80 (2009) 1-4.
- [49]. M. Hashimoto, Advances in Nano-Level Materials Characterization Technology, Nippon Steel Technical Report No. 91 January 2005.
- [50]. P. Roger, Neutron Scattering: A primer, Los Alamos Science, (1990).
- [51]. J.I. Goldstein, Scanning Electron Microscopy and X-ray Microanalysis, New York, Springer 3<sup>rd</sup> ed., (2003).
- [52]. S. Eni, Y. Wang, N. Hashimoto, S. Ohnuki and T. Narita, Material Transaction 52 (2011) 319-323.
- [53]. D.B. Williams, C. B. Carter, Transmission Electron Microscopy: a Textbook for Materials Science New York, Springer, (1996).
- [54]. E.E. Levi, Practical hardness testing made simple, (available on <http://www.aws.org/educators/Library/0000/000587.pdf>).
- [55]. D.B. Williams, C. B. Carter, Transmission electron microscopy: a textbook for materials science, New York, Springer, (1996).
- [56]. N. Miyajima, C. Holzapfel, Y. Asahara, L. Dubrovinsky, D.J. Frost, D.C. Rubie, M. Dressler, K. Niwa, M. Ichihara and T. Yagi, Combining FIB milling and conventional Argon ion milling techniques to prepare high-quality site-specific TEM samples for quantitative EELS analysis of oxygen in molten iron J. Microscopy 238 (2010) 200-209.
- [57]. S. Eni, Y. Wang and S. Ohnuki, The powerful combination of ion-milling method for XTEM preparation: Application to a diffusion barrier coating on Nb substrate, AIP Conf. Proc. 1454, (2012) 242-245.
- [58]. L.A. Giannuzzi, F.A. Stevie, Introduction to focused ion beams: instrumentation, theory, techniques, and practice, Springer (2005).
- [59]. Emphyrean, The multi - purpose solution for your analytical needs, The analytical X-ray

Company, (2012).

- [60]. JEOL Company, High performance general purpose SEM, (available on <http://www.jeol.co.jp/>).
- [61]. N. Mori, Micro area analysis with JXA-8530F (FE-EPMA), JEOL News Vol.45 No. 1 (2010) 42-46.
- [62]. A. Bromley, Neutron in science and technology, Physics Today, (1983) 31-39.
- [63]. By Baldev Raj, T. Jayakumar, M. Thavasimuthu, Practical non-destructive testing, 2<sup>nd</sup> edition, Woodhead Publishing limited, England (2002).
- [64]. J.C Domanus, Practical neutron radiography, Kluwer Academic Publ. The Netherlands, (1992).
- [65]. A.A. Harms and D.R. Wyman, Mathematics and Physics of Neutron Radiography, D. Riedel Publ. Company, the Netherland, (1986).
- [66]. Sutiarmo, Bharoto, Setiawan, Juliyani and Fahrurrozi, Development of CCD Camera for Neutron Radiography Facility, RN1 in BATAN Serpong, Proceedings of National Conference on Human Resources of Nuclear Technology (2010) 439.
- [67]. Bharoto, Development of Data Acquisition and Control Software for Neutron Radiography Facility at Serpong, Indonesia, Atom Indonesia Vol. 39 No. 2 (2013) 95 - 99.
- [68]. D. Golodnitsky, Yu. Rosenberg, A. Ulus, The role of anion additives in electrodeposition of nickel/cobalt alloys from sulfamate electrolyte, Electrochimica Acta 47 (2002) 2707/2714.
- [69]. Meenu Srivastava, V. Ezhil Selvi, V.K. William Grips, K.S. Rajam, Surface and Coatings Technology 201 (2006) 3051-3060.
- [70]. T. Watanabe, Nano Plating - Microstructure Formation Theory of Plated, Elsevier, 2004.
- [71]. Y. Mishima, S. Ochiai and T. Suzuki, Acta Mater. 33 (1985) 1161-1169.

- [72]. C. Georgeta and A. Angel, *Metalurgia International*, Vol. 11, No. 8 (2006) 36-45.
- [73]. R.D Noebe, R.R Bowman, M.V Nathal, *Int. Mater Rev.* 38 (1993) 193-232.
- [74]. D.Shi, B.Wen, R. Melnik, S. Yao, T. Li, *J. Solid State Chemistry* 182 (2009) 2664–2669.
- [75]. B. Grushko, W. Kowalski, D. Pavlyuchkov, B. Przepiorzyn´ski, M. Surowiec, *J. Alloys Compd.* 460 (2008) 299-304.
- [76]. E.D. Specht, P.D. Rack, A. Rar, G.M. Pharr, E.P. George, J.D. Fowlkes, H. Hong, E. Karapetrova, *Thin Solid Films* 493 (2005) 307 – 312.
- [77]. B. Grushko, W. Kowalski, D. Pavlyuchkov, S. Mi, M. Surowiec, *J. Alloys and Compounds* 485 (2009) 132–138.
- [78]. V. Raghavan, *J. Phase Equilibria and Diffusion* Vol.30 No. 1 (2009) 61-63.
- [79]. X.M. Hou, K.C. Chou, Quantitative interpretation of the parabolic and non-parabolic oxidation behavior of nitride ceramic, *Journal of the European Ceramic Society*, 29 (2009) 517-523.
- [80]. B. Wang, C. Sun, J. Gong, R. Huang, L. Wen, Oxidation behaviour of the alloy IC-6 and protective coatings, *Corrosion Science*, 46 (2004) 519-528.
- [81]. Y. Kitajima, S. Hayashi, T. Nishimoto, T. Narita, S. Ukai, Rapid formation of  $\alpha$ -Al<sub>2</sub>O<sub>3</sub> scale on an Fe–Al alloy by pure-metal coatings at 900 °C, *Oxidation of Metal*, 73 (2010) 375–388.
- [82]. K. Hauffe, G.H. Meier, *Oxidation of Metals*, Plenum, New York (1966).
- [83]. G.M. Liu, M.S. Li, J. H. Ma, Y.C. Zhou, *Trans. Nonferrous Met. Soc. China*, 17 (2007) 595-599.
- [84]. I. Levin and D. Brandon, *J. Am. Ceram. Soc.* 81 (1998) 1995-2012.
- [85]. P. S. Santos, H. Souza Santos and S.P Toledo, *Material Research*, 3 (2000) 104-114.
- [86]. J. R. Nicholls, P. Hancock and L. H. Al Yasiri, *Materials Science and Technology*, 5 (1989) 799.

- [87]. M. Seraffon, N. J. Simms, J. Sumner, J. R. Nicholls, The development of new bond coat compositions for thermal barrier coating systems operating under industrial gas turbine conditions, *Surface and Coating Technology*, 206 (2011) 1529-1537.
- [88]. J.D. Kuenzly and D.L. Douglass, *Oxidation of Metals*, 8 (1974) 139-178.
- [89]. M. Seraffon, N. J. Simms, J. Sumner, J. R. Nicholls, Oxidation behavior of NiCrAl and NiCoCrAl bond coatings under industrial gas turbine conditions, *Oxidation of Metals*, 81 (2014) 203–215.
- [90]. S. Taniguchi and A. Andoh, *Oxidation of Metals*, 58 (2002) 545-562.
- [91]. P.Y. Hou, *Annu. Rev. Mater. Res.*, 38 (2008) 275-298.
- [92]. G.C. Rybicki and J.L. Smialek, *Oxidation of Metals*, 31 (1989) 275-304.
- [93]. R.W.G. Wyckoff, *Crystal Structures*, 2nd ed., vol. 2 (Interscience, New York, 1964), pp. 6-8.
- [94]. P. N. Kalu, D. Waryoba, A.D. Rollett: *EML* 5930 (2005), 27-750.
- [95]. J.C Yang, E. Schumann, I. Levin and M. Ruhle, *Acta Mater*, 46 (1998) 2195-2201
- [96]. K. Reszka, J. Morgiel, Z. Zurek, A. Jaron, *Archives of Metallurgy and Materials*, 59 (2014) 77-81.
- [97]. V. Jayaram and C.G. Levi, *Acta Metall*, 37 (1989) 569-578.
- [98]. H.S.C O`neill, W.A. Dollase, and C.R. Ross, *Phys, Chem Minerals*, 18 (1991) 302-319.
- [99]. B. Alling, A. Khatibi, S. Simak, P. Eklund and L. Hultman, *Journal of Vacuum Science and Technology. A. Vacuum, Surfaces, and Films*, 31 (2013) 3-17.
- [100].A.H Truesdell, J.R. Haizlip, H. Armannsson, F. D'Amore, Origin and transport of chloride in superheated geothermal steam. *Geothermics*, 18 (1989) 295-304.
- [101].D.E. White, G.A. Waring, *Volcanic Emanations, Data of Geochemistry*, USGS Prof Paper 440-K (1963) 29.
- [102].J.V. Lawless, R.C Gonzales, *Geothermal geology and review of exploration*, Biliran

- Island. Proceedings of 4th New Zealand Geothermal Workshop (1982) 161-167.
- [103].R.O. Fournier, J.M. Thompson, Composition of steam in the system NaCl-KCl-H<sub>2</sub>O-quartz, *Geochim cosmochim Acta* 57 (1993) 4365-4375.
- [104].J.L. Bischoff, J.R. Rosenbauer, R.O. Fournier, The generation of HCl in the system CaCl<sub>2</sub>-H<sub>2</sub>O: Vapor-liquid relations from 380-500 °C, *Geochimica et Cosmochimica Acta* 60 (1996) 7-16.
- [105].D. Kevin. P.E. Rafferty, Piping, Geo-Heat Center, Klamath Falls, Oregon 97601.
- [106].Shreir LL. Corrosion, metal / environment reactions, 2nd ed., London: Newnes-Butterworths, (1979).
- [107].J. Cai, C. Li, X. Tang, F. Ayello, S. Richter, S. Netic, *Chemical Engineering Science*, 73 (2012) 334–44.
- [108].Y. Xiao, S. Netic, A stochastic prediction model of localized CO<sub>2</sub> corrosion, *Corrosion* 2005, NACE paper no. 05057, Houston, (2005).
- [109].B. Brown, K.L. Lee, S. Netic, Corrosion in multiphase flow containing small amounts of H<sub>2</sub>S, *Corrosion* 2003, NACE paper no. 03341, Houston, (2003).
- [110].By Baldev Raj, T. Jayakumar, M. Thavasimuthu, *Practical non-destructive testing*, 2<sup>nd</sup> edition, Woodhead Publishing limited, England (2002).
- [111].P. Roger, *Neutron Scattering: A primer*, Los Alamos Science, (1990).

## Academic Achievement

### 1. Publications

- [1]. **S. Eni**, K. Zaini, Y. Wang, N. Hashimoto, S. Hayashi, and S. Ohnuki, Nano-Micro Characterization of NiCoCrAl Coating on Carbon Steel Substrate, *Advanced Materials Research* Vol. 896 (2014) pp 586-590.
- [2]. **Eni Sugiarti**, Fredina Destyorini, Kemas A. Zaini, Yongming Wang, Naoyuki Hashimoto, Somei Ohnuki and Shigenari Hayashi, Characterization of Ni-based Coatings on Carbon Steel by Electron Microscopy, *Surface and Coatings Technology* (Accepted).
- [3]. **Eni Sugiarti**, Kemas A. Zaini, Yongming Wang, Naoyuki Hashimoto, Somei Ohnuki and Shigenari Hayashi, Transmission Electron Microscopy of Meta-Stable Al<sub>2</sub>O<sub>3</sub> Scale Formed on NiCoCrAl Coated Layer during Isothermal Oxidation, *Oxidation of Metal* (Accepted).
- [4]. **Eni Sugiarti**, Kemas A. Zaini, Yongming Wang, Naoyuki Hashimoto, Somei Ohnuki and Shigenari Hayashi, Effect of Pack Cementation Temperature on Oxidation Behavior of NiCoCrAl Coated Layer, *Advanced Materials Research* (Accepted).
- [5]. **Eni Sugiarti**, Kemas A. Zaini, D.D. Resetiana, Sutiarmo, Fahrurrozi, Yongming Wang, Naoyuki Hashimoto, Somei Ohnuki, and Shigenari Hayashi, Analysis of Internal Corrosion on Coated Piping System by Non-Destructive Testing (Under Review).

### 2. Patent

- [1] Multilayer coatings for metal substrate, Register No. P00201407030.

### 3. Others

- [1]. **Eni Sugiarti**, Youngmin Wang, Naoyuki Hashimoto, Somei Ohnuki and Toshio Narita, Phase Characterization of Re-Based Diffusion Barrier Layer on Nb Substrate, Material Transaction, Vol. 52 No.3 (2011) 319-323.
- [2]. **S. Eni**, Y. Wang, N. Hashimoto, S. Ohnuki and T. Narita, Cross-sectional TEM Characterization of Re-Based Diffusion Barrier on Nb Substrate, Materials Science Forum Vol. 696 (2011) 318-323.
- [3]. **Eni Sugiarti**, Youming Wang and Somei Ohnuki: The Powerful Combination of Ion-Milling Method for XTEM Preparation, American Institute of Physics (AIP) Conf. Proc., 1454, (2012) 242-245.

### 4. Awards

- [1]. High Resolution Electron Microscopy Observation of Intermetallic Compound in the Coated Layer on Nb Substrate. Presenter award from The Japan Institute of Metal (JIM), January 27, 2011, Muroran, Japan.
- [2]. Development of Diffusion Barrier Layer for High Temperature Materials, Fellowship award for Women in Science from Loreal – UNESCO, December 10, 2012. Jakarta, Indonesia.

### 5. Presentations

- [1] **Eni Sugiarti** and Sutiarto, Analysis of Internal Corrosion on Piping Carbon Steel by Neutron Radiography, Conference on 8th Neutron and X-ray Scattering: Application, Simulation and Modelling for Supporting Material Research in Indonesia, PTBIN-BATAN, Tangerang, Indonesia October 4, 2011.
- [2] **Eni Sugiarti**, Youming Wang and Somei Ohnuki, The Powerful Combination of Ion-Milling Method for XTEM Preparation, International Conference on Physics and Its

- Applications (ICPAP 2011), Institute Technology of Bandung (ITB), Indonesia, November 10-11, 2011.
- [3] **S. Eni**, Y. Wang, K.A. Zaini, S. Hayashi, N. Hashimoto, S. Ohnuki, Characterization of Coated Carbon Steel by means of Electron Microscopy and Neutron Radiography, The 150th Annual Spring Meeting of The Japan Institute of Metals, Yokohama, Japan, March 28-30, 2012.
- [4] **Eni Sugiarti**, Fredina Destyorini and Kemas A. Zaini Thosin, Effect of Temperature Process on the Oxidation of Coated Carbon Steel, The 2nd International Conference on Theoretical and Applied Physics (ICTAP 2012), University of Palangkaraya, Indonesia, October 19-20, 2012.
- [5] **S. Eni**, K. Zaini, Y. Wang, N. Hashimoto, S. Hayashi, and S. Ohnuki, Nano-Micro Characterization of NiCoCrAl Coating on Carbon Steel Substrate , The 2013 International Conference on Advanced Materials Science and Technology (ICAMST 2013), Univeristy of Gajah Mada, Yogyakarta, Indonesia, September 17-18, 2013.
- [6] **Eni Sugiarti**, Kemas A. Zaini, Yongming Wang, Naoyuki Hashimoto, Shigenari Hayashi and Somei Ohnuki, Nano-Micro Structural Investigation of the Oxide Scale on Carbon Steel Substrate, International Symposium of High-temperature Oxidation and Corrosion 2014 (ISHOC), Hakkodate, Japan, June 23-27, 2014.
- [7] **Eni Sugiarti**, Kemas A. Zaini, Yongming Wang, Naoyuki Hashimoto, Somei Ohnuki, and Shigenari Hayashi, Effect of Pack Cementation Temperature on Oxidation Behavior of NiCoCrAl Coated Layer, The 1st Materials Research Society of Indonesia (MRS-Id) Meeting, Bali, Indonesia, September 26-28, 2014.
- [8] **Eni Sugiarti**, Kemas A. Zaini, Yongming Wang, Naoyuki Hashimoto, Somei Ohnuki, and Shigenari Hayashi, Effects of Oxidation Temperature on the Oxide Scale Formation of NiCoCrAl Coatings on Low Carbon Steel, The 2nd International Conference on Functional Materials Science (ICFMS 2014), Lombok, Indonesia, November 12-13, 2014.

## 6. Workshop

- [1] Workshop on Exploring the soft Matters at Nanometer Scale by Small Angle Scattering (Neutron and X-Ray), Organized by Indonesian Polymer Society, Serpong, Indonesia, October 9-11, 2012.
- [2] Workshop on Analysis of Morphology Material by Atomic Force Microscope (AFM), Organized by Indonesian Institute of Sciences (LIPI), Tangerang, Indonesia, November 20-21, 2012.
- [3] Workshop on Strengthening R&D Management Capacity of Researchers and Research Managers of R&D Institutes in the Area of Nanotechnology, Organized by Indonesian Institute of Sciences (LIPI) cooperation with APCTT - ESCAP, Jakarta, Indonesia, June, 26-27 2013.
- [4] Workshop on Interpretation of X-ray Data Analysis, Organized by Indonesian Institute of Sciences (LIPI), Serpong, Indonesia, November 21-22, 2013.
- [5] The 6th AONSA Neutron School 2014, Organized by National Nuclear Energy Agency (BATAN) of Indonesia, October 12 – 17, 2014.